Theoretical Studies on the Influence of Size and Support Interactions of Copper Catalysts for CO_2 Hydrogenation to Methanol

Zur Erlangung des akademischen Grades eines

DOKTORS DER NATURWISSENSCHAFTEN

(Dr. rer. nat.)

von der KIT-Fakultät für Chemie und Biowissenschaften

des Karlsruher Instituts für Technologie (KIT)

genehmigte

DISSERTATION

von

M.Sc. Amir Hossein Hakimioun

Abstract

Global warming and climate change, caused by greenhouse gases (GHG) released into the atmosphere by human activities, are becoming one of the world's most crucial issues. Carbon dioxide (CO_2) is the primary emitted greenhouse gas, produced mostly from the usage of fossil fuels. The daily increase in the global energy demand and the promising potential of converting and using the captured emitted CO_2 to value-added products and chemicals (e.g., methanol) resulted in a vast amount of inventions and investigations on this topic. Methanol is the simplest alcohol and one of the valuable converted products of the CO_2 conversion process, which can be used as renewable energy, fuels, etc. In industry, methanol is synthesized through heterogeneous catalytic reactions utilizing Cu-based catalysts, promoted or unpromoted nanoparticles (NPs) on support materials. Theoretical and computational methods of modelling heterogeneous catalytic reactions, done mostly by applying density functional theory (DFT) methods, are one example of benefiting from computer-aided material designing. However, investigating this procedure is challenging as the difference in the size scale of the study systems between the experiments and theoretical works are different. DFT is perfectly capable of handling systems consisting of a few hundred atoms, which contrasts with real systems with thousands of atoms.

In this thesis, by applying cost-efficient and, at the same time, highly accurate computational models, some critical challenges regarding the procedure of converting CO_2 to methanol, such as the catalyst's particle size and shape effect, support effect, and applications of trends in catalytic reactions, were investigated. The utilization of DFT provided a fundamental understanding of the properties of the transition metal (TM) catalysts, with sizes ranging from 0.5 nm to 3.6 nm, using their fixed geometries and the adsorption energies of the intermediates related to methanol synthesis as descriptors. In addition, after confirming the reliability of the proposed models for different transition metals, the influence of the supports, inert (graphene) and oxide (magnesium oxide (MgO)), on the properties of NPs, through adsorption studies with different sizes and shapes was determined.

Moreover, the development of the models mentioned paved the way toward finding the trends in catalytic reactions through linear scaling relationships between the adsorption energies of the intermediates involved in methanol synthesis. In addition to the linear scaling relationships in the adsorption energies, the important role of geometrical and electronic effects affecting these relations is also demonstrated.

Finally, the origin of the copper particle size effect, which plays a significant role in CO_2 hydrogenation to methanol and its competitor reverse water gas shift reaction (RWGS), is demonstrated as the reaction being clearly structure sensitive and providing a new guideline in designing of novel catalysts for methanol synthesis from CO_2.

Zusammenfassung

Die globale Erwärmung und der Klimawandel, die durch die vom Menschen in die Atmosphäre freigesetzten Treibhausgase (THG) verursacht werden, sind zu einem der wichtigsten Themen der Welt geworden. Kohlendioxid (CO_2) ist das wichtigste emittierte Treibhausgas, das hauptsächlich durch die Nutzung fossiler Brennstoffe entsteht. Der täglich steigende weltweite Energiebedarf und das vielversprechende Potenzial der Umwandlung und Nutzung des abgeschiedenen CO_2 in Produkte und Chemikalien mit hohem Mehrwert (z. B. Methanol) haben zu einer Vielzahl von Erfindungen und Untersuchungen zu diesem Thema geführt. Methanol ist der einfachste Alkohol und eines der wertvollsten umgewandelten Produkte des CO_2-Umwandlungsprozesses, das als erneuerbare Energie, Treibstoff usw. verwendet werden kann. In der Industrie wird Methanol durch heterogene katalytische Reaktionen unter Verwendung von Katalysatoren auf Cu-Basis, geförderten oder ungeförderten Nanopartikeln (NPs) auf Trägermaterialien synthetisiert. Theoretische und computergestützte Methoden zur Modellierung heterogener katalytischer Reaktionen, die meist mit Hilfe der Dichtefunktionaltheorie (DFT) durchgeführt werden, sind ein Beispiel dafür, wie man vom computergestützten Materialdesign profitieren kann. Die Untersuchung dieses Verfahrens stellt jedoch eine Herausforderung dar, da sich die Größenordnung der untersuchten Systeme zwischen den Experimenten und den theoretischen Arbeiten unterscheidet. Die DFT ist durchaus in der Lage, Systeme mit einigen hundert Atomen zu handhaben, was im Gegensatz zu realen Systemen mit Tausenden von Atomen steht.

In dieser Arbeit wurden durch die Anwendung kosteneffizienter und gleichzeitig hochpräziser Berechnungsmodelle einige kritische Herausforderungen im Zusammenhang mit der Umwandlung von CO_2 in Methanol untersucht, wie z. B. der Effekt der Partikelgröße und -form des Katalysators, der Effekt des Trägers und die Anwendung von Trends in katalytischen Reaktionen. Der Einsatz von DFT ermöglichte ein grundlegendes Verständnis der Eigenschaften der Übergangsmetall (TM)-Katalysatoren mit einer Größe von 0,5 nm bis 3,6 nm, wobei ihre festen Geometrien und die Adsorptionsenergien der Zwischenprodukte der Methanolsynthese als Deskriptoren verwendet wurden. Nachdem die Zuverlässigkeit der vorgeschlagenen Modelle für verschiedene Übergangsmetalle bestätigt wurde, wurde außerdem der Einfluss der Träger, inert (Graphen) und Oxid (Magnesiumoxid (MgO)), auf die Eigenschaften der NPs durch Adsorptionsstudien mit verschiedenen Größen und Formen bestimmt.

Darüber hinaus ebnete die Entwicklung der genannten Modelle den Weg zur Ermittlung der Trends in den katalytischen Reaktionen durch lineare Skalierungsbeziehungen zwischen den Adsorptionsenergien der an der Methanolsynthese beteiligten Zwischenprodukte. Neben den linearen Skalierungsbeziehungen bei den Adsorptionsenergien wird auch die wichtige Rolle von geometrischen und elektronischen Effekten aufgezeigt, die diese Beziehungen beeinflussen.

Schließlich wird der Ursprung des Kupferpartikelgrößeneffekts, der bei der CO_2-Hydrierung zu Methanol und der damit konkurrierenden umgekehrten Wassergasverschiebungsreaktion (RWGS) eine wichtige Rolle spielt, aufgezeigt, da die Reaktion eindeutig strukturabhängig ist und einen neuen Leitfaden für die Entwicklung neuartiger Katalysatoren für die Methanolsynthese aus CO_2 darstellt.

Table of contents

1 Introduction

1.1 Challenges of CO₂ Emission

Global warming, climate change, greenhouse gases, CO_2 emission, carbon neutrality, fossil fuels, etc., include all the terms that have been frequently heard in recent years and decades. Growing consumption of fossil fuels resulted in increased CO_2 concentration in the atmosphere, which has made it a worldwide concern. Realizing this issue united politicians, scientists, businesses, and social media to pursue possible solutions for it in an engagement movement. For instance, as a consequence of the motivative talks and activities of Al Gore and the Intergovernmental Panel on Climate Change (IPCC), who won the Nobel Peace prize in 2007, the increase of public engagement with the adoption of the Paris Agreement[1] and the protesting movements of young generations, were observed.

Global warming is caused by heat-trapping greenhouse gases (GHG), such as carbon dioxide (CO_2), methane (CH_4), and nitrous oxide (N_2O), which are produced by daily human activities. As shown in **Figure 1.1**, the level of CO_2 concentration in the atmosphere, based on recent studies, reached the highest level of 418.90 ppm in July 2022, which is more than doubled in eight glacial periods (800,000 years).
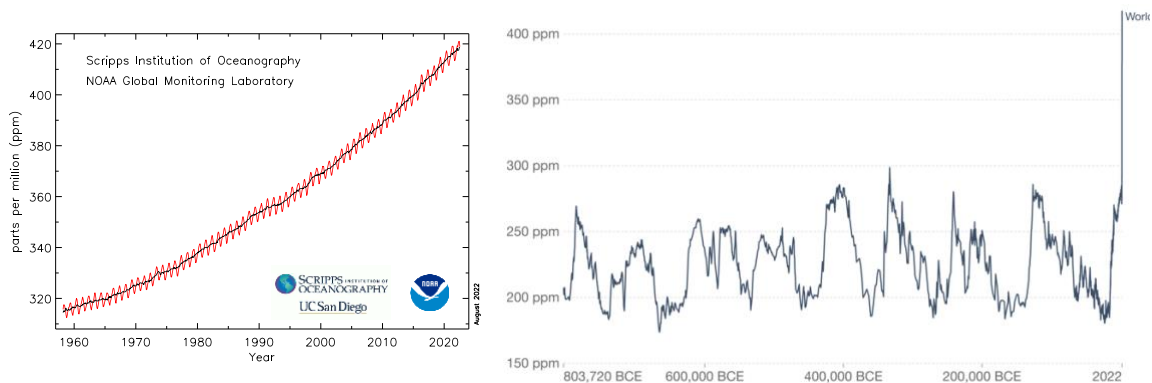
Figure 1.1. Left: Mean carbon dioxide measured at Mauna Loa Observatory, Hawaii. The red line illustrates the monthly mean values and the black line illustrate the correction for the average seasonal cycle. The credit of the image is for NOAA ESRL Global Monitoring Division, Boulder, Colorado, USA (http://esrl.noaa.gov/gmd/).[2] Right: The long-term global atmospheric concentrations of CO_2 (in ppm) in the past 800,000 years. The plot is on the basis of comparing the atmospheric samples contained in ice cores with recent direct measurements.[3] The graph is provide by National Oceanic and Atmospheric Administration (NOAA) (https://gml.noaa.gov/ccgg/trends/global.html)

Figure 1.1 depicts the amount of CO_2 present in the atmosphere in the past few decades and the past 800,000 years until 2022.[2-4] As can be seen, the CO2 level fluctuated between the ice ages and warmer interglacial periods (200 ppm to 280 ppm) till 1950, when it reached 300 ppm, and

today it is reaching the record of 420 ppm. It indicates the influence of the Industrial Revolution and the increase of burning fossil fuels on the level of atmospheric CO_2.[5]

Contrary to what the public might assume, climate change and CO_2 emission are not recent concerns and known threats to the human future. In the early work of Joseph Fourier (French mathematician and physicist), in 1824, the possible influence of atmospheric gases on increasing the earth's temperature was shown.[6] His postulate was further investigated and followed by other scientists worldwide until 1856, when the studies of an American scientist Eunice Foote began innovative topics on the potential impacts of CO_2 on global climate warming. Since her studies were presented only at the AAAS annual meeting[7] in Albany, New York, in 1856 and not published as formal publications, the credit for recognizing these concepts is given to John Tyndall. He published a series of papers regarding this topic. He indicated that, compared to oxygen and nitrogen, which constitute the bulk of the atmosphere, CO_2, water vapor, and hydrocarbon gases, such as methane, were highly efficient in absorbing radiant energy. He further postulated the possible impact on climate as the result of changes in the concentrations of those gases.[8-9] All of the mentioned studies were confirmed and authenticated by the Swedish physical chemist Svante Arrhenius in 1896, who explored the greenhouse effect on climate change and identified CO_2 as the key to the increase of the earth's temperature.[10] Scientific studies were carried out on this topic. Until the threatening effect of using fossil fuels and releasing CO_2 into the atmosphere was addressed and warned to the public in a short paragraph-long report in the Rodney & Otamatea Times newspaper in 1912 (110 years ago) with the headline "Coal Consumption Affecting Climate". In that report, a yearly burning of 2 billion tons of coal in the world, which resulted in releasing of 7 billion tons of CO_2 into the atmosphere, was mentioned. In addition, a blanket-like effect of the air on the earth, which results in the earth's temperature rise and its considerable impact on the future, was anticipated.[11]

Since the early scientific studies on issues related to climate change and global warming and considering the urgent attention to the daily rise of the concentration of greenhouse gases, especially CO_2, the number of scientific published papers on this topic have arisen remarkably. **Figure 1.2** indicates the increase of interest in published papers acquired from a search in the Web of Science database[12] with the keyword of "climate change" from 1985 to date (July, 2022). A total number of published papers of 449,925 was obtained.
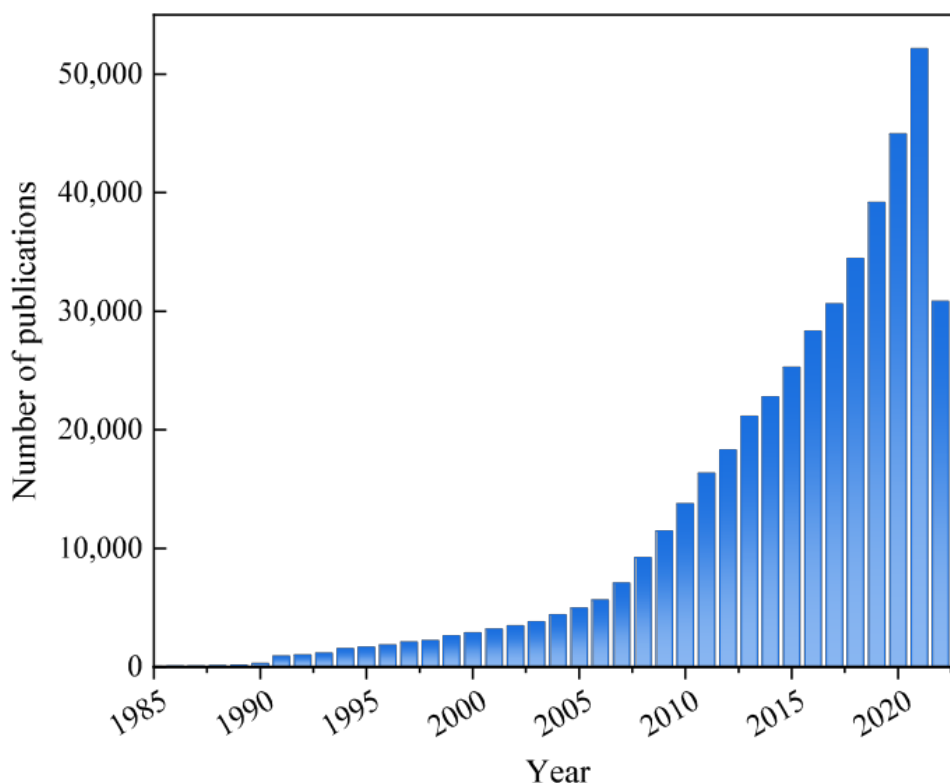
Figure 1.2. The number of published documents (449,925) published each year from 1985 to 2022, obtained from the website of Web of Science[12] using the keyword "climate change".

An urgent need to mitigate CO_2 emissions is essential. CO_2, nowadays, can be reduced in three ways capturing and storage, control of its emission, and chemically conversion and utilization.

1.2 Methanol

Methanol (methyl alcohol), the volatile, colorless liquid (under standard conditions), is the simplest organic alcohol and was isolated for the first time in 1661.[13] Before its industrial production process, it was obtained from the pyrolysis of wood (yield of 10-20L per ton of wood) and charcoal[14] and used mainly as lamp oil and burning fuels. Thanks to feasible industrial production process, methanol plays an important role as a basic chemical and fuel in the world to date, with a global demand of millions of tons per year.[15]

Contrary to NO_X and SO_X species, which emit harmful emissions, methanol is environment-friendly fuel and has less harmful emissions upon its combustion.[16-17] Moreover, the scientific community has widely accepted replacing petroleum derivatives with the methanol economy.[18]

As seen from **Figure 1.3**, the annual methanol production shows steady growth globally and is projected to be 6% per year till 2023, which is projected to reach 109 million tons.[19]
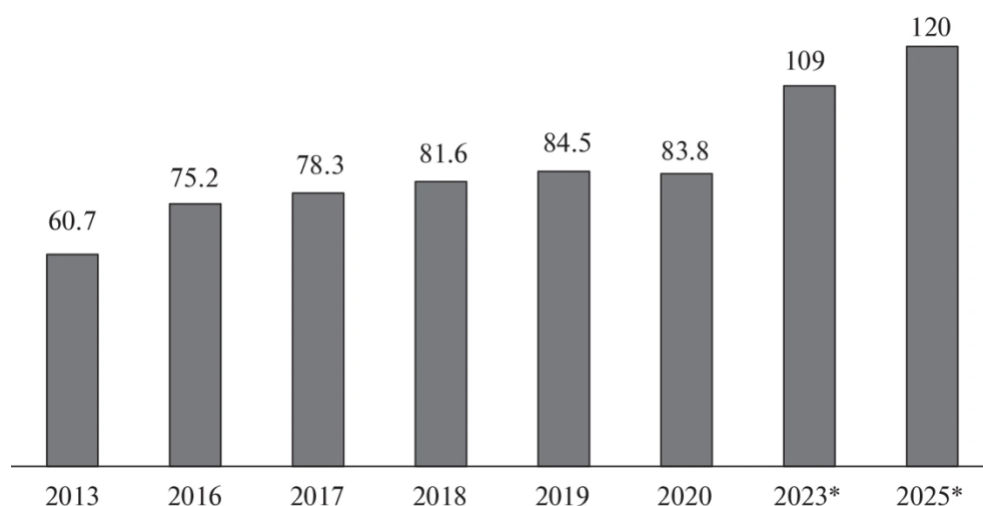
Figure 1.3. Worldwide production of methanol (millions of tons) between 2013 and (forecasted) 2025. The asterisks show forecasts.[19] Reproduced from Ref[15] with permission from Springer Nature, copyright 2022.

A significant amount of methanol (about 80%) is converted to chemicals, such as formaldehyde, fuels, methyl-tert-butylether (MTBE), and acetic acid. As shown in **Figure 1.4**, the major amount of methanol is converted to formaldehyde, which produces many commodity products. MTBE is also used, in modern countries, as the replacement for organolead compounds. The other part of the converted methanol (about 23%) is used to produce fuels and solvents. The direct utilization of methanol as a fuel is still under investigation and is believed to increase the methanol demand in the future.
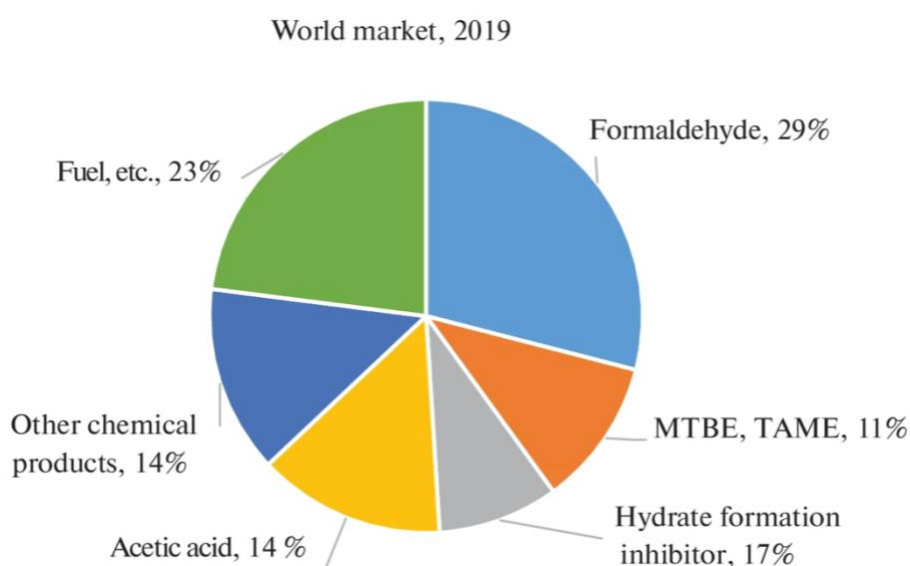
Figure 1.4. Methanol's world consumption in 2019[19]. Reproduced from Ref[15] with permission from Springer Nature, copyright 2022.

Typically, methanol is produced from natural gas or coal. However, it can be produced from sustainable sources, such as biomass, wood, or hydrogenation of captured CO_2 using wind/solar-derived hydrogen. Methanol, in contrast to hydrogen, has fewer difficulties in storing, transporting, and handling as an energy carrier. This brings the necessity of knowing the procedures to produce methanol and its challenges, as will be discussed further.

.1.3 CO and CO$_2$ Hydrogenation

The high consumption of fossil fuels and their limited natural resource urges the need to explore new energy production methods. The captured CO$_2$ can be utilized to produce value-added fuels and chemicals via the catalytic process.[20] For example, methanol can be synthesized from the catalytic hydrogenation reaction (hydrogen used as a reagent) of captured CO$_2$.[21]

The following will discuss the selectivity of the reaction pathways, the nature of active sites, and the reaction mechanism.

1.3.1 Selectivity

Methanol synthesis can follow each of the following procedures: from CO$_2$ hydrogenation (see equation **(1.1)**), the reverse water-gas shift reaction (RWGS) (see equation **(1.2)**), or formation from CO and H$_2$ (see equation **(1.3)**):[22]

$$CO_2 + 3H_2 \rightleftharpoons CH_3OH + H_2O \qquad \Delta H_{298K} = -49.5 \text{ kJ mol}^{-1} \qquad (1.1)$$

$$CO_2 + H_2 \rightleftharpoons CO + H_2O \qquad \Delta H_{298K} = +41.1 \text{ kJ mol}^{-1} \qquad (1.2)$$

$$CO + 2H_2 \rightleftharpoons CH_3OH \qquad \Delta H_{298K} = -90.6 \text{ kJ mol}^{-1} \qquad (1.3)$$

The abovementioned equations show that the methanol synthesis from CO and CO2 hydrogenation (exothermic) is thermodynamically more favorable at relatively lower temperatures.

In the industrial procedure to produce methanol from synthesis gas mixtures (H$_2$, CO, CO$_2$), Cu/ZnO/Al$_2$O$_3$ catalyst at the reaction temperature of 230-300 °C and pressure of 50-120 atm is used.[23] Selectivity of the reaction mechanism concerning CO and CO$_2$ is one of the challenges in methanol synthesis. It has been known that CO is the main carbon source for synthesizing methanol using Cu/ZnO catalysts for many years.[24-26] After the ^{18}CO$_2$, ^{14}CO, and ^{14}CO$_2$ isotopic labeling experiments, both CO and CO$_2$ were determined to produce methanol, by which the CO$_2$ hydrogenation pathway at 220 °C and 250 °C was defined as the primary pathway.[27-28] DFT calculations suggested that about 75% of the methanol synthesis occurred via the CO$_2$ hydrogenation pathway and CO$_2$ is the dominant carbon source.[23] Although the isotope tracing experiments at 240 °C later confirmed this finding, the carbon source shift from CO$_2$ to CO at lower temperatures (160 °C) was also reported.[29] Considering that the CO$_2$ hydrogenation at high conversion is suppressed because of water formation, it is generally accepted that CO$_2$, generated by water-gas shift (WGS) reaction (see equation **(1.4)**), is the main carbon source in the process and converts to methanol afterward.

$$CO + H_2O \rightleftharpoons CO_2 + H_2 \qquad (1.4)$$

The consumption of water produced during methanol synthesis is beneficial for the catalyst's stability. To optimize the methanol selectivity and to prevent the rapid degradation of catalyst, it is crucial to avoid the undesired competitive reverse water-gas shift (RWGS) reaction and the extra water formed as its by-product.

Despite the debates on the selectivity of the reaction pathways in methanol synthesis, discussing the reaction pathways and the nature of active sites is worthwhile.

1.3.2 Active Sites and Mechanism

Although industrial methanol synthesis has been known for almost 100 years, several questions regarding its mechanism are still unanswered.[30] Since methanol synthesis is a structure-sensitive reaction, the choice of the model surface is profoundly essential. On the other hand, the nature of the active site of the copper catalyst in the reaction mechanism of industrial methanol synthesis is not entirely understood yet and is still under debate. It has been reported, by Grabow et al., that Cu(111), which is a thermodynamically stable facet and primarily will be exposed by Cu particles in the methanol synthesis condition (reducing condition), is the stable facet for catalytic methanol synthesis.[23]

In another study, it was suggested that defects could affect the copper surface activity. In the mentioned study, by Behrens et al., on the industrial synthesis of methanol from the hydrogenation of CO_2, using flat Cu(111), stepped Cu(211), and stepped CuZn(211) surfaces, the activity order of CuZn(211) > Cu(211) > Cu(111) was reported. From their results, it can be gained that the high activity of the Cu active site depends on the presence of steps at the surface and Zn at the stepped surface.[31]

The synthesis of methanol through hydrogenation of CO or CO_2 occurs via a series of bond forming and bond breaking processes with the intermediates HCOO, HCO, HCOOH, H_2COOH, H_2CO and CH_3O on the catalyst.[23] The formate pathway (via formate intermediate) and RWGS reaction (followed by CO hydrogenation to methanol with formyl (HCO) and formaldehyde (HCHO) intermediates), are the mostly accepted industrial reaction mechanisms for CO_2 hydrogenation. The schematic of the two pathways is illustrated in **Figure 1.5**.
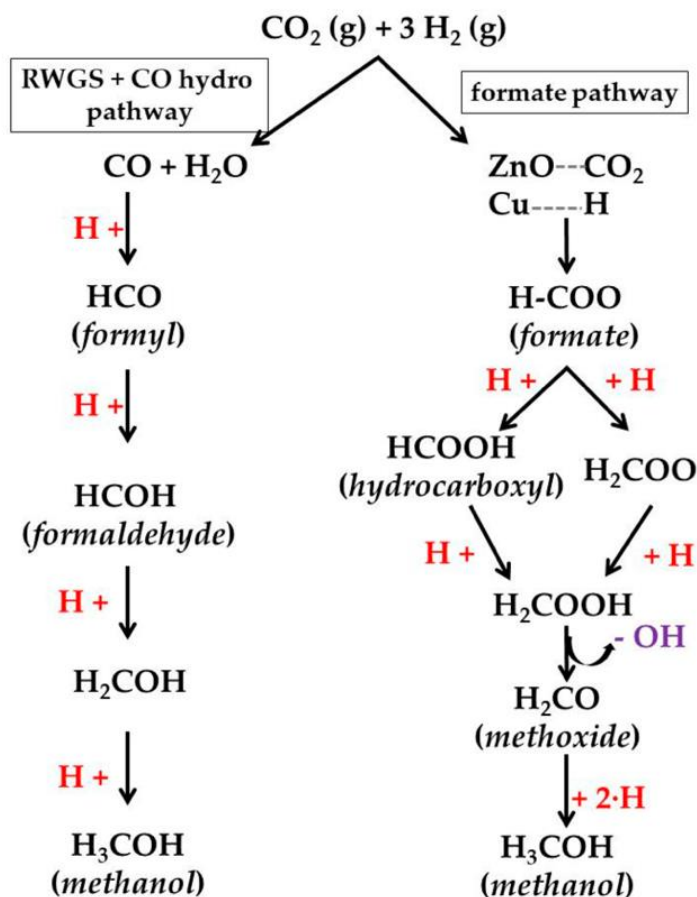
Figure 1.5. Reaction pathways of methanol synthesis from CO_2 hydrogenation using Cu-based catalysts.[32] (adapted from References[33-34])

The methanol production via the formate pathway from CO_2 hydrogenation is followed by the reaction of CO_2 with hydrogen atoms to form intermediates, such as formate (HCOO*), dioxomethylene (H$_2$COO*), formaldehyde (H$_2$CO*) and methoxy (CH$_3$O*).[35] The formate pathway has been proposed, by several studies, for CO_2 hydrogenation reaction using Cu[36-38], Zn[30, 39-40], and Pd[41-42] catalysts. Another reaction mechanism in methanol synthesis from CO_2 hydrogenation is the reverse-water-gas shift reaction (RWGS). Based on this mechanism, CO* is produced from CO_2 hydrogenation via carboxyl (COOH*) intermediate. Afterward, CO* further hydrogenates to form formyl (HCO*), formaldehyde (H$_2$CO*), and methoxy (CH$_3$O*) intermediates, and at the end, methanol is produced.[43]

As methanol synthesis, as well as many other important industrial reactions, benefits and, is based on heterogeneous catalysis and catalysts, the definition of heterogeneous catalysis and catalysts will be introduced in the following.

1.4 Heterogeneous Catalysis

The phenomenon by which chemical reactions are accelerated using catalysts is called catalysis. Catalysis is the fundament of the chemical industries. A suitable catalyst can, thermodynamically, enhance the rate of a reaction rather than the position of the thermodynamic equilibrium. Catalysts are primarily composed of solids. There are three classes of catalysts: enzymatic, homogeneous,

and heterogeneous. As this thesis focuses on the development of heterogeneous catalysts, this class of catalysts will be discussed here.

In heterogeneous catalysis, the catalyst, solid material, is in a different phase from the reactants/products in the reaction. It enables it to be easily separated from the produced products. Reactants (adsorbates) temporarily adsorb on the surface of catalysts, and the catalytic reaction takes place at the reaction mixture and the catalyst surface (at the active sites) interface. Transition metals, reducible- and non-reducible oxides, zeolites, and metal-organic frameworks (MOFs) are different classes of heterogeneous catalysts.

Due to the high price of the catalyst metals (e.g., Pt, Pd, Au, etc.), they are employed in nanoscales, i.e., the nanoparticle metal catalysts supported on inert materials or metal oxides (e.g., Al_2O_3, TiO_2, etc.). Thus, designing highly active and selective heterogeneous catalysts is very important.

1.4.1 Computational Design of Heterogeneous Catalysts

Investigations and understanding of catalytic systems' mechanisms and atomic-scale details to develop new (optimized) catalysts accompanied by obtaining trends and predictions of the reactivity of the systems are feasible through computational methods in catalysis. Besides providing accurate and fast descriptions and predictions for the catalytic systems of interest, the aim of using such theoretical techniques is to simulate and provide information about the properties which are challenging, costly, or even impossible to obtain through the experiments. The close and direct contact and connection between the experimental and computational approaches enhance both sides. The discovery of catalysts accelerates benefiting from the accurate predictions provided by computational modelling of the systems. One of the most standard tools in the core of computational heterogeneous catalysis is the density functional theory (DFT) method (discussed in **Chapter 2**) to simulate the study systems, which can provide accurate results.[44-47]

Although the DFT is very useful for discovering heterogeneous catalysis on transition metal surfaces, it is utilizable for a limited number of systems. It can't be used for all interesting adsorption systems (large systems). Thus there is a need for simple models that can reasonably estimate bond energies and strength of an adsorbate-surface bond in investigating (large) systems. A model was developed to determine the adsorption energy of hydrogenation or dehydrogenation reaction energies of organic molecules on transition metal surfaces, accompanied by a scaling model. The results of the developed model were in agreement with the results of the full DFT calculations, which showed that the model could describe the absolute magnitude and trends in reaction energies. Furthermore, it was demonstrated that by generalizing the scaling relations, the adsorption energy of any hydrogenated species could be used, instead of the reactant (e.g., CO_2), as the reference.[48]

As an example of using such scaling relations in reducing CO_2 to methanol reaction, an approach of reducing the number of energy parameters from 16 to 1 was theoretically performed. The scaling relations between the adsorption energies, and transition-state energies with the adsorption energy of oxygen for all of the hydrogenated forms of CO_2, on different metal surfaces were found. The results provided a complete map of all relevant energies in methanol synthesis according to only oxygen adsorption energy. The comparisons between oxygen adsorption energy values obtained for different transition metals (Cu, Ni, Pd) surfaces and zinc-doped copper step surfaces are plotted in the volcano plot of **Figure 1.6**. The difference between the activity of Cu-Zn and the intermetallic compounds is probably due to the lower number of active sites in the former catalyst. While nickel and palladium bind oxygen strongly and weakly, the elemental copper functions better than the

other two metals. Moreover, the developed one-descriptor model could predict an activity close to the optimum of the mixed-metal system Ni-Ga.[49]
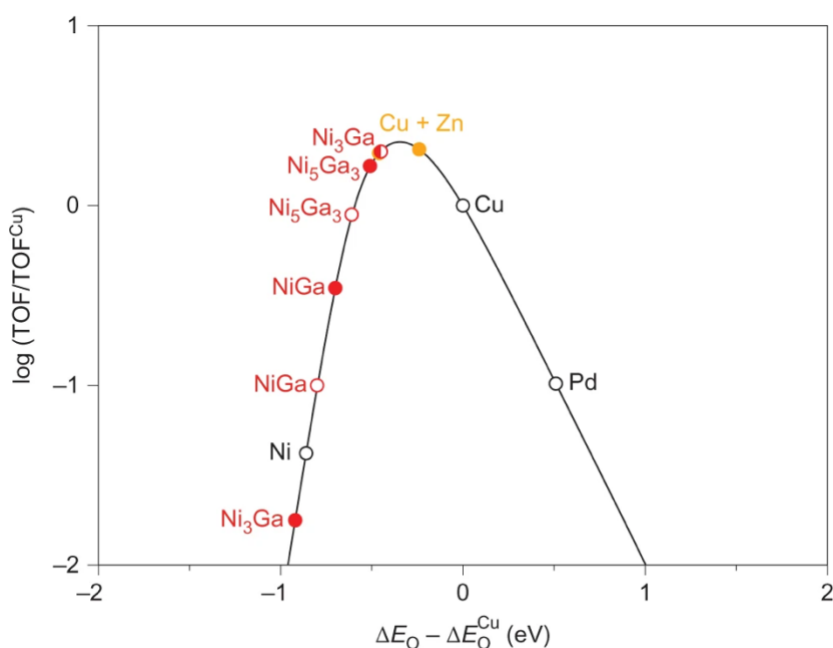

Figure 1.6. Theoretical activity volcano plot for CO_2 hydrogenation to methanol. Turnover frequency (TOF) is plotted against relative oxygen adsorption energy (relative to Cu(211)). Calculated oxygen adsorptions on the stepped 211 surfaces of copper, nickel, and palladium are depicted as open black circles, and Cu + Zn, in orange. ΔE_O for Ni-Ga intermetallic compounds is shown in red. Solid circles illustrate nickel-rich sites, hollow circles gallium-rich sites, and half-open circles mixed sites. The reaction condition simulated are 500 K, 1 bar, and a CO_2:H_2 ratio 1:3. Reproduced from Ref[50] with permission from Springer Nature, copyright 2014.

Industrial catalysts, used in heterogeneous catalytic reactions, are typically metal nanoparticles (with sizes ranging from 3–20 nm) supported on inert or metal oxide supports.[51] Conventionally, the computational modelling method of such catalysts is to simulate reactions on infinite surface metal slabs of different facets, which correspond to the surfaces of larger nanoparticles.[52] However, despite providing helpful comprehension of the systems, these models cannot capture some complexities of real nanoparticle catalysts.[53] Particle size-, shape effects, as well as the effect of supports are neglected in the extended surface models. Here the modelling of real nanoparticle catalysts, as well as the influences of their size, shape, and support, will be discussed.

1.4.2 Nanoparticles in Catalysis

In catalysis, metal catalysts' structure-reactivity depends on their geometric and electronic properties, such as their size, morphology, chemical composition, and higher surface-to-volume ratio.[54] They build an intermediate geometrical class of materials between the solid state of matter and molecular-like structures. The existence of a larger number of active sites available on the surfaces of nanostructured catalysts, due to their higher surface-to-volume ratio caused by the reduction of their size, makes them more efficient than crystal surfaces. Conventionally, nanoclusters are composed of few atoms to hundreds of atoms, and their behavior is more similar to molecules than bulk matter.[55] Despite the importance of the metal clusters in catalysis and technological applications[56], they are not well-designed models for describing the catalysts used in real industrial catalytic reactions, which have sizes ranging from 3 to 20 nm on average.[51, 57]

Despite this fact, theoretically, it is crucial to build models of nanoparticle catalysts to study their properties in high levels of methods such as DFT while keeping the computational costs at a reasonable and reachable limit.

Nanoparticles (NPs) have various applications in different fields of study, such as in energy conversion and storage, chemical industries, and environmental technology.[58-59] NPs provide a large number of surface adsorption sites per catalyst's loading (their higher surface-to-volume ratio) that discriminates them from solid state matters in terms of activity (ideal for catalysis applications). Some unique properties of NPs, such as finite-size (defined as energetically competitive isomers) and electronic effects, bring about special catalytic properties. For instance, gold nanoparticles exhibit an intense activity towards a given reaction, despite gold being a highly inert metal.[60] Therefore, it is essential to extensively consider the unique effects of/on the metal nanoparticles.

1.4.3 Particle Size and Shape Effect

Controlling the size and shape of the nanoparticles, which can ensure an appropriate surface-to-volume ratio and increase the active sites, to enhance the activity, selectivity, and durability of the catalyst in catalytic reactions is extremely important.

As mentioned in the previous section, the existence of a finite-size effect is one of the challenges. This challenge can, sometimes, lead to strong deviations between the behavior of smaller clusters or particles with the bulk-like systems, known as "quantum size effects" (QSE).[61-62] Moreover, the selectivity and activity of the NP catalysts, depending on how they interact with adsorbates, will alter according to the changes of their size and morphology. Consequently, the number and type of adsorption sites and the active facets changes.

The alteration of the surface structures of the metal NPs with sizes between 2 nm to 10 nm due to the change of the fraction of surface atoms forming different adsorption sites is expected in catalytic reactions.[63-66] In agreement with this fact, the strong particle size effect of the metal particles with sizes ranging between 2 nm to 10 nm on the activity and selectivity of some catalytic reactions, such as methanation, Fischer-Tropsch synthesis, ammonia synthesis, and methanol synthesis has been found.[67-73]

In methanol synthesis from CO and CO2 hydrogenation, sensitivity or insensitivity of the reaction towards the structure of the copper surface has been debated for decades.[74] However, the structure-sensitivity of industrial-relevant methanol synthesis using an industrial copper catalyst, regardless of the presence or absence of ZnO or Zn-silicate promoters, was proved. As shown in **Figure 1.7**, for copper NPs smaller than 8 nm, a significant decrease in surface-specific activity is observable.
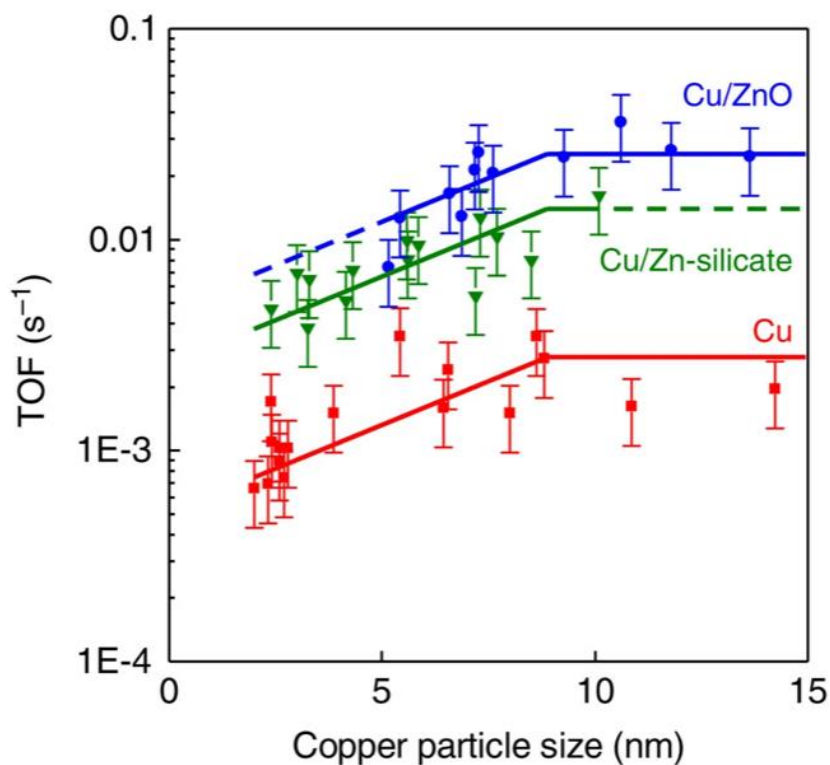
Figure 1.7. The surface-specific activity (TOF) for methanol synthesis after 2-10 hours on stream at 260 °C and 40 bar against catalyst's particle size. Catalyst are: copper containing, that is, Cu/SiO_2, $Cu/(functionalized)SiO_2$ and Cu/C (red), containing Cu/Zn-silicate, that is, $CuZn/SiO_2$ (green), and containing Cu/ZnO, that is, $Cu/ZnO(/Al_2O_3)$ and $CuZn/C$ (blue). Error bars indicate the s.d. in the methanol synthesis activity (35%).[73]

There is a big difference between the number of theoretical studies of the adsorption properties of large systems (close to the bulk limit) and the small metal particles. As an example of the large systems studied, it was suggested, by Rösch et al., that the bulk limit was reached for unrelaxed big clusters (260 atoms palladium particle).

As another example, the adsorption energy calculations for CO and O on gold nanoparticles ranging from 13 to 1415 atoms (0.8-3.7 nm) with massively parallel computing on 32,768 cores proved that the bulk surface properties were obtained for clusters larger than 560 atoms. Furthermore, finite-size effects for clusters less than 560 atoms and quantum-size effects for the smallest clusters were observed.[61]

a)

b)
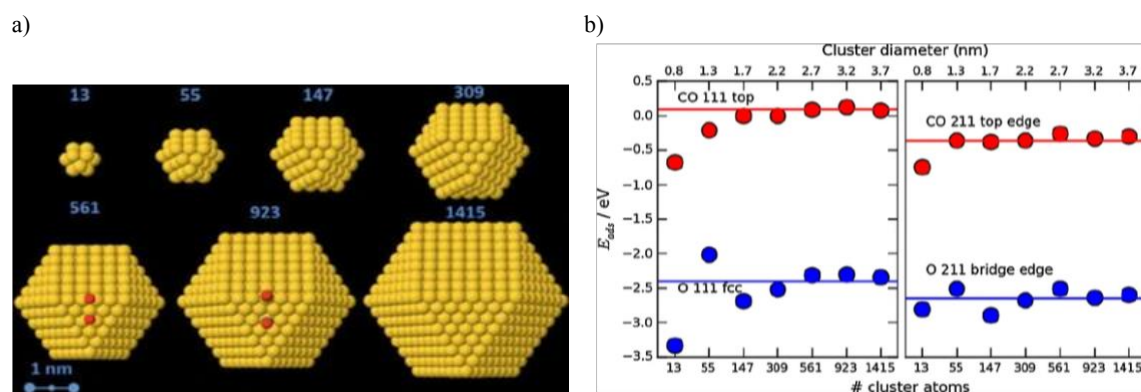
Figure 1.8. (a) All closed shell cuboctahedral gold particles up to 1,415 atoms shells[75-81]. The two adsorption sites for the two adsorbates are shown (O fcc site or edge site on the 561 atom cluster and CO top site on the 923 atom cluster, as close to the center of the edge/facet as possible). (b) Calculated CO and O adsorption energies on the (111) facet and at the edge of fixed-geometry clusters against the cluster size. The adsorption energies for (111) and (211) slab surface calculations are shown as horizontal lines. Reproduced from Ref[61] with permission from Springer Nature, copyright 2011.

To measure the electronic effects of the pure clusters with respect to the variation of their sizes and to determine the effects of coupling to the lattice, the clusters were relaxed with and without the presence of the adsorbate, respectively. As can be seen from **Figure 1.8 (b)**, the adsorption energies are dependent on the size of the clusters in fixed-geometry structures. Generally, it could be gained that the smaller the particle, the stronger the adsorption will be, except in the case of Au_{55}, which was found, both experimentally and theoretically, to be unreactive towards oxygen.

These effects were confirmed later, by Li et al., by studying the catalytic properties of fixed free-standing platinum metal clusters ranging from 13 to 1415 atoms. It was reported that the adsorption energies of clusters with 147 Pt atoms and above were similar to the values obtained from the related infinite surface.[82]

1.4.4 Support Effect

Most industrial catalytic reactions are based on supported metal nanoparticle catalysts. The high surface free energy of metals[83] can be reduced by dispersing on the high surface area of supports. It is known that the properties of the support, such as reactivity, available surface area, etc., impact the metal particle size, charge, and morphology, providing special active sites over the metal-support boundary[84]. Consequently, this can have influences on the metal nanoparticles' catalytic properties. The morphology of the support materials is important in enhancing the performance and stability of any metal NP catalyst.[85-86] The supports in heterogeneous catalysis can be carbon[73], carbon nanofibers[87], zeolites[88], alumina[89], and metal oxides such as TiO_2[90]

The presence of support significantly influences most of the catalytic reactions. For example, it has been reported that the rate of water-gas shift reaction (WGS) rises around an order of magnitude per mole of Au catalyst by using TiO_2 support instead of Al_2O_3.[91]
In a recent study, it has been revealed that in the WGS reaction using a gold nanowire, the activation barrier of water decreased from ~2 eV on a clean Au(111) surface to ~0.75 eV at Au supported on MgO(100).[92]

Another study demonstrated the key role of zirconia (ZrO_2) support on methanol synthesis by CO_2 hydrogenation. The investigated model consisted of supported copper particles (Cu_{38}) on zirconia. The adsorption energies on the modelled metal oxide supported catalyst were compared to the results obtained with pure Cu(111) surface and zirconia slab model.
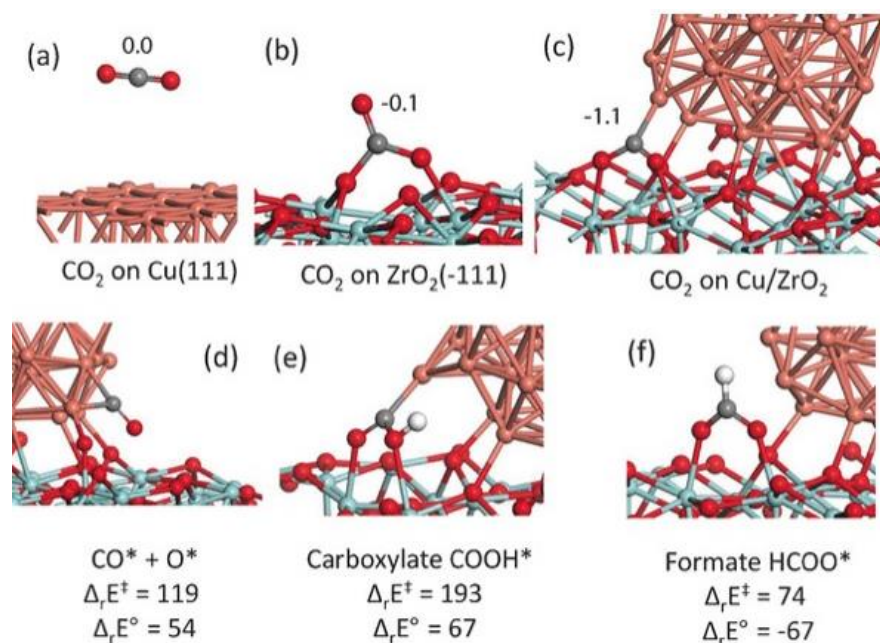
Figure 1.9. a–c) Optimized structures of CO_2 adsorbed on Cu(111) (a), on (monoclinic) m-ZrO_2 ($\bar{1}11$) (b), and at the interface between copper and zirconia (c). The Bader charge on CO_2 molecules are shown. d–f) Possible structures of intermediates at the interface between copper and zirconia: CO* and O* (d), carboxylate COOH* (e), and formate HCOO* (f). Activation barriers and formation enthalpy from adsorbed CO_2+H_2 are given in kJ mol^{-1}. Atom key: zirconium (cyan), oxygen (red), copper (orange), carbon (gray), hydrogen (white).[93]

As can be seen from **Figure 1.9**, while CO_2 does not adsorb on Cu(111) surface and binds to the zirconia surface as carbonate, by adopting a bent structure, it adsorbs on the interface between copper and zirconia (**Figure 1.9 a-c**). The transformation of CO_2 to CO, carboxyl, and formate on the interface between copper and zirconia are depicted in **Figure 1.9 (d)-(f)**. It was concluded that for the conversion of formate, which was the main intermediate of the reaction, to methanol, the use of Cu/ZrO_2 is crucial.[93]

1.5 Scope of the Thesis

This thesis aims to investigate some important and under debate factors influencing the performance and properties of transition metals catalysts, which can consequently affect the catalytic reactions. As an example of such factors, particle size and shape effects and the effect of support can be pointed out. While heterogeneous catalysis is mainly based on transition metal nanoparticles, it is important to study and understand their intrinsic properties and external factors on their performance. However, because the size scale of the catalysts investigated in reality (experimental studies) and computationally (mostly based on DFT calculations) are much different, developing computational models and methods to accurately predict the systems' properties is crucially important. At the same time, lowering the consumption of computing resources also possesses great

importance. This thesis focused on developing such cost-efficient models of nanoparticles and investigating the factors mentioned before on their performance in important catalytic reactions, such as methanol synthesis from CO and CO_2 hydrogenation.

The contents of this thesis can be summarized as follows:

- Chapter 3, Particle Size Effect in Coinage Metals: Here the models of copper, silver and gold clusters and nanoparticles with different sizes were modelled. The accuracy of the fixed-geometry models, by means of intrinsic properties as well as oxygen adsorption energy, were compared with the relaxation of the structures. Proving the good performance of the modelled systems. Also the particle size effect as well the quantum size effect were investigated.
  - This chapter is based on the publication: **Hakimioun, A.H.**, Dietze, E.M., Vandegehuchte, B., Curulla-Ferré, D., Joos, L., Plessow, P. N., Studt, F. *Catalysis Letters* 151, 3165–3169 (**2021**).

- Chapter 4, Particle Size Effect in other Transition Metals: The utilized models of the particles in the previous chapter were used for the first three elements of groups 9 and 10 of the periodic table of elements to study their particle size effect on the adsorption energy of oxygen atom as a probe atom. Furthermore, the obtained results were compared to the ones of coinage metals.
  - This chapter is based on the publication: **Hakimioun, A.H.**, Kaźmierczak, K., Vandegehuchte, B., Curulla-Ferré, D., Plessow, P. N., Studt, F., *in preparation*.

- Chapter 5, Metal-Support Interactions in Heterogeneous Catalysis: Here the influence of non-reducible oxidic support (magnesium oxide (MgO)) on the properties of copper particles of different sizes and shapes was investigated. In addition, the effects of the particle's size and shape were studied. It was emphasized that the support could represent some influence only at the adsorption positions at the direct interface between the support and the particle. The comparison between these factors proved the higher effect of the particle size than the other two factors.
  - This chapter is based on the publication: **Hakimioun, A.H.**, Kaźmierczak, K., Vandegehuchte, B., Curulla-Ferré, D., Plessow, P. N., Studt, F. *ACS omega* 8, 11 (**2023**): 10591-10599.

- Chapter 6, Scaling Relations in Adsorption Energies: In this chapter, the adsorption energies of different intermediates involved in the catalytic CO_2 hydrogenation reaction to methanol using the cost-efficient models of copper particles (studied in **Chapter 3**) were calculated. The trends in the adsorption energies, as well as the influence of the particle size were shown. In addition, the impact of spin polarization on the obtained results is discussed.
  - This chapter is based on the publication: **Hakimioun, A.H.**, Kaźmierczak, K., Vandegehuchte, B., Curulla-Ferré, D., Plessow, P. N., Studt, F., *in preparation*.

- Chapter 7, Particle Size Effect in CO_2 Hydrogenation: This chapter identifies the influence of particle size of copper catalysts on the selectivity of CO_2 hydrogenation reaction toward the production of methanol. A combination of DFT and experimental methods (carried out by performed by Laura Barberis and Nienke L. Visser, both at Utrecht university) were

applied to shed light on one of the most debated topics in the copper-based catalytic reaction of CO_2 hydrogenation, proving the structure sensitivity of the reaction.

- This chapter is based on the publication: Barberis, L., **Hakimioun, A.H.**, Plessow, P.N., Visser, N.L., Stewart, J.A., Vandegehuchte, B., Studt, F., de Jongh, P. *Nanoscale* 14, 37 (**2022**): 13551-13560.

2 Theoretical Methods

2.1 Introduction

Computational modeling and simulation of materials have benefited from the computers' developments over time, resulting in the appearance of more applicable softwares that can significantly help develop and refine the materials and their handling. Thus, it is important to understand definitions of the terms 'model' and 'simulation'.

A' model' is used to idealize the real behavior of a system by, for instance, approximately describing it depending on some empirical and/or physical deductions. Models usually arise from a set of concepts transferred into mathematical relations to calculate quantities or behaviors.

The 'simulation', on a modelled system is utilized to study the influences of external forces and constraints on it. Therefore, it is essential to know that the simulations are based on models. The accuracy of the simulations of the real system models depends on several factors, such as the simulation methods used.

In general, Computational Materials Science (CMS), applying computer-based modeling and simulation of materials, can help understand and predict materials' behavior. However, the predictions, the models' accuracy, and the outcomes of the calculations can be validated by experiments on real systems. A strong tie between the theory and the experiment could make the CMS methods more robust and reliable. At the same time, by investigating phenomena that cannot be reached and observed by experiments, CMS can provide a deeper understanding of a materials system.

A large range of lengths of the systems and time scales are among the challenges in modelling and simulation of materials. The length scales of the studying systems can vary from nanometers scale to the meters scale of structures. Consequently, the time scales also vary between the ranges of femtoseconds to the decades. Based on this fact, not a single technique can be used to study all the different scales; thus, appropriate methods (ranging from structural mechanics to quantum mechanics) are used to study specific physical phenomena for given ranges of time and length scales.

At the length scales ranging from 1 Å (10^{-10} m) to 100 microns (10^{-4} m) the behavior of the materials is dominated by atomic bonding. Thus, to study the underlying electronic structure of the atomic bonding and calculate the distribution of electrons of the constituent atoms, utilizing quantum

mechanics is required. In this chapter, a brief theory basic of the employed methods in the thesis will be introduced.[94]

In the following, a brief introduction of conventional DFT using plane wave functions and some additional key concepts based on Refs[94-98], will be discussed.

2.2 Quantum Mechanics of Multi-Atomic Systems (Nanoparticles and Surfaces)

The origin of quantum mechanics can be traced back to the beginning of the twentieth century and the failure of classical physics in predicting and describing microscopic phenomena (e.g., photoelectric effect, black-body radiation, etc.). The quantum mechanical treatments of all electronic structures of materials are based on the Schrödinger equation. The description of the motion of nuclei and electrons and the interactions in their stationary states can be represented by the time-dependent Schrödinger equation:

$$i\hbar \frac{\partial}{\partial t} \Psi(r,t) = \left(\frac{-\hbar}{2m} \nabla^2 + V(r,t) \right) \Psi(r,t) = (\hat{T} + \hat{V}) \Psi(r,t) = \hat{H}(r,t) \Psi(r,t) \quad (2.1)$$

where $\hat{H}$ is the Hamiltonian operator, Ψ is the wave function, a description for the system's state, i is the imaginary number unit, $\hbar$ is the reduced form of Planck constant ($\hbar = h/2\pi$), t is the time, r is the vector of position including all the positions of particles in the system, ∇ is the spatial differential operator, m is the particle's mass. The system's energy can be found from the operation of the Hamiltonian operator (divided into the potential operator $\hat{V}$ and the kinetic operator $\hat{T}$ components). In the cases where the potential is constant or has a slower variation with time, the Hamiltonian is assumed to be time-independent, and the Schrödinger equation can be written as:

$$\Psi(r,t) = \Psi(r) \cdot \exp\left(\frac{-iEt}{\hbar} \right) \quad (2.2)$$

E is the system's energy calculated from the operations on the wave function.

The energy of a multi-atomic system (consisting of nuclei and electrons with vector positions of R and r, respectively), primarily investigated in computational chemistry using quantum mechanics, can be found applying the time-independent Hamiltonian on the wave function $\Psi(r, R)$. The Hamiltonian for a system of N electrons and M nuclei is depicted as:

$$\hat{H} = -\sum_{i=1}^{N} \frac{1}{2} \nabla_i^2 - \sum_{A=1}^{M} \frac{1}{2M_A} \nabla_A^2 - \sum_{i=1}^{N} \sum_{A=1}^{M} \frac{Z_A}{r_{iA}} + \sum_{i=1}^{N} \sum_{j>i}^{N} \frac{1}{r_{ij}} + \sum_{A=1}^{M} \sum_{B>A}^{M} \frac{Z_A Z_B}{R_{AB}} \quad (2.3)$$

where M_A is the ratio between the masses of nucleus (A) and an electron, Z_A the atomic number of nucleus. The first and second terms in Eq. **(2.3)** correspond to the operators for the kinetic energies of the electrons (T_e) and of the nuclei (T_N), respectively. The coulomb attraction between nuclei and electrons (V_{Ne}) is represented in the third term and the fourth and fifth terms illustrate the

potential energies caused by the repulsion between electrons (V_{ee}) and between nuclei (V_{NN}), respectively. Thus, the equation **2.3** can be summarized as:

$$\hat{H} = \hat{T}_e + \hat{T}_N + \hat{V}_{Ne} + \hat{V}_{ee} + \hat{V}_{NN} \tag{2.4}$$

With regards to the fact that the mass of nucleus is much heavier (about 1800 times) than of the electron, the electron moves with orders of magnitude faster than the nucleus. Thus, using the Born-Oppenheimer approximation, the electrons can move in their field while the nuclei are considered as static particles. In computational chemistry, the Born-Oppenheimer approximation is a key principle. Therefore, the solution to the Schrödinger equation for a multi-atomic system would be simplified as the kinetic energy of the nuclei can be neglected, and also, the term for the nuclei repulsion becomes constant. The equation **(2.3)** can be simplified, and the electronic Hamiltonian will be depicted as:

$$\hat{H}_{elec} = -\sum_{i=1}^{N} \frac{1}{2} \nabla_i^2 - \sum_{i=1}^{N} \sum_{A=1}^{M} \frac{Z_A}{r_{iA}} + \sum_{i=1}^{N} \sum_{j>i}^{N} \frac{1}{r_{ij}} \tag{2.5}$$

Thus, the electronic Schrödinger equation including the electronic Hamiltonian operator and wave function which is dependent on the coordinates of the nuclei R and of the electrons r will be:

$$\left[\hat{T}_e + \hat{V}_{ee} + \hat{V}_{eN}\right] \Psi^{elec}(r, \{R\}) = E_e \Psi^{elec}(r, \{R\}) \tag{2.6}$$

which $\{R\}$ shows the parametrical dependence of the electronic wave function on R. Therefore, the total energy of the system can be derived by the summation of E_{elec} and E_{nuclei}.

2.3 Density Functional Theory (DFT)

2.3.1 Hohenberg-Kohn Theorems

Many different classes of methods to find variational solutions for the equation **(2.5)** are available. Among them, density functional theory (DFT) provides a promising way to study the ground state physical properties of multi-atomic systems at their lowest energy configurations by considering their electronic densities $\rho(r)$ in 3 dimensions rather than the wave function. DFT, which is used vastly in computational materials science studies, e.g., catalysis, was presented from the first model in 1927 by Thomas and Fermi[94]. DFT is constructed based on the two theorems of Hohenberg and Kohn[99] in which the electrons in the system move by the influence of an external potential v_{ext}. Their first theorem states that the external potential and, consequently, the total energy is a unique functional (function of a function) of the electron density (see equation **(2.7)**).

$$E[\rho(r)] = \int \rho(r) v_{ext}(r) dr + F[\rho(r)] \tag{2.7}$$

where $E[\rho(r)]$ is the energy functional, $v_{ext} = -Z/r$ (where Z is the nuclear charge), $F[\rho(r)]$ is the universal functional of the electron density (electronic contributions $T[\rho] + V[\rho]$). In other words, the energy of interaction between all the electrons and the nucleus can be found from the

integral of $\rho(r)$ as a function of r, the distance between the electron and nucleus, times the electrostatic potential (external potential) of an electron and nucleus at the distance r between them. Their second theorem states that the ground state electronic density is the density that minimizes the energy functional.

2.3.2 Kohn-Sham Scheme

Although the two theorems of HK were powerful, they could not provide a method of computing the ground state density of systems of interest. To solve this issue, in 1965, Kohn and Sham introduced the so-called Kohn-Sham (KS) theory by changing the many-body problem into a system with N non-interacting particles. Based on their developed model system, non-interacting electrons move by the influence of an external effective potential which results in the energy of the system minimizing the ground state, which is identical to the many-body interacting system.

$$v_{KS-DFT}(r) = v_{ext}(r) + v_{Coul}(r) + v_{XC}(r) \tag{2.8}$$

where $v_{KS-DFT}(r)$ is the Kohn-Sham potential, $v_{ext}(r)$ is the external potential, $v_{Coul}(r)$ is the Coulomb potential and the $v_{XC}(r)$ is the exchange-correlation potential which is derived from the functional derivative of the $v_{XC}(r)$:

$$v_{XC}(r) = \frac{\delta E_{XC}^{KS}}{\delta \rho(r)} \tag{2.8}$$

The ground state energy functional is determined by:

$$E_{KS-DFT}[\rho] = T_S[\rho] + E_{Ne}[\rho] + J[\rho] + E_{XC}[\rho] \tag{2.9}$$

The equation **(2.8)** is divided into known and unknown parts. The kinetic energy of non-interacting electrons $T_S[\rho]$, the classical Coulomb electron-electron interaction energy $J[\rho]$, and the attraction energy between the nuclei and electrons $E_{Ne}[\rho]$ constitute the known part and the unknown part is the so-called exchange-correlation term $E_{XC}[\rho]$, which summarizes all the corrections between the kinetic and Coulomb energies and the correct calculated values. The kinetic energy of the non-interacting system is given by:

$$T_S[\rho] = -\frac{1}{2} \sum_i^N \nabla^2 \phi_i(r) \tag{2.10}$$

where $\phi_i(r)$ are the so-called Kohn-Sham orbitals and are the eigenfunctions of the following eigensystem equation:

$$\left(-\frac{1}{2}\nabla^2 + v_{KS-DFT}(r)\right)\phi_i(r) = \varepsilon_i\phi_i(r) \tag{2.11}$$

As ε_i are the KS-orbital energies non-interacting single electron wave function. The electron density of a N electrons system is then assumed by KS as a sum of one-electron KS-orbitals:

$$\rho(\mathrm{r}) = \sum_i^N \phi_i^2(\mathrm{r}) \tag{2.12}$$

It must be noted that the KS-orbitals are obtained from mathematical approaches, and their energies have no direct physical meaning (except HOMO level). The KS-potential is dependent on the density, and to reach convergence in the electron density, a self-consistency procedure in solving the equation **(2.11)** is needed.

2.3.3 Exchange-Correlation Functionals

In equation **(2.9)**, the term $E_{XC}[\rho]$ representing the exchange-correlation (XC) functional is the only unknown quantity, which includes all the corrections to the approximate KS-Hamiltonian. The $E_{XC}[\rho]$ is usually constructed from the sum of exchange and correlation functionals:

$$E_{XC} = E_X + E_C \tag{2.13}$$

Due to its unknown form, a significant area for DFT studies has been designated to develop and test the accuracy and related computational cost of approximations of the XC functionals. The available long list of approximated XC functionals with different complexities brings about the vital delicacy of choosing the right XC functional in the computational studies of the systems. The more sophisticated approximation methods increase the accuracy of the results obtained from DFT and, on the other hand, increase the computational cost. The "Jacob's ladder", proposed by Perdew[100] provides a vivid illustration of the relation between the accuracy of XC functional and the computational cost (see **Figure 2.1**). According to the scheme, functionals are sorted from the Hartree approximation (earth) to the exact approximation of XC functional (heaven of chemical accuracy). In addition, based on the nature of approximations, the functionals are categorized into *empirical* and *non-empirical*. In the former category, the functionals are generated based on the fitting obtained from experimental results of atomic properties. Hence, only physical rules and theories constitute the latter category.

Figure 2.1. Illustration of Jacob's Ladder of DFT accuracy. Reproduced from Ref[101] with permission from Springer Nature, copyright 2020.

The so-called Local Density Approximation (LDA), introduced by Kohn and Sham, is the oldest and simplest approximation.[102-104] In this approximation, the XC-energy density is approximated with the XC-energy density of the homogeneous electron gas model with the same density as the local density of the system of study.

$$E_{XC}^{LDA}[\rho] = \int \rho(\mathrm{r})\varepsilon_{XC}(\mathrm{r})dr \qquad (2.14)$$

where ε_{XC} is the exchange-correlation energy function for electron density $\rho(\mathrm{r})$. The exchange expression is exactly known analytically (see equation **(2.15)**) and the correlation part can be fitted to more accurate quantum mechanical simulations (e.g., Quantum Monte-Carlo (QMC) simulations).

$$\varepsilon_{XC}(\mathrm{r}) = -\frac{3}{4}\left(\frac{3\pi(\mathrm{r})}{\pi}\right)^{\frac{1}{3}} \qquad (2.15)$$

Local theories are still among the most common corrections applied to exchange-correlation energy function. However, these corrections are not only based on the local values of the electron density

but also the local value of the gradient of the local density. These classes of XC functionals, widely used in DFT that increase the accuracy, complexity, and computational cost, are designated as *generalized gradient approximations* (GGA). It is represented as the general form of:

$$E_{XC}^{GGA}[\rho] = \int \rho(\mathrm{r})\varepsilon_{XC}(\rho, \nabla\rho)d\mathrm{r} \tag{2.16}$$

where $\nabla\rho(\mathrm{r})$ is the gradient of electron density. The GGA functionals, which sit on the second rung of Jacob's ladder, are the second generation XC functionals and exhibit better results than LDA for studies of different properties, for instance, geometry optimizations and the energies of the ground states of atoms and molecules. A vast number of GGA functionals have been developed and are available to date, which provides more options for theoreticians to investigate their different systems of interest. Among them, Perdew and Wang (PW91)[105], Perdew-Burke-Enzerhof (PBE)[106], BLYP[105, 107-108] are the most common functionals.

The meta-GGA functionals (e.g., TPSS[109]), sitting on the next ladder rung, were developed by including the second derivative of the density and kinetic energy densities with respect to space. They have shown better performance than LDA and GGA functionals in studies of molecular properties in the gas phase.[110-113]

By adding the "exact exchange" contribution, obtained from the calculations using Hartree-Fock (HF), to the DFT exchange and correlation to reduce the self-interaction (interaction of an electron with itself) error, the hybrid functionals were developed. They constitute the fourth generation of the XC functionals, and B3LYP (with 20% HF exchange)[114-116] and PBE0 (with 25% HF exchange)[117] are examples of such functional.

2.3.4 Van-der-Waals (vdW) Interaction

The van der Waals interactions (also known as London dispersion) are types of electron correlations. By definition, the van der Waals interaction includes the dipole-dipole (electrostatic interaction in a polar system), dipole-induced dipole (interaction between nonpolar and polar systems), and dispersion interactions. In a system where two atoms are very close, the van der Waals interactions are repulsive owing to the repelling forces between two electrons (with negative charges). The general equation of the van der Waals interactions between two atoms (A and B) is[118]:

$$E_{\mathrm{vdW}}(r_{\mathrm{AB}}) = E_{\mathrm{repulsion}}(r_{\mathrm{AB}}) - \frac{C^{\mathrm{AB}}}{(r_{\mathrm{AB}})^6} \tag{2.17}$$

where E_{vdW} is the van der Waals energy, the term C^{AB} is a constant, r_{AB} is the distance between atom A and B and $E_{\mathrm{repulsion}}$ is the repulsive energy. In DFT, most conventional GGA correlation functionals contain short-range correlations and long-range correlations, such as dispersion interactions, that are neglected. Depending on the functional used in DFT studies, dispersion corrections are applied differently. DFT symmetry-adapted perturbation theory (DFT-SAPT)[119] is one of the methods of incorporating dispersion interactions with KS-DFT by calculating only

intermolecular electron correlations. There are also developed vdW functionals that directly include dispersion corrections, e.g., ALL-functional or VV09-functional.[120-121]

There are some kinds of semi-empirical dispersion corrections to the functionals in DFT (DFT-D1, DFT-D2, and DFT-D3)[122-124], which are generated by adding modifications to, e.g., GGA functionals. The dispersion-corrected DFT-D3 energies are defined as:

$$E_{\text{DFT}-\text{D3}} = E_{\text{KS}-\text{DFT}} - E_{\text{dispersion}} \tag{2.18}$$

where $E_{\text{dispersion}}$ is the dispersion correction obtained from the sum of two- and three body terms ($E^{(2)}$ and $E^{(3)}$). The two body is more important term and is given by:

$$E^{(2)} = \sum_{AB} \sum_{n=6,8,10} s_n \frac{C_n^{AB}}{r_{AB}^n} f_{d,n}(r_{AB}) \tag{2.19}$$

with the term C_n^{AB} being the averaged dispersion coefficients of order n=6,8,10,… for atom pair AB with the internuclear distance of r_{AB}. s_n are scaling factors (adjusted for $n > 6$). To avoid near singularities for mid-range double-counting effects and to determine the dispersion correction's range, damping functions $f_{d,n}$ are applied.

2.3.5 BEEF-vdW Functional

Among the developed functionals, PBE[106] and RPBE[125] (mostly used for surface adsorption) are very popular. However, the non-local vdW interactions, like dispersion forces, are not included in these functionals. Consequently, throughout this thesis, the Bayesian Error Estimation Functional with vdW (BEEF-vdW) is employed as the main functional. The BEEF-vdW exchange-correlation functional reliably describes both the short- (covalent bonds) and long-range van der Waals interactions between molecules and surfaces[126]. The BEEF-vdW was chosen for its performance and correctly describing adsorption energies[127] and transition states of adsorbates on metal surfaces. The exchange energy density is defined as the exchange energy density of the uniform electron gas ϵ_x^{hom} and an exchange enhancement factor in a basis M_x Legendre polynomials

$$E_{xc}^{GGA}[\rho, \nabla\rho] = \sum_m a_m \int \epsilon_x^{hom}(\rho) B_m[t(s)] \, d\text{r} \tag{2.20}$$

with a_m the expansion coefficients, B_m the Legendre basis function of order 0 to $M_x - 1$ in $t(s)$, a transformed reduced density gradient.

To describe the effects of electron correlation, a linear combination of local Perdew-Wang[128] LDA correlation functional, semi-local Perdew-Burke-Ernzerhof (PBE)[129] correlation and a non-local correlation of vdW-DF2[130] type, were modelled. The general BEEF-vdW XC functional can be written as:

$$E_{xc}^{\text{BEEF-vdW}} = \sum_{m=0}^{M_x-1} a_m \int \epsilon_x^{LDA} B_m[t(s)] dr + \alpha_C E_C^{LDA} + (1 - \alpha_C) E_C^{PBE} + E_C^{NL} \quad (2.21)$$

where α_C are the correlation mixing parameter which are adjustable parameters and E_C^{NL} is related to the nonlocal correlation.

2.4 Plane waves and Basis set

Basis sets are necessary compartments in practically solving the electronic Schrödinger equation. Typically, the wave function can be written as the sum of a set of functions (basis functions), denoted as the basis set. Gaussian, plane wave, Slater type orbitals, exponential, polynomial, numeric atomic orbitals, etc., are some types of basis functions. The Gaussian basis sets are based on the Linear-Combination-of-Atomic-Orbitals (LCAO) approach in which the molecular orbital ψ_i is described as the linear combination of one-electron functions ϕ_μ (basis set), of Slater[131] or Gaussian[132] type:

$$\psi_i(r_j) = \sum_\mu C_{i\mu} \phi_\mu(r_j) \quad (2.22)$$

The choice of basis set is dependent on the required accuracy as well as the computational cost. The choice of the wave function also depends on the type of system of study. For the periodic systems, e.g., extended surfaces, the plane wave basis sets have usually been used.

2.4.1 Bloch's Theorem

Since the structures of the crystal lattices and surface systems are periodic, the external potential and the electronic structure will also be periodic. Thus, the theoretical solution for the periodic systems is based on Bloch's theorem[133]. According to Bloch's theorem, all the solutions to the Schrödinger equation for a periodic potential must be continuous throughout the space. In other words, the wave function for an electron can be defined as a product of the lattice periodicity $u(\boldsymbol{k}, \boldsymbol{r} + \boldsymbol{R}) = u(\boldsymbol{k}, \boldsymbol{r})$, and a plane wave $\exp(i\boldsymbol{k} \cdot \boldsymbol{r})$:

$$\psi(\boldsymbol{k}, \boldsymbol{r}) = \exp(i\boldsymbol{k} \cdot \boldsymbol{r}) \cdot u(\boldsymbol{k}, \boldsymbol{r}) \quad (2.23)$$

with $\boldsymbol{R}$, $\boldsymbol{r}$, $\boldsymbol{k}$ and $u(\boldsymbol{r})$ being the direct lattice-, position- and wave vectors and lattice-periodic factor, respectively. Plane waves are set of functions which satisfy Bloch's theorem condition as the result of expansion of lattice periodic term with a reciprocal lattice vector $\boldsymbol{G}$.

$$\psi_j(\boldsymbol{k}, \boldsymbol{r}) = \sum_{\boldsymbol{G}} C_{j,\boldsymbol{k},\boldsymbol{G}} \cdot \exp(i(\boldsymbol{k} + \boldsymbol{G})\boldsymbol{r}) \quad (2.24)$$

where $C_{j,\boldsymbol{k},\boldsymbol{G}}$ are the expanding coefficients and the lowest energy solutions can be reached by varying these coefficients. Practically, a finite number of plane waves can be used, which is sufficient owing to the existence of only discrete G due to the lattice periodicity, and the coefficients of small kinetic energy are usually the most significant.[118] Thus, truncating the basis set to a finite number of plane waves can be a practical solution, which is defined by the kinetic cutoff energy.

$$E_{cut-off} = \frac{\hbar^2}{2m}|\mathbf{G}_{max}|^2 \tag{2.25}$$

The accuracy of the plane wave basis set can be systematically enhanced by increasing the cutoff energy.

2.4.2 Pseudopotentials and Projector Augmented Wave Methods

Although plane waves can sufficiently describe the delocalized electrons, they do not have the same performance for the wave functions with large curvature, e.g., the core region of an atom, and the wave function oscillates rapidly. Very high cut-off energy would be necessarily used, which increases the computational cost to solve this issue. Moreover, in contrast to the valence electrons, which are involved in most chemical bondings, the core electrons usually do not contribute to chemical bonds (especially for heavy elements). Therefore, the core electrons are described using pseudopotentials, in which by using plane waves, only valence electrons are modelled. The disadvantage of this approach is that the core electrons are not considered.

Another method in which all the electrons are considered is known as the "Projector Augmented Wave (PAW)" method.[134-135] In this approach, the all-electron wave function is described as a smooth pseudo wave function for the valence electrons and the local basis set expansion for the nuclei region (denoted as an augmented sphere) around each atom.

2.5 Thermodynamics of Catalytic Reactions

In order to find a connection between the catalytic reactions occurring in the real reaction conditions (high pressures and/or temperatures and longer times to reach steady-state conditions) and the atomic scales (lower temperature 0 K and femtosecond time-scales), constructing the kinetic model by applying some approximations are necessary. These corrections to the potential energy obtained from an electronic structure calculation (optimization of the structure) are provided by thermodynamics (vibrational frequency calculations). By computing the partition function, the thermodynamic properties, such as entropy (S), and Gibbs free energy (G), can be obtained. The total partition function q_{total} can be represented by the combination of translational, rotational, and vibrational modes related to thermal molecular motions:[136]

$$q_{total} = q_{translation} \times q_{rotation} \times q_{vibration} \tag{2.26}$$

where q_{total} is the total partition function that breaks down into the contributions of translational, rotational, and vibrational modes.

In this thesis, regarding the necessity of describing the behavior of gas molecules both in the gas phase and on the surface, which results in different partition functions, two different approaches; ideal gas approximation (for gas phase molecules) and harmonic approximation (for adsorbates on the surfaces) were employed.

2.5.1 Ideal Gas Assumption

To describe molecules in 3D space, degree of freedom (DOF) ($3N$ coordinates, where N refers to the number of atoms) is needed. It can be separated into translational, rotational, and vibrational components. The translational partition function can be calculated as:

$$q_{translation} = \left(\frac{2\pi m k_B T}{h^2}\right)^{\frac{3}{2}} V \tag{2.27}$$

with m being the mass, k_B the Boltzmann constant, h the Planck constant and V the volume.

Since the monoatomic gas molecules have no rotational mode of motion, the other gases have two or more, depending on whether they have linear or non-linear configurations. The diatomic and polyatomic gas molecules (homonuclear/heteronuclear) are treated differently in the calculations of rotational partition functions. The rotational partition function for a diatomic gas molecule can be written as:

$$q_{rotation} = \frac{8\pi^2 I k_B T}{\sigma h^2} \tag{2.28}$$

with $\sigma = 1$ the symmetry factor for the heteronuclear diatomic gas molecules and $\sigma = 2$ for homonuclear ones and I being the moment of inertia. The rotational partition function for the non-linear polyatomic gas species is defined as:

$$q_{rotation} = \left(\frac{1}{\sigma}\right)\left(\frac{8\pi^3 k_B T}{h^2}\right)^{\frac{3}{2}} I_x^{1/2} I_y^{1/2} I_z^{1/2} \tag{2.29}$$

The remaining degrees of freedom are related to the vibrational modes of motion, for which the vibrational partition function is represented as:

$$q_{vibration} = \prod_{i=1}^{3N_{atoms}-6} \left(\frac{1}{1-e^{-\beta h c v_i}}\right) \tag{2.30}$$

where $3N_{atoms} - 6$ represents the remaining degrees of freedom for non-linear and $3N_{atoms} - 5$ for linear polyatomic gas molecules with N atoms, c is the constant for the light's speed and v_i is the ith vibrational mode. As mentioned above, the thermodynamic properties can be obtained from the calculations of the partition functions. The ideal-gas enthalpy is one of those obtained properties, and it is shown in the equation below:

$$H(T) = E_{elec} + E_{ZPE} + \int_0^T C_P dT \tag{2.31}$$

where E_{elec} and E_{ZPE} are the electronic (ground state) energy and the zero-point energy (ZPE), respectively, and the integral over the heat capacity C_P (only as a function of temperature and not pressure for ideal gas).

The zero-point energy (ZPE) is expressed as:

$$E_{ZPE} = \frac{1}{2} \sum_{i}^{N} hc v_i \tag{2.32}$$

The entropy of ideal gas as a function of temperature and pressure can be calculated as:

$$S(T, P) = S(T, P^{\circ}) - k_B \ln \frac{P}{P^{\circ}} \tag{2.33}$$

which can break into rotational, translational (at a reference pressure P°), electronic and vibrational components:

$$S(T, P) = S^{\circ}_{translation} + S_{rotation} + S_{electronic} + S_{vibration} - k_B \ln \frac{P}{P^{\circ}} \tag{2.34}$$

where each of the components shown in equation **(2.33)** are calculated as below:

$$S^{\circ}_{translation} = k_B \left\{ \ln \left[\left(\frac{2\pi m k_B T}{h^2} \right)^{3/2} \frac{k_B T}{P^{\circ}} \right] + \frac{5}{2} \right\} \tag{2.35}$$

$$S_{rotation} = k_B \left[\ln \left(\frac{8\pi^2 I k_B T}{\sigma h^2} \right) + 1 \right] \quad , \text{if linear} \tag{2.36}$$

$$S_{rotation} = k_B \left\{ \ln \left[\frac{\sqrt{\pi I_x I_y I_z}}{\sigma} \left(\frac{8\pi^2 k_B T}{h^2} \right)^{3/2} \right] + \frac{3}{2} \right\} \quad , \text{if non-linear} \tag{2.37}$$

$$S_{vibration} = k_B \sum_{i}^{\text{vib DOF}} \left[\frac{\varepsilon_i}{k_B T (e^{\varepsilon_i / k_B T} - 1)} - \ln \left(1 - e^{-\varepsilon_i / k_B T} \right) \right] \tag{2.38}$$

$$S_{electronic} = k_B \ln \left[2 \times (\text{total spin}) + 1 \right] \tag{2.39}$$

As the consequence of obtaining enthalpy and entropy the ideal-gas Gibbs free energy can be calculated from their combination:

$$G(T, P) = H(T) - TS(T, P) \tag{2.40}$$

2.5.2 Harmonic Approximation

The translational and rotational modes for the strongly bounded adsorbates (e.g., CO, etc.) on catalytic surfaces are frustrated. Thus, the vibrational modes are the only possible degrees of freedom and are approximated as quantum harmonic oscillations. The properties, such as internal energy U and entropy $S(T)$, which are related through the Helmholtz free energy ($F = U - TS$), can be calculated consequently.

$$U(T) = E_{electronic} + E_{ZPE} + \sum_{i}^{harmonic\ DOF} \frac{\varepsilon_i}{e^{\varepsilon_i/k_BT} - 1} \tag{2.41}$$

$$S = k_B \sum_{i}^{harmonic\ DOF} \left[\frac{\varepsilon_i}{k_BT(e^{\varepsilon_i/k_BT} - 1)} - \ln\left(1 - e^{-\varepsilon_i/k_BT}\right) \right] \tag{2.42}$$

2.5.3 Energy Corrections for BEEF-vdW

In comparison between the experimental and DFT results (using RPBE and BEEF-vdW exchange-correlation functionals) in the studies related to CO and CO_2 reduction[137-139], large errors in gas-phase thermochemical reaction energies were observed. To solve this issue, a promising technique based on statistical sensitivity analysis to determine the origins of the errors and then apply systematic corrections has been applied.[137, 139] The outcome of such studies illustrated and quantified the poor performance of RPBE and BEEF-vdW in describing the gas phase molecules with OCO backbone (e.g., CO, HCOOH, CH_3COOH, and $HCOOCH_3$). Consequently, a correction on the order of ~0.5 eV was reported to be necessary to minimize the error in the calculated reaction energies.

3 Particle Size Effect in Coinage Metals

3.1 Introduction

Transition metal nanoparticles are widely used in heterogenous catalysis for a broad variety of reactions ranging from hydrogenation to emission control, with nanoparticle sizes typically ranging from 3–20 nm.[140-142] While smaller particles have a higher specific surface area per gram of catalyst, they are often unstable and tend to sinter to larger particles during application.[143-144] Interestingly, it has been reported that smaller sizes lead not only to larger catalytic surface areas and higher concentrations of various surface terminations, but could also exhibit different catalytic properties. Perhaps the most striking example is given by gold nano- particles that have been shown to be highly active for CO oxidation while gold is otherwise not active at all.[145-147] These strong deviations of smaller clusters and particles from bulk-like behavior are often denoted as 'quantum size effects' and are due to the vanishing of the d-band into more localized, atomic-like d-states.[61-62] The size effect has been investigated theoretically for gold[61, 148] and platinum[62] nanoparticles up to the size of 3.7 nm. The transition of the underlying electronic structure towards the bulk limit has been identified at around 2.5 nm at which point the adsorption energies of O and CO converge to the limit of extended surfaces accompanied by the formation of a d-band. Other studies of the effect of the particle size on adsorption energies included Pt[149-150] and Pd[151-152]. Apart from gold, copper and silver are highly interesting transition metals with applications in methanol synthesis,[74, 153-154] the water–gas-shift reaction[155] and selective oxidation[156-157]. Particle size effects have also been identified for copper experimentally (e.g., for methanol synthesis),[158] but theoretical studies exist only for smaller copper clusters (<1 nm).[159-167] Similarly, experimental data for Ag demonstrated a strong size dependency for ethylene epoxidation[168-169], but only small Ag clusters have been studied theoretically to date.[170]

3.2 Computational details

For all DFT calculations, the BEEF-vdW[126] functional as implemented in the VASP[135, 171-174] program package in version 5.4.1 using the projector-augmented wave (PAW) method with standard PAW-potentials for the metal atoms and soft PAW-potentials[135, 173] for oxygen was used. For all calculations, a Γ-centered k-point sampling and Gaussian smearing with a width of 0.1 eV was used. For the bulk lattice parameters (**Table 3.1**), a cut-off energy of 800 eV was used for the plane wave basis set and a 16×16×16 Monkhorst-Pack grid, but only to determine lattice constants. The gas phase atoms were calculated in their ground state spin state (doublet) with a vacuum of 15 Å, 14 Å and 13 Å in x, y, z direction respectively.

Table 3.1. BEEF-vdW optimized lattice parameter a_0 in Å and corresponding bulk chemical potential μ^{bulk} in eV relative to the gas phase atom. E_{bulk} in eV is the total energy of the bulk metal and $E_{atom-gas}$ in eV the energy of the corresponding gas phase atom in the doublet spin state.

Metal	a_0	μ^{bulk}	$E_{atom-gas}$	E_{bulk}
Cu	3.664	-3.02	2.38	-0.64
Ag	4.206	-2.21	2.76	0.55
Au	4.208	-2.70	2.45	-0.26

The oxygen adsorption energy was calculated on a 4×4×4 (111) slab in the hcp and fcc position corresponding to a coverage of 1/16 monolayer of oxygen. The 2 bottom layers of the slab were kept frozen. The oxygen adsorption energy was calculated relative to 0.5 O_2 in the gas phase. A 4×4×1 k-point grid and a 350 eV energy cut-off was used. The distance between periodic images in z-direction is 18 Å. To calculate the distance of the oxygen atom to the metal surface as employed in the fixed atom nanoparticle calculations, a frozen (111) surface slab is chosen and the oxygen atom was relaxed in the fcc position. The distance between the oxygen atom and the metal atom underneath the oxygen atom is given in **Table 3.2** for the hcp and fcc position respectively.

Table 3.2. Distance between the adsorbed oxygen atom and the metal atom directly underneath in Å.

Metal	fcc position	hcp position
Cu	5.430	3.290
Ag	6.190	3.775
Au	6.205	3.810

All structures were optimized until atomic forces were below 0.01 eV/Å. As surface reference, the fcc position close to the edge of a 3×3×4 (211) surface is chosen, because of the similarities in the coordination environment of the oxygen atom to the position used on the nanoparticles. For the (211) surface a 5×4×1 k-point grid was used. The used adsorption positions on the surfaces shown **Figure 3.1** for the example of Cu.
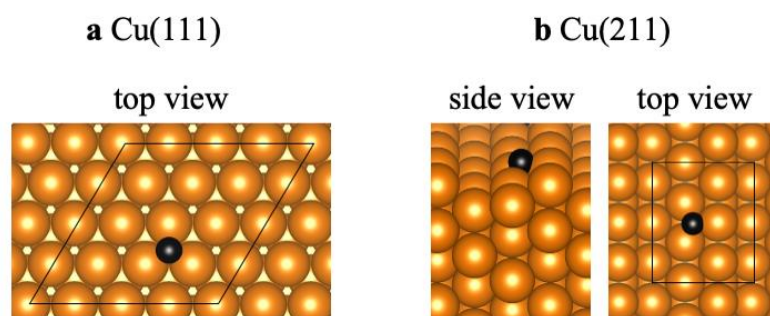

a Cu(111)   **b** Cu(211)

Figure 3.1. (a) Top view and unit cell of the used fcc hollow adsorption position on the (111) surface and (b) side view and top view of the used fcc hollow position on the (211) surface. Orange color represents Cu and black O.

The cuboctahedral nanoparticle structures are constructed using the cluster module of the atomic simulation environment (ASE) package[175] and the BEEF-vdW optimized bulk parameters as given in **Table 3.1**. A Γ-centered 1×1×1 k-point grid and 350 eV as energy cut-off was used. The periodic images of the clusters are separated by 28 Å. Cu structures between 13 and 923 atoms were optimized until atomic forces were below 0.01 eV/Å. Single point calculations were performed for Cu, Ag and Au structures containing 13 to 1415 atoms. To calculate the oxygen adsorption energy, the oxygen was placed on the (111) facet at the fcc position closest to the corner. The distance was chosen according to the one on the fixed (111) surface slab. The distances are given in **Table 3.2**. In the case of the nanocluster containing 13 atoms, the oxygen was positioned on the hcp position of the (111) facet using again the derived distance from the fixed surface slab.

For the investigation of the quantum size effect, for the example of Cu_{55} and Cu_{147}, additional metal atoms were added to the (100) facets, starting with the ones furthest away from the adsorbed oxygen to keep a low surface energy and to change the adsorption environment of oxygen as little as possible. In the case of Cu_{55}, as many atoms where added to form the truncated octahedral Cu_{79} and octahedral Cu_{85}. The additional metal atoms kept the bulk Cu-Cu distance and are in positions according to the fcc lattice structure. Smaller clusters were created by removing atoms resulting in the lowest surface energy configuration with the additional constrain that the atoms should be removed furthest away from the adsorbed oxygen. On these modified nanoclusters single point calculations only were performed. For comparison the octahedral Cu_{44} was calculated as well as a set with removed atoms starting from octahedral Cu_{146}.

3.3 Intrinsic Properties of the Particles

The effect of structure optimization for Cu for the mean Cu-Cu distance $\langle d_{Cu-Cu} \rangle$ and the chemical potential relative to the Cu bulk chemical potential is shown in **Figure 3.2** similar to Dietze et al.[176] Fitting the slope in Figure 1.2b with a linear function gives, $s_{Cu} = 2.46$ eV , which is smaller than the one derived by Dietze et al. ($s_{Cu}^{PBE-D3} = 3.76$ eV) for similar type of clusters. This is due to the use of a different functional (PBE-D3) as compared to the BEEF-vdW functional used in this work, which results in a different cohesive energy (-3.99 eV vs. -3.02 eV) likely also surface energies, which are directly related to the effective parameter s_{Cu}.
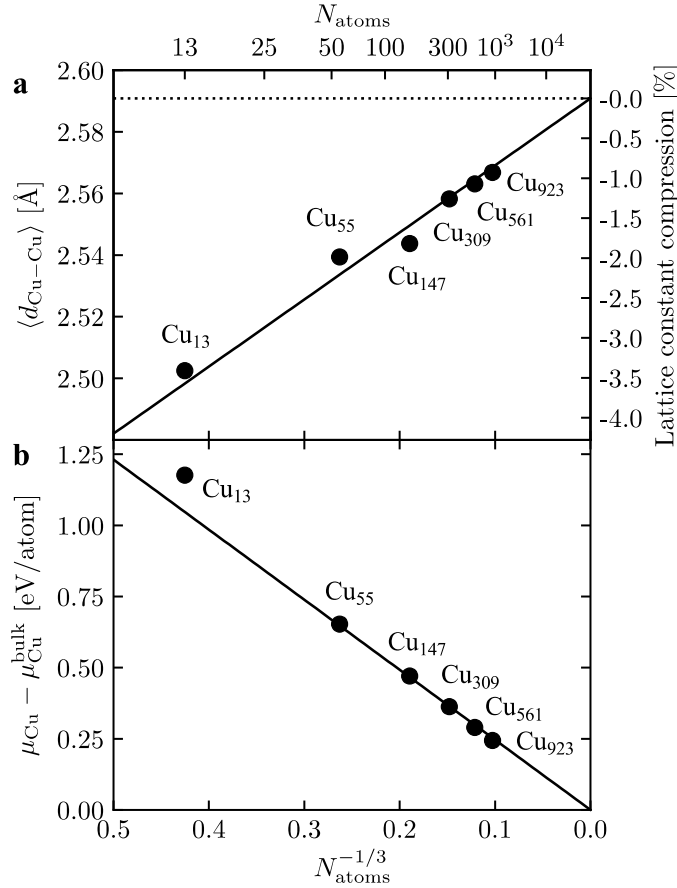
Figure 3.2. (a) Mean Cu-Cu distance $\langle d_{Cu-Cu} \rangle$ in Å of the relaxed nanoparticles and (b) chemical potential μ_{Cu} relative to the bulk chemical potential of bulk Cu, μ_{Cu}^{bulk}, both as function of the number of atoms to the power of -1/3, $N_{atoms}^{-1/3}$ (lower abscissa). The upper abscissa shows the corresponding number of atoms, N_{atoms}. Cu_{13} was excluded from the fit.

For visualization, the diameter of the various clusters was derived from spherical particles:

$$d = \left(\frac{6\, V_{atom} \cdot N_{atom}}{\pi} \right)^{1/3} \tag{3.1}$$

with V_{atom} derived from the mass and density of the corresponding metal as given in **Table 3.3**.

Table 3.3. Atom mass[177] m[178] in u, density[179] ρ in g/cm³ and corresponding atomic volume V_{atom} in Å³ of Cu, Ag and Au.

Metal	m [u]	ρ [g/cm³]	V_{atom} [Å³]
Cu	63.546	8.96	11.777
Ag	107.868	10.49	17.075
Au	196.966	19.30	16.947

In addition, the strain effect on the adsorption energy of oxygen was studied using a 4×4×4 Cu(111) slab with 4 layers of which the two bottom ones were frozen to the strained bulk lattice constant.

The oxygen was always placed on the fcc site. The results are shown in **Figure 3.3**. It can be seen that applying strain to the surface results in an increase in the oxygen adsorption energy for compression and decrease for lattice expansion.[180] The effect of surface compression for 2% is larger ($\Delta= 0.138$ eV) as the effect of expansion ($\Delta= 0.045$ eV), but in principle surface strain has only a small impact on the oxygen adsorption on the Cu (111) surface.
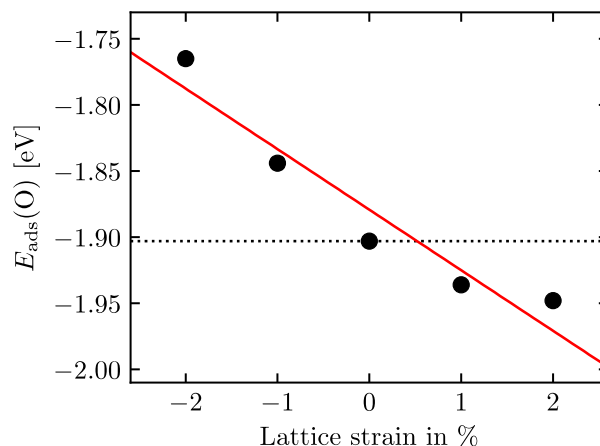

Figure 3.3. Effect of lattice strain on the oxygen adsorption energy. The dotted black line shows the adsorption energy with zero strain and the red line is the linear fit ($y = a \cdot x + b$) of the data with $a = -0.05$ eV/% and $b = -1.88$ eV.

3.4 Verification of the Model

Herein the effect of particle size for all three coinage metals, Cu, Ag and Au using density functional theory (DFT) calculations was investigated. As particles that are relevant for catalysis are typically larger than 1 nm for Cu[73], Ag[181] [77] and Au[145], the particle size effects including these sizes have been focused in this work. While particles are mostly supported in heterogeneous catalysis, free standing particles were studied. This has the advantage of decoupling particle size effects from perturbations of a particular support in addition to being computationally more feasible. It has been noted, therefore, that a direct comparison with experiments would need to account for metal-support interactions in addition to size effects. Herein the oxygen adsorption energy, that has been shown to be a key descriptor in the hydrogenation of CO_2 to methanol,[50] using cuboctahedral nanoparticles ranging from 13 to 1415 atoms (0.7–3.5 nm in diameter, see Figure 1.4) has been investigated. The clusters are chosen such that the size effect while maintaining the shape of the cluster and the adsorption site of the oxygen could be systematically investigated. The BEEF-vdW functional[126] was employed to calculate the oxygen adsorption energy on the fcc adsorption position closest to the corner of the (111) facet of the nanoparticles such that the adsorption site is the same for all particles with the exception of M_{13}, as shown in the insets in **Figure 3.4**. For Cu, the effect of geometry optimization is studied explicitly. For free standing metal Cu clusters ranging from 13 to 923 atoms, a linear relation between the mean Cu-Cu distance, the chemical potential which is approximated by the average energy per atom, and the number of atoms to the power of -1/3 (see **Figure 3.2**) is observed, similarly to what has been found for other metals[150, 170, 176, 182-188].
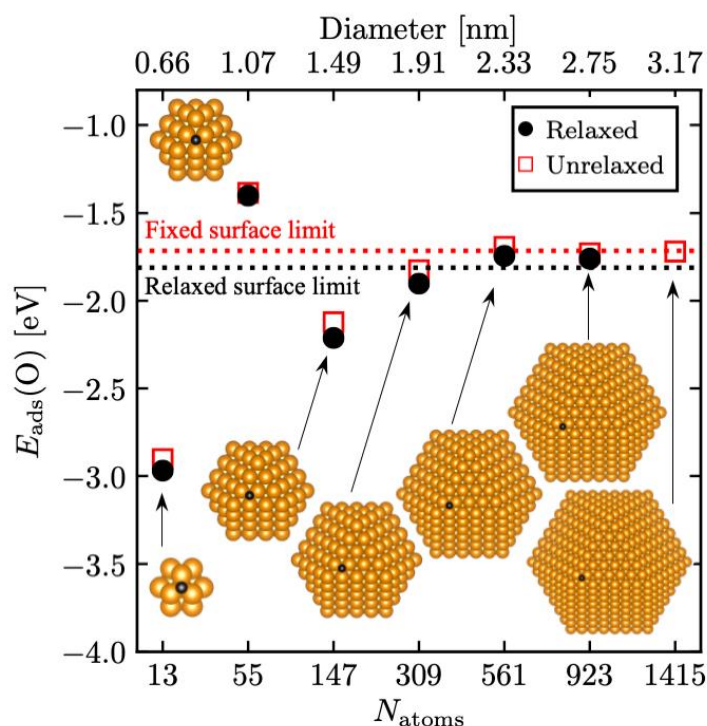
Figure 3.4. Adsorption energy of oxygen (relative to ½ gas phase O_2) on various fully optimized (black filled circles) and unrelaxed (red empty squares) Cu nanoparticles as a function of the number of atoms within the nanoparticles (N_{atoms}). The upper abscissa gives the corresponding nanoparticle diameter in nm derived from spherical particles (see section 3.3). The surface limit of the relaxed nanoparticles is given as black dotted line and the corresponding limit for the fixed geometry as red dotted line as calculated for adsorption on the fcc site of a Cu(211) slab with a coverage of 1/9. As insets, all Cu nanoparticles with adsorbed oxygen (black) are shown.

Figure 3.4 shows the adsorption energy of an oxygen atom on the Cu clusters with increasing size. The filled black circles show the results of the optimized structures. It can be seen that the adsorption energy converges to the limit of the Cu(211) surface for Cu_{309} and larger. As previously seen for Au_{55}, Cu_{55} shows a comparatively weak adsorption energy for oxygen. Comparing these results to single point calculations, using the Cu bulk lattice constant and the copper-oxygen distance obtained from Cu(111) surface calculations, it can be seen that all adsorption energies are shifted to higher values by approximately 0.1 eV. Keeping in mind that the accuracy of the BEEF-vdW functional with respect to adsorption energies on transition metal surfaces is around 0.2 eV,[127] the constant shift implies that the effect of strain is small and similar for all clusters, which can be also seen in **Figure 3.3** which plots the adsorption energy of oxygen on strained Cu(111) surfaces. This is in agreement with Kleis et al.[189] and Li et al.[62] [3], who found that trends in adsorption energies are similar for relaxed and unrelaxed clusters for Au and Pt. As was shown before by Mavrikakis et al.[180] and others[190-192], the overall effect of strain is usually linear for up to 3% deviation[193] from the lattice constant.

3.5 Particle Size Effect

Figure 3.5 compares the oxygen adsorption energy on unrelaxed Cu, Ag and Au nanoparticles, showing that for the 309-atomic cluster adsorption energies are converged to within about 0.2 eV. Interestingly, all three coinage metals follow the exact same trend, that is (1) strong adsorption on M_{13}, (2) weakest adsorption on M_{55}, (3) again stronger binding on M_{147} and (4) slow convergence from M_{309} and M_{561} towards the bulk limit. Overall, there is a systematic offset between the binding energies of a given cluster for the three metals, with binding energies generally decreasing from Cu over Ag to Au.
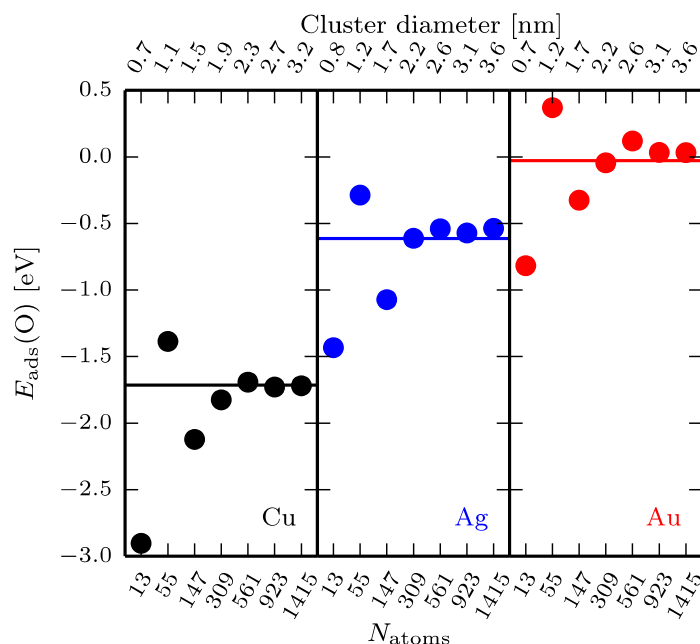

Figure 3.5. Adsorption energy of oxygen (relative to ½ gas phase O_2) on unrelaxed Cu, Ag and Au nanoparticles versus the number of atoms. The upper abscissa shows the corresponding nanoparticle diameter. The lines are the surface limit for adsorption on the fcc-site on the fixed 211-slab of the corresponding metal.

3.6 Quantum Size Effect (QSE)

Li et al.[82] argued that quantum size effects play a significant role for platinum clusters below 2 nm. This has been attributed to a change from a broad d-band to more discrete d-states, as the extent of orbital overlap of individual atoms decreases.

So far, in this study only geometric closed-shell cuboctahedral clusters[194] were included, which can be generated by sequentially adding coordination shells starting from a single atom, resulting in a monotonic increase of cluster sizes by increments of about 0.4–0.5 nm. In order to investigate the size effect for smaller variations in more detail, Cu nanoparticles ranging from 44 to 200 atoms as shown in Figure 1.6a were investigated. These clusters have been derived from cuboctahedral Cu_{55}, octahedral Cu_{146}, and cuboctahedral Cu_{147} by adding or removing atoms to or from the fcc lattice positions to create stable intermediate clusters. In particular, the atoms with lowest coordination number were removed first or atoms were added so that the added atom has the highest

possible coordination number. In case of different options for adding or removing atoms with the same coordination number, the site associated with the largest vertical distance from the top facet was chosen to minimize the direct influence on the oxygen adsorption site. For example, for cuboctahedral particles, atoms were first added to the fcc(100) sites towards the formation of octahedral particles. It can be seen that the oxygen adsorption energy varies strongly with the number of atoms and is oscillating for every 20–40 atoms. This can be explained by the so-called "electronic magic numbers" occurring for 58, 92 and 138 electrons, where closed-shell configurations are reached for spherical jellium clusters.[188] For the electronic configuration of coinage metals ($d^{10}s^1$), considering only the single s-electron per atom, particularly stable clusters are thus reached for cluster sizes N_{atoms} = 58, 92, and 138, e.g., cluster sizes with the number of atoms equal to the number of electrons in the closed-shell jellium configurations. Larsen et al.[195] have shown that for Cu, Ag and Au, clusters are particularly stable around these numbers and demonstrated that Au clusters show an increased oxygen adsorption energy. Here also a similar behavior in the oxygen adsorption energy for Cu has been observed, which shows a maximum close to these electronic magic numbers. Quantum size effects (QSEs) do hence play a key role for small Cu clusters where the oxygen adsorption energies change quite drastically with the addition or removal of a few copper atoms. Note also that the weak adsorption of Cu_{55} as well as the rather strong adsorption of Cu_{147} are close to the corresponding minimum and maximum. The drastic change in oxygen adsorption also means that for example Cu_{147} has a strong adsorption of about 2.1 eV, but that this is reduced by 0.4 eV when going to Cu_{140}. Atomically precise control of the particle size and size distribution would therefore be necessary if one wanted to adjust the oxygen binding energies within a narrow range. Interestingly, the behavior is very similar for Ag and Au, that follow the trends in oxygen chemisorption energies observed for copper in the 50–200 atoms range. As shown in **Figure 3.6b**, the stability of the metal clusters follows the usual increasing trend with cluster size, further highlighting the difficulties in precise cluster synthesis and stabilization in the reported range. Synthesis techniques such as wet impregnation or colloidal synthesis are presently not able to achieve such a high atom specificity[196] and further improvement is needed for the future design and preparation of nanoparticles.
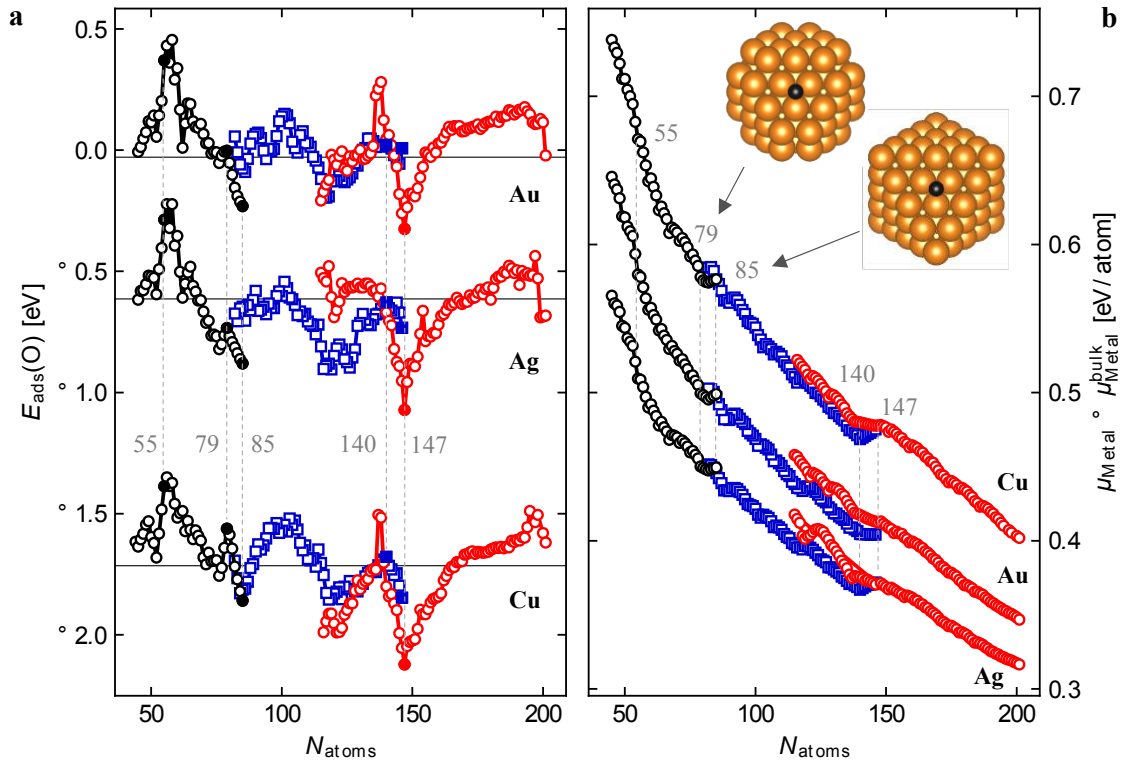
Figure 3.6. a: Oxygen adsorption energy (relative to ½ O_2 in the gas phase) on various Cu, Ag and Au fixed geometry nanoparticles as a function of particle size. **b:** Chemical potential μ_M relative to the bulk chemical potential of M, μ_{CM}^{bulk} for M = Cu, Ag, Au as function of the number of atoms. The filled black circles correspond to the M_{55} cuboctahedral cluster, the M_{79} truncated octahedral and the M_{85} octahedral cluster respectively. The filled red circle corresponds to the M_{147} cuboctahedral cluster. The filled blue squares correspond to the octahedral M_{146} and truncated octahedral M_{140} clusters. The open circles and open squares correspond to clusters that can be derived from the parent clusters described above by adding or removing atoms in bulk fcc-positions. The insets show the atomic structure of oxygen adsorption (black atom) on octahedral Cu_{85} and truncated octahedral Cu_{79}.

3.7 Conclusion of the Chapter

In summary, the effect of particle size on the adsorption energy of oxygen on the coinage metals Cu, Ag and Au has been investigated. It has been found that the effect of surface relaxation on oxygen adsorption is relatively small compared to the changes with particle size, thus allowing the use of less expensive single-point calculations and thus larger particles to capture the trends in adsorption energies. Interestingly, all three metals follow the exact same trend, where adsorption is strongest for M_{13}, weakest for M_{55} and approaches smoothly the bulk limit for M_{309}/M_{561}. In contrast, changes are quite drastic for smaller clusters for which an increase or decrease by one atom in a copper cluster changes the oxygen adsorption energy by as much as 0.1 eV. While it is interesting to note that the exact same trend for all three coinage metals was found, future work will show how this relates for other transition metals as well as how support interactions impact the oxygen adsorption energy. In the next chapter, the particle size effect on other transition metal particles will be discussed.

4 Particle Size Effect in other Transition Metals

4.1 Introduction

Supported nanoparticles (NPs) of late transition metals are used in wide range of catalytic reactions.[51, 57, 141, 197] Their reactivity is influenced by many factors, among them being e.g., the influence of the support as well as the shape and size of the nanoparticle.[198-199] Typically, one aims for metallic particles with sizes in the nanometer scale (with sizes between 3 to 20 nm), as they have a high surface area per gram of catalyst, and are thus normally more active than catalysts having large particle sizes.[143-144] For extremely small particles, typically less than 2 nm or even in the sub-nanometer regime, quantum size effects have also been reported to play an important role on the particle's reactivity. For example, Au NPs catalysts have been reported to have a high catalytic activity for low-temperature CO oxidation despite the fact that gold itself is a chemically inert element.[145-147] These quantum size effects are characterized by properties that are different than those for larger metal particles. A distanced difference is the fact that very small particles do not form a d-band typically for metals, but are instead characterized by well-defined d-states as typical for single atoms. This in turn has been observed to alter adsorption energies of adsorbates on the particles, typically such that they bind adsorbates stronger than the same catalyst surface of larger particles. At a specific particle size, the electronic structures of the metallic nanoparticles turn to their metallic counterpart, and likewise the adsorption energies converge to the surfaces of bulk structures.[75, 150-152, 195]

4.2 Computational details

All DFT calculations were carried out using BEEF-vdW[126] functional implemented in VASP[171-174] program package in version 5.4.1 and applying the projected-augmented wave (PAW) method. Standard PAW-potentials and soft PAW-potentials[135, 172] were used for the metal atoms and oxygen atom, respectively. A Γ-centered k-point and Gaussian smearing (width of 0.1 eV) were used. The optimization of lattice constants (lattice parameters gathered in **Table 4.1**) of the bulk structures of all transition metals (TMs) was done using 800 eV cut-off energy of the plane wave basis set and a 16x16x16 Monkhorst-Pack grid. The energy of oxygen adsorption was calculated on a hcp and fcc positions of four-layered p(3x3) unit cell of fcc(111) slab (1/9 ML coverage of oxygen) where all the atoms were kept frozen. A cut-off energy of 350 eV and a 4x4x1 k-point grid was used. The reported oxygen adsorption energies are relative to 0.5 O_2 in the gas phase. The fixed-geometries of metallic cuboctahedral nanoparticles were modelled with respect to the distance of atoms in their bulks and the distance of oxygen atom from the adsorption positions on the particles were obtained from the relaxation of oxygen atom on frozen slabs. The structures were

This chapter is based on the publication: Hakimioun, A.H., Kaźmierczak, K., Vandegehuchte, B., Curulla-Ferré, D., Plessow, P. N., Studt, F., *in preparation*.

38

constructed using the cluster module in the atomic simulation environment (ASE) python-based package[175]. The periodic images of the systems were distanced by 18 Å in z-direction.

Table 4.1. Lattice parameters a_0 in Å and corresponding chemical potential of bulk μ^{bulk} in eV relative to the gas phase atom. E_{atom} in eV is the energy of the corresponding single atom in the gas phase and E_{bulk} in eV is the total energy of the bulk metal.

Metal	a_0	μ^{bulk}	E_{atom}	E_{bulk}
Co	3.534	-4.91	0.639	-4.27
Rh	3.845	-5.69	1.44	-4.25
Ir	3.883	-8.00	2.18	-5.82
Ni	3.537	-4.38	1.85	-2.53
Pd	3.976	-3.207	1.25	-1.95
Pt	3.996	-5.12	1.99	-3.12
Cu	3.664	-3.01	2.37	-0.64
Ag	4.206	-2.21	2.76	0.55
Au	4.208	-2.70	2.45	-0.26

The calculated chemical potentials (μ_{Metal}) of the pure metallic nanoparticles (relative to the bulk chemical potential of metal, μ_{Metal}^{bulk}) as a function of the number of atoms to the power of -1/3 are depicted in **Figure A.1**. As can be seen, there are linear relations between the calculated chemical potentials, and the number of atoms. The growth of the size of the metallic NPs illustrates correlation with the stability of them, i.e., the bigger the size of the particle, the more stable it becomes. The difference in the stability of nanoparticles consist of different metals, is observable from the differences between the slopes of the fitted lines in each series.

4.3 Particle Size Effect for Groups IX and X Elements

In the previous work[200] particle size effects for coinage metals (Cu, Ag, and Au) using density functional theory (DFT) calculations of the adsorption energy of oxygen as a reactivity descriptor, were reported. Herein, that study is extended to groups IX (Co, Rh, Ir), and X (Ni, Pd, Pt). Earlier work on the size effect of copper NPs showed that one can utilize single point calculations without explicit geometry relaxations as these were yielding nearly identical results.[200-201] The same procedure of calculating single point energies as this allows to reduce the usage of computing resources tremendously, was applied (see **Chapter 3**). Cuboctahedral nanoparticles ranging from 13 to 923 atoms (see **Figure 4.1**) which represent nanoparticles of sizes of approximately 0.7 to 3 nm in diameter, depending on the transition metal, were used. Keeping the nanoparticle shape allows to study the size effect without changes of adsorption sites of oxygen. The oxygen chemisorption energy, which has been reported as a key descriptor in the hydrogenation of CO_2 to methanol, was studied.[50]
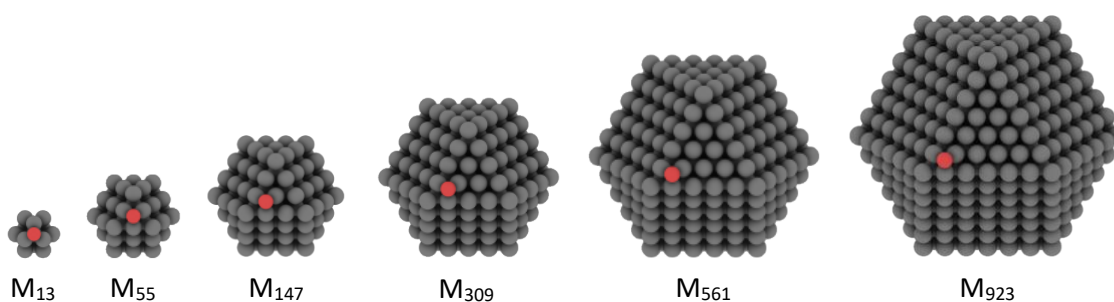
Figure 4.1. All metallic nanoparticles (M=Co, Rh, Ir, Ni, Pd, Pt, Cu, Ag and Au) studied, with adsorbed oxygen atom (in red) are shown. All particles have a cuboctahedral shape, the sizes ranging from 13 to 923 atoms (app. 0.7-3 nm).

In all the calculations the BEEF-vdW functional[126, 202] was applied in order to calculate the oxygen adsorption energy adsorbed on the fcc position of the (111) facet of the nanoparticles closest to the corner which was kept identical for all the metallic particles studied. For the M_{13} clusters, the hcp adsorption position of the (111) facet was used to model the adsorption. The results of the calculated oxygen adsorption energies of transition metals NPs of Co, Rh, Ir, Ni, Pd, and Pt as a function of their particle size are shown in **Figure 4.2**. The solid lines denote oxygen adsorption on the M(111) surface limit. Since Co and Ni NPs contain large spin, calculations were very demanding with respect to computational resources. Therefore, only particles up to 561 atoms (M_{561}), have been converged, as evident from **Figure 4.2**. However, both Co and Ni reach the surface limit rather early on and it is not expected that this will change again for larger particles.

For Co, Rh, and Ir it was observed that while the corresponding M_{13} NPs bind oxygen stronger by -3.71 eV, -3.27 eV, and -3.35 eV, respectively, already the M_{55} NPs reach the oxygen binding energies of the extended (111) surfaces. Interestingly, Rh_{147} and Ir_{147} bind oxygen a bit weaker by about -1.84 eV and -1.51 eV, respectively. A comparison of the NPs considered in this study with those of the coinage metals is depicted in **Figure A.2**.

Ni, Pd and Pt NPs also show an increased oxygen adsorption energy for the small M_{13} cluster, being -3.29 eV for Ni, -1.77 eV for Pd and -1.74 eV for Pt. Oxygen adsorptions on both Ni_{55} and Pd_{55} are close to the extended surface limit and do not change with increasing NP size. For Pt a similar trend is observed with the exception that Pt_{55} has a slightly increased oxygen binding energy compared to the extended surface limit (-1.24 eV), such that this is first reached at Pt_{147} (app. 1.67 nm). The results obtained for Pt NPs are largely in line with those reported earlier.[83]
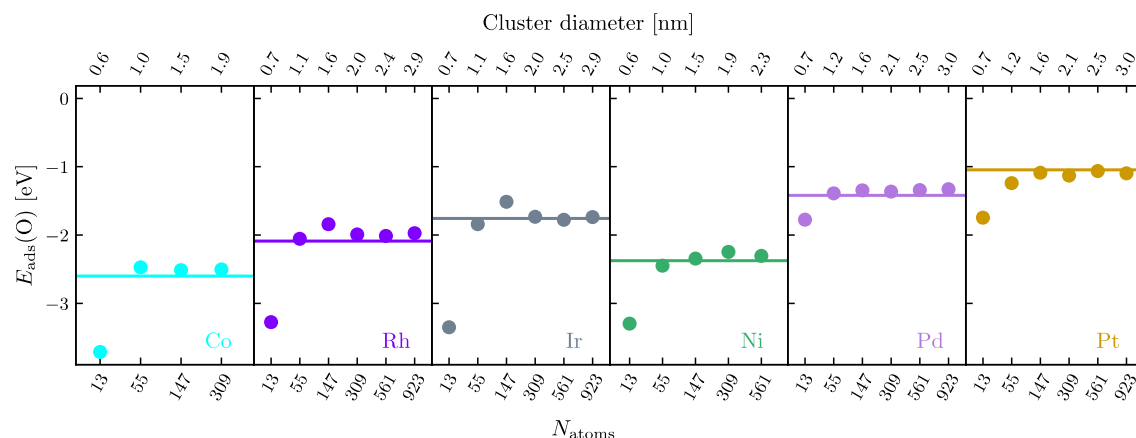
Figure 4.2. The calculated oxygen adsorption energies on the metallic NPs ($E_{ads}(O)$) against the number of atoms in NPs (N_{atoms})(lower abscissa) and the corresponding diameter of the particles (in nm). The cobalt (Co), rhodium (Rh), iridium (Ir), nickel (Ni), palladium (Pd) and platinum (Pt) metals are shown in cyan, violet and grey, green, purple, dark yellow colors circles. The horizontal lines correspond to the surface limits obtained from the oxygen adsorption energies calculated on fixed fcc(111) slabs of the corresponding metal. Adsorption energy of oxygen (relative to ½ gas phase O_2) on unrelaxed metallic nanoparticles versus the number of atoms. The upper abscissa shows the corresponding nanoparticle diameter.

4.4 Influence of Spin Polarization

The calculations of the nanoparticles consisting of Ni and Co were carried out, including spin polarization. However, to study the influence of spin polarization on the total energies of the metallic NPs and the calculated oxygen adsorption energy, a comparison between the spin-polarized and non-spin-polarized systems was performed. Among the $3d$, $4d$, and $5d$ transition metals (with unfilled localized d-states), only $3d$ metals are known to form magnetic solids. However, the studies on $4d$ metal clusters reported nonzero magnetic moments for Pd and Rh clusters in the gas phase.[203] The calculated magnetic moments (μ_B) (normalized to the number of atoms in their structures) of the spin-polarized cuboctahedral NPs are shown in **Figure 4.3**.
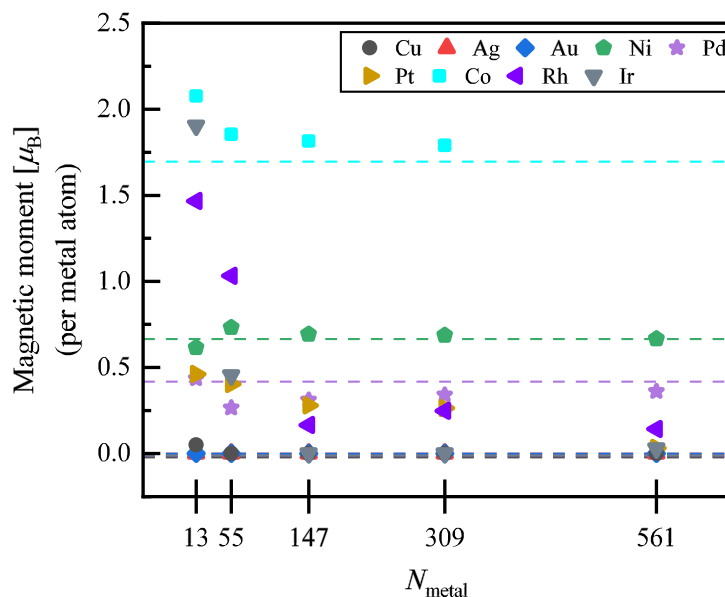
Figure 4.3. The calculated magnetic moments (μ_B) (per atoms) of the metals relative to the number of atoms in the particles as a function of the number of metal atoms in the nanoparticles. The copper (Cu), silver (Ag), gold (Au), nickel (Ni), palladium (Pd), platinum (Pt), cobalt (Co), rhodium (Rh), and iridium (Ir) metals are shown in black, red, blue, green, purple, dark yellow, cyan, violet, and grey colors shapes.

As can be observed from **Figure 4.3** the magnetic moment (μ_B) per atom of Rh_{13} is approximately three times higher than the Ni bulk. It contrasts with the fact that the bulk Rh is not ferromagnetic while the Ni bulk is ferromagnetic. The converging of the magnetic moments (μ_B), per atom of metals, at different particle sizes for each elements is also observable in **Figure 4.3**. The oscillatory variation of the magnetic moments of Pd clusters with respect to the changes in their sizes was reported before.[204] In addition to the magnetic moments (μ_B) calculations to study the size effect, a comparison between the oxygen adsorption energies calculated on both spin-polarized and non-spin-polarized systems was also performed. The results of the calculated oxygen adsorption energies in both spin-polarized and non-spin-polarized systems as a function of the size of NPs are illustrated in **Figure A.2**. The figure reveals the slight effect of spin-polarization on oxygen adsorption energy. The calculated values of the magnetic moments of the pure metallic NPs and the O-adsorbed NPs, gathered in **Table A.3,** shows the stabilizing effect of oxygen adsorption on different transition metals NPs.

4.5 Conclusion of the Chapter

In conclusion, the particle size effect of the transition metals of groups IX, and X of the periodic table of elements by means of oxygen adsorption energy were investigated. It has been shown that by using less expensive single-point calculations on the well-defined fixed-geometry structures of the nanoparticles, the trends in adsorption energies can be captured. Reaching the bulk limits are observed at different particle sizes by changing the metal. M_{13} clusters, in all the studied cases, show higher reactivity toward the oxygen. The spin-polarization indicated a margin influence on the oxygen adsorption energy, where it disappears by the growth of the size of the nanoparticles.

In the next chapter, the influence of support on the adsorption of oxygen atom on copper nanoparticles of different sizes and shapes will be discussed.

5 Metal-Support Interactions in Heterogeneous Catalysis

5.1 Introduction

Oxide supported transition metal particles constitute an important class of heterogeneous catalysts, being employed for reactions ranging from hydrogenation over oxidation to emission control.[205] The composition of such catalysts in terms of oxide and transition metal, greatly determines the interaction between metal particles and the support surface. This interaction additionally both depends on and dictates particle size and shape as well as the long term stability of the catalysts,[51, 72, 206-212] with typical sizes of the transition metal particles used in industry being in the nanometer range, mostly somewhere in between 3-20 nm.[76] Importantly, the activity and selectivity of a catalyst often crucially depends on the exact nature of the particle – oxide interaction[93, 213-216], that, if it is strong, is often denoted as strong metal support interaction (SMSI).[217-223] There are multiple ways being discussed via which the oxide support can alter the catalytic function of the particle. Indirectly, through changing the shape and thus faceting of the nanoparticle[72, 224] or through an electronic interaction between the support and the particle, changing the electronic structure and thus d-band of the metal.[207, 225-228] Or directly, when the reaction occurs at the metal-support interface with the reactants and intermediates binding to both the transition metal and oxide support.[92, 229] While these phenomena offer a plethora of possibilities to enhance the performance of catalysts,[216] it also makes the identification of active sites and reaction mechanisms, and thus a knowledge-based improvement, difficult to achieve.

Theoretical studies, mainly based on density functional theory (DFT) calculations, have found widespread application in the catalysis field as they are able to reveal the nature of the interaction of the transition metal with the reactants and intermediates. Furthermore, these calculations are now routinely used to compute transition state energies that can be directly linked to a catalysts activity and selectivity.[230-233] As the size of the real catalytic system is intractable for computations, these are typically performed using simple models of the active site. While small nanoparticles are subjected to quantum size effects[61-62, 234] traditional metal nanoparticles (NPs) with diameters larger than 3 nm are conveniently modeled using extended surfaces of the facets constituting the particle, thus greatly reducing the size of the system. These models do, however, not include support effects other than those on particle shape. To include also other support effects, more and more attempts is made for modelling of supported nanoparticles (NPs).[235-237] Due to the increasing computational demand with increasing particle size, these models typically consist of particles well below 3 nm, where they are subject to quantum size effects and might thus not be representative of the much larger catalytic system.

An elegant way to circumvent these limitations has been found in so-called nanowire or nanorod models of the transition metal supported on the oxide of interest.[92, 238-239] Such an approach ensures

that the model mimics the behavior of large particles and is able to simulate the influence of the support while being computationally feasible. The accuracy of these models in representing the true interaction of large particles with oxide surfaces and the metal-support interaction, however, has not been fundamentally addressed to date.

Herein, the influence of MgO support on copper, measured by changes in binding strength of an oxygen atom, to evaluate the impact of parameters such as particle size and shape, and most importantly the effect of the interface have been studied. Using supported copper NPs with diameters up to 2.6 nm, their performance with nanowire models has been compared and an assessment of how well they can serve as models for metal-support interfaces has been made.

5.2 Computational details

All periodic DFT calculations were carried out using the Vienna ab-initio simulation package (VASP)[171-174] in version 5.4.1 and the functionalities of Atomic Simulation Environment (ASE)[175] python library, employing the Bayesian error functional with van der Waals corrections (BEEF-vdW)[126] and the projector-augmented-wave (PAW)[135, 173] method with standard potentials for metal atoms, and soft PAW potentials for oxygen atoms. Γ-centered k-point sampling was used in all calculations. Copper nanoparticles were computed at the Γ-point. Copper nanowire model, a 2x1x1 k-point was employed. The plane-wave kinetic energy cutoff was set to 350 eV for the calculations of the oxygen adsorption energy on systems including Cu NPs and nanowire (NW). A 16x16x16 k-point sampling and a cut-off energy of 800 eV was used for the calculations of bulk Cu and MgO. All calculations used a Gaussian smearing with a width of 0.1 eV. The bulk lattice parameters were calculated to 3.664 Å and 4.262 Å for Cu and MgO, respectively, in good agreement with experimentally and theoretically reported values.[23, 240-243] During the optimization of the MgO supported Cu NPs and NW structures, the positions of Mg and O atoms were fixed (with respect to its lattice in the bulk), whereas the positions of all copper atoms were allowed to move until the forces of relaxed atoms converged to below 0.01 eV/Å. The distance between the copper nanoparticles and MgO support, which was used for the fixed-geometry models, was obtained from the relaxation of a 3-layered copper slab with a unit cell of (1x1) on a 2-layered MgO slab with the same unit cell size.

The adsorption of oxygen atom was modelled on p(4x4) Cu(111) slab, to determine the reference oxygen chemisorption energy and the distance of the atom from the Cu atoms in fcc and hcp positions (used further for the adsorption on the fixed-geometry nanoparticles). The O was allowed to fully relax, while the Cu was kept frozen. The oxygen adsorption energy was calculated as follows:

$$E_{Adsorption} = E_{Cu/MgO+O} - E_{Cu/MgO} - E_O \tag{5.1}$$

where $E_{Cu/MgO+O}$ stands for the total energy of oxygen atom adsorbed on MgO supported copper nanoparticle, $E_{Cu/MgO}$ for the total energy of MgO supported copper nanoparticle and E_O for the energy of an oxygen atom ($1/2\ E_{O_2}$).

5.2.1 Cohesive Energy

The stabilization effect of the magnesium oxide support on the copper nanoparticles is shown in **Figure 5.1**. A margin stabilizing effect of the support on the particles is observable. Cohesive energies were calculated using the following equation:

$$E_{Cohesive} = \frac{E_{Cu/MgO} - E_{MgO} - (N \times E_{Cu\,atom})}{N} \qquad (5.2)$$

where $E_{Cu/MgO}$ is the total energy of the MgO supported copper nanoparticle, E_{MgO} is the energy of MgO, N is the number of copper atoms in the system and $E_{Cu\,atom}$ stands for the energy of a single copper atom (2.37 eV).
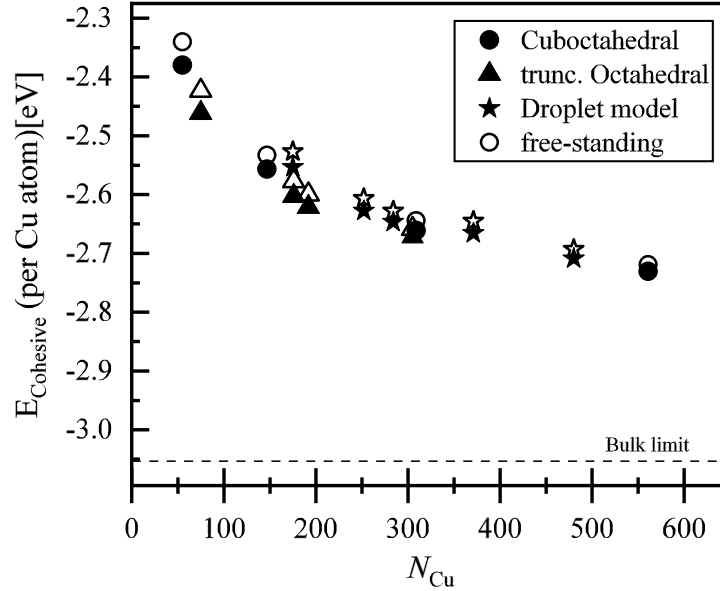

Figure 5.1 Calculated cohesive energies (per number of copper surface atoms facing the oxide support) both for MgO- supported and unsupported fixed-geometry copper nanoparticles versus the number of copper atoms in particles. The solid circle, triangle and star shapes represent cuboctahedral, truncated octahedral and droplet model geometries of the studied nanoparticles, respectively. The hollow shapes indicate the unsupported particles. The dashed-line in the figure represent the cohesive energy of copper bulk on MgO (the model of the structure is described above).

5.2.2 Optimum Distance between the Copper NPs on MgO

In order to find a sufficient distance between the periodic images of MgO-supported Cu NPs that guarantees negligible interaction, test calculations of oxygen chemisorption energies were performed on some of the Cu NPs, by varying the distance between the clusters. The results are shown in **Figure 5.2**.
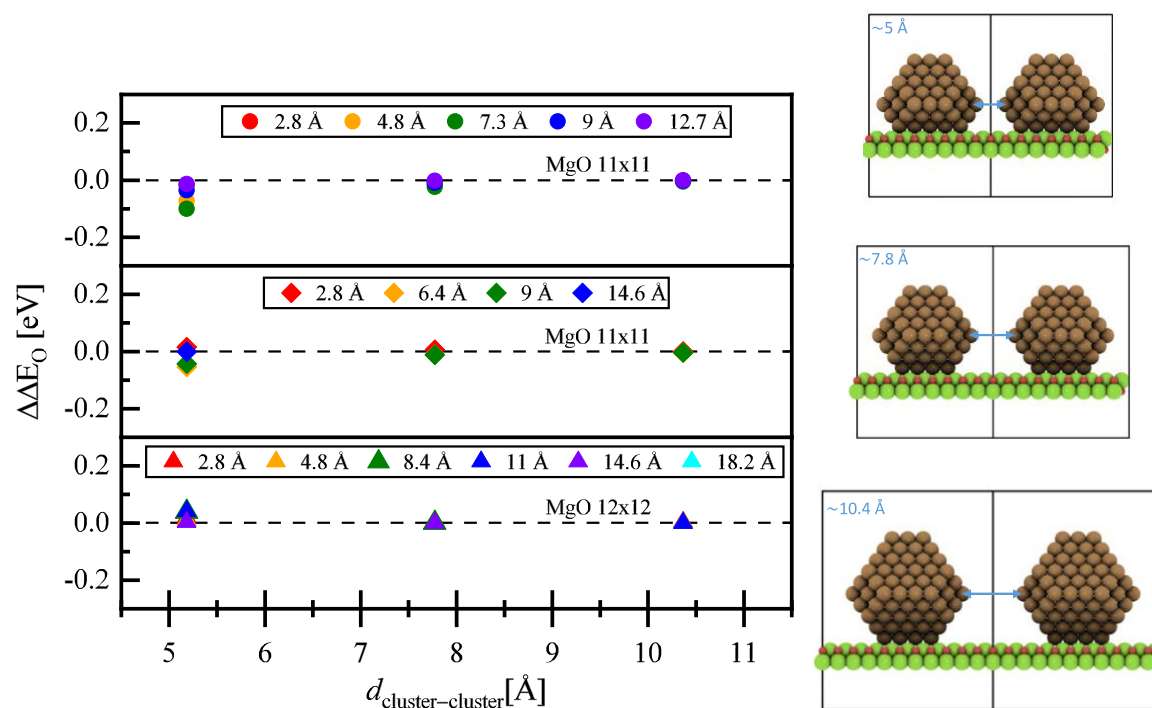
Figure 5.2. Left: The calculated oxygen adsorption energies difference on fixed-geometries of Cu_{176} (top figure), Cu_{192} (middle figure) and Cu_{305} (bottom figure) nanoparticles with respect to the distance between the copper nanoparticles and their periodic images. The values shown in legends represent the distance of oxygen atom, adsorbed on particles, from the oxide surface in angstrom. All the oxygen chemisorption energies are referenced to the values obtained from the calculate values of the same systems on longest distance between the particles. The dashed lines represent the referenced value calculated for oxygen adsorption energy on copper nanoparticles supported on the specified size of the magnesium oxide (number of magnesium atoms in *x*- and *y*-directions). Right: from top to bottom the repeated (in x-direction) structures of Cu_{176}, Cu_{192} and Cu_{305} supported on different sizes of MgO support. The distances between the particles with their periodic images are shown in figures (in blue color).

As the results show, a small distance of 5 Å is sufficient and for computational efficiency, this separation was chosen. The possible interactions between the periodic images of Cu/MgO structures orthogonal to the surface were avoided by applying a vacuum of ~16 Å in the z-direction.

The calculations of the oxygen chemisorption on different copper FCC-type surfaces (Cu(111), Cu(100), Cu(211), Cu(110) and Cu(321)) were performed using 4 layers of a Cu slab where 2 bottom layers were fixed to the lattice of copper in the bulk. The copper atoms in the unconstrained layers were relaxed until their forces were smaller than 0.01 eV/Å. For the Cu(111) slab: a unit cell of (3x3) with the k-point grid of 4x4x1; for the Cu(100) slab: a unit cell of (4x4) with the k-point grid of 3x3x1; for the Cu(211) slab: a unit cell of (3x3) with the k-point grid of 5x4x1; for the Cu(110) slab: a unit cell of (2x2) with the k-point grid of 4x6x1; and for the Cu(321) slab: a unit cell of (3x3) with the k-point grid of 3x4x1 were used. For all of the surfaces the cut-off energy of 450 eV was used. The oxygen adsorption energy was calculated relative to the energy of 1/2 O_2 in the gas phase. For visualizing the structures shown, iRASPA[244] and VESTA[245] software were used.

5.3 Models of Cu/MgO Catalysts

The choice of the copper magnesium oxide (Cu/MgO) system was motivated by related studies in methanol synthesis in which a route for methanol synthesis via CO hydrogenation, at milder conditions, by combining copper with basic oxide support (MgO), was proposed. It was shown that a synergy between the metal and oxide could result in the formation of active catalysts, such as Cu/MgO, for methanol production from CO/H_2 pathway. The mentioned synergy is assigned with a bifunctional mechanism provided at the Cu/MgO interface and could be interrupted by the presence of CO_2. Consequently, it was reported that the active Cu/MgO catalyst significantly impacted the increase of methanol productivity compared to the other supported catalysts.[229]

The fact that MgO is a non-reducible support, and that both MgO(100) and Cu(100) have square unit cells, greatly simplifies the Cu/MgO model construction. Herein, the investigations span from cluster sizes of 55 atoms (Cu_{55}) to particles consisting of 561 atoms (Cu_{561}) that are ~2.6 nm in diameter. These large particles require a tremendous computational capacity in DFT simulations, and therefore, approximate models using single-point energy calculations which greatly reduces this effort were applied. The oxygen binding energy was chosen as this is a simple enough descriptor that is sensitive to the underlying electronic structure of copper[200] and is often used to estimate the activity of copper as well as other transition metals for the hydrogenation of CO_2 to methanol.[50]

First the influence of magnesia on the intrinsic stability of the copper nanoparticles has been studied. The nanoparticles binding with their {100} facet to the MgO(100) shows stronger adhesion energies than the others which bind via {111} facets. This is caused by the difference in symmetries and alignments between the two interacting interfaces.

This can be observed in **Figure 5.3**, which shows the structure of both Cu(100) and MgO(100). For a perfect match at the interface, an interfacial Cu atom would always be placed exactly on top of an oxygen atom. However, due to the fact that the MgO-lattice constant is 16% larger (lattice-mismatch), this will be increasingly difficult for larger clusters.
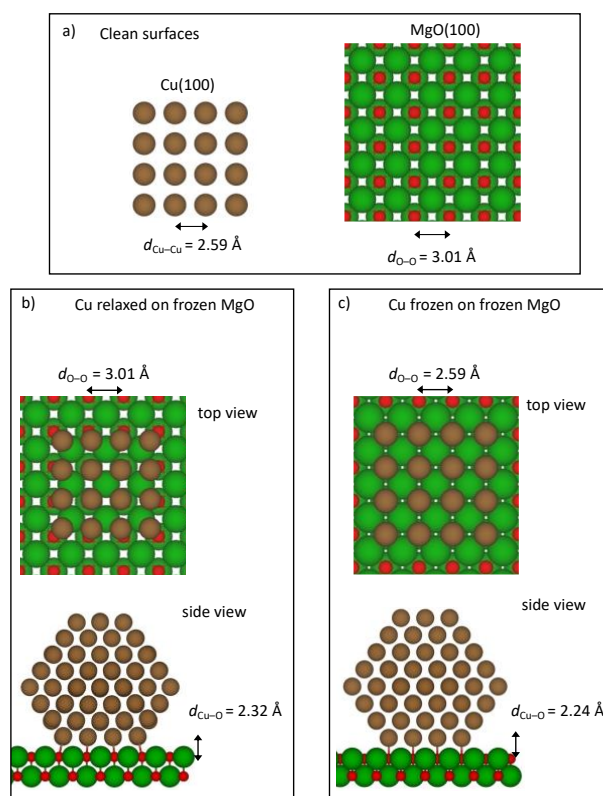
Figure 5.3. Illustration of the interface models studied in this work. (a) shows the clean surfaces and b-c) interfaces that arise when using (b) a relaxed Cu_{192} particle on MgO and (c) a Cu_{192} particle with atoms fixed in their bulk positions on top of MgO, where the atomic bulk positions have been scaled to match the lattice of Cu. For the top views, only one layer of Cu(100) is shown, in the case of interfaces, it is the interfacial layer.

Two types of models are considered in this work: First of all, Cu clusters are fully relaxed on a two-layer MgO(100)-slab, with the Mg and O atoms frozen in their bulk positions (see **Figure 5.3b**). Since this is computationally very demanding, a simplified model, where the Cu particles are also frozen with the atoms in their bulk positions, was furthermore explored. Due to the mentioned lattice mismatch, this simplified approach requires one lattice constant to be adjusted and it was chosen to scale the MgO lattice so that it matches that of Cu and keep Mg and O atoms again fixed in their (scaled) bulk positions, (see **Figure 5.3c**). The distance of the copper nanoparticles from the support was obtained from a calculation of a Cu(100) slab on MgO(100).

The adhesion energy per copper surface atom that interacts with the MgO support ($E_{adhesion}$) is calculated by subtracting the energy of the free-standing Cu NPs (E_{Cu}) and that of the MgO slab (E_{MgO}) from the energy of the supported Cu NPs ($E_{Cu/MgO}$) normalized through division by the number of copper atoms facing the oxide interface (n) (see equation **5.3**).

$$E_{adhesion} = \frac{E_{Cu/MgO} - E_{Cu} - E_{MgO}}{n} \qquad (5.3)$$

The results of the adhesion energies of Cu NPs are depicted in **Figure 5.4**. The solid circles and hollow shapes shown in **Figure 5.4**, represent the adhesion energies of the fixed-geometries (Cu bulk lattice constant, see **Figure 5.3c**) of copper nanoparticles adsorbing on lattice-matched MgO

(compressed by 16% to match the lattice of Cu in bulk) and relaxed Cu nanoparticles on MgO, respectively (see **Figure 5.3b**). The dashed line in **Figure 5.4** at -0.21 eV shows the adhesion energy of a relaxed 3-layered (7x7) unit cell of Cu(100) slab on a 2-layered (6x6) unit cell of MgO(100) slab (constrained to the MgO lattice in bulk) and the other dashed line, at -0.46 eV, shows the adhesion energy of a relaxed 3-layered (1x1) unit cell of Cu(100) slab adsorbed on a 2-layered (1x1) unit cell of MgO(100) slab (compressed lattice to match with the copper lattice in the bulk).

The relative binding energies decrease with increasing size of the nanoparticles because of larger lattice mismatch between the two interacting surfaces. Note that the fraction of interacting copper atoms decreases with particle size. Comparing the adhesion energies of the fully relaxed Cu_{55}, Cu_{75} and Cu_{192}, interacting with the oxide support via their {100} and {111} surfaces (hollow circles and triangles, respectively), it is obvious that the copper nanoparticles bind stronger to the MgO(100) support via their {100} surface. Cu_{75} binds stronger than other Cu nanoparticles, which we speculate is due to the fact that its small {100} facet can more easily adopt to match the support. Among the series of the calculated fixed-geometries, the droplet models bind weaker to magnesia whereas the truncated octahedral Cu NPs bind stronger to the MgO(100) support.
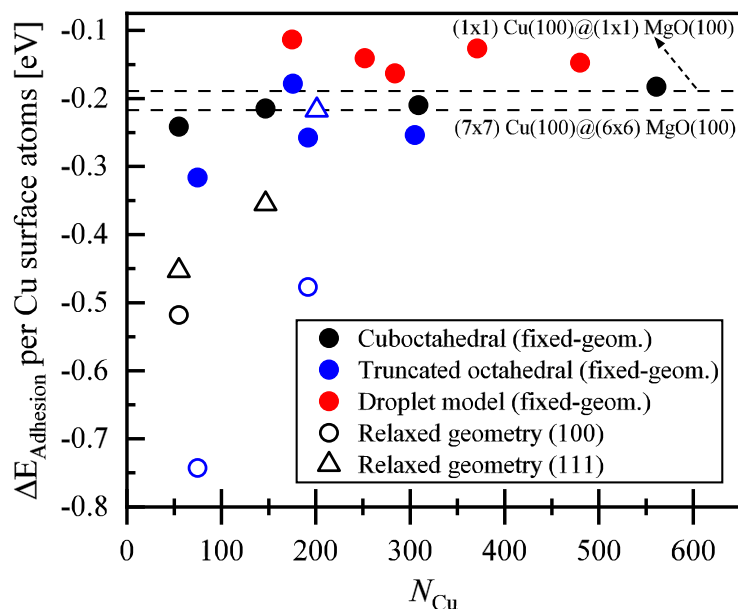

Figure 5.4. Adhesion energy of copper NPs supported by MgO per interacting surface copper atoms plotted against the total number of copper atoms in the nanoparticles. Solid and hollow shapes represent the fixed-geometries and fully relaxed Cu NPs on MgO, respectively. Circle shapes are used to show the adhesion energies of copper NPs on the MgO via their Cu(100) facets and the triangle shapes are used for the adhesion of Cu NPs on MgO surface via their Cu(111) facets. Black, blue and red colors were used to differentiate the series of cuboctahedral (Cu_{55}, Cu_{147}, Cu_{309}, and Cu_{561}), truncated octahedral (Cu_{75}, Cu_{176}, Cu_{192}, and Cu_{305}) and droplet-like (Cu_{175}, Cu_{252}, Cu_{284}, Cu_{371}, and Cu_{480}) nanoparticles, respectively.

Due to the strong interaction of truncated octahedral copper nanoparticles with MgO, they have been used to introduce and validate simplified methodology against full geometry optimized systems in this study. Therefore, the oxygen adsorption energy on various adsorption positions on Cu_{75} and Cu_{192} truncated octahedral particles was calculated. These results are shown in **Figure 5.5a**. The oxygen adsorption energies were calculated from full relaxation and single-point calculations of MgO supported copper nanoparticles and the adsorbate (oxygen atom). For single-point calculations, the distance of the adsorbate from the adsorption position of the copper nanoparticles was taken from the relaxation of oxygen atoms adsorbed on FCC and HCP positions

on a frozen four-layered Cu(111) slab, where all Cu atoms were fixed at their bulk positions. In all cases the oxygen atom was adsorbed on FCC(111) facets of the Cu NPs.

The differences of the oxygen adsorption energies between the supported and unsupported (free-standing) fixed-geometries of Cu_{75} and Cu_{192} nanoparticles, are plotted against the same differences from the fully relaxed systems in **Figure 5.5b**.
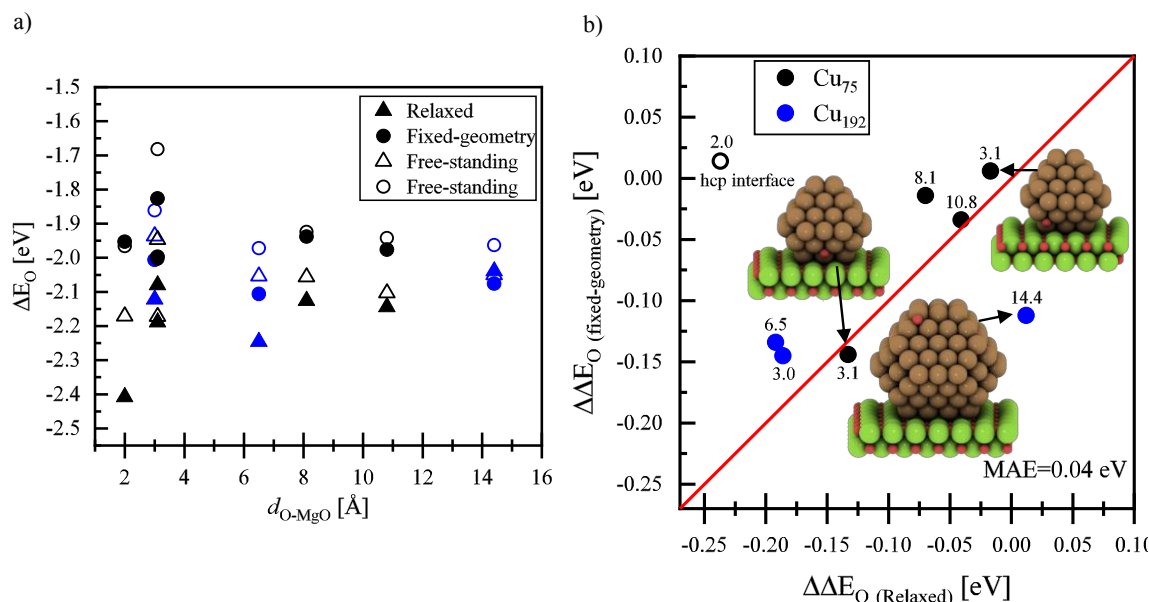

Figure 5.5. (a) Calculated adsorption energy of oxygen atom on Cu_{75} (black symbols) and Cu_{192} (blue symbols) both supported by magnesia (full symbols) and free-standing (hollow symbols) against the distance of adsorbate from the support. The triangle and circle points represent the optimized and fixed-geometry structures, respectively. (b) Parity plot of the difference of the oxygen adsorption energy between supported and free-standing fixed geometry of Cu_{75} and Cu_{192} against the same calculated energies of relaxed structures. The numbers on each of the points in the figure show the distance of the oxygen atom adsorbate from the magnesia support. The oxygen adsorption energy was calculated relative to the energy of $1/2O_2$ in the gas phase.

As can be seen from **Figure 5.5b**, the computationally cheaper procedure of calculating single points energies yields comparable results with those from the full relaxation, with a mean absolute error below 0.1 eV. The only exception is the oxygen adsorbed directly at the interface between the copper particle and the MgO support (hollow circle in **Figure 5.5b**). Since there is a significant interaction of oxygen with both the copper particle and the MgO surface, only fully relaxed structures yield reasonable results.

5.4 Support Effect

Having verified that the static model employing single point energy calculations is in fact able to reproduce the results and trends from the full geometry optimized models, the oxygen adsorption on various copper clusters and particle models on the MgO(100) surface has been calculated.

The extent of interaction of the MgO(100) surface with the various copper clusters and particles on the corresponding oxygen binding energy is shown in **Figure 5.6** for a series of truncated octahedral (Cu_{75}, Cu_{176}, Cu_{192} and Cu_{305}), cuboctahedral (Cu_{55}, Cu_{147}, Cu_{309} and Cu_{561}) and droplet models (Cu_{175}, Cu_{252}, Cu_{284}, Cu_{371} and Cu_{480}).
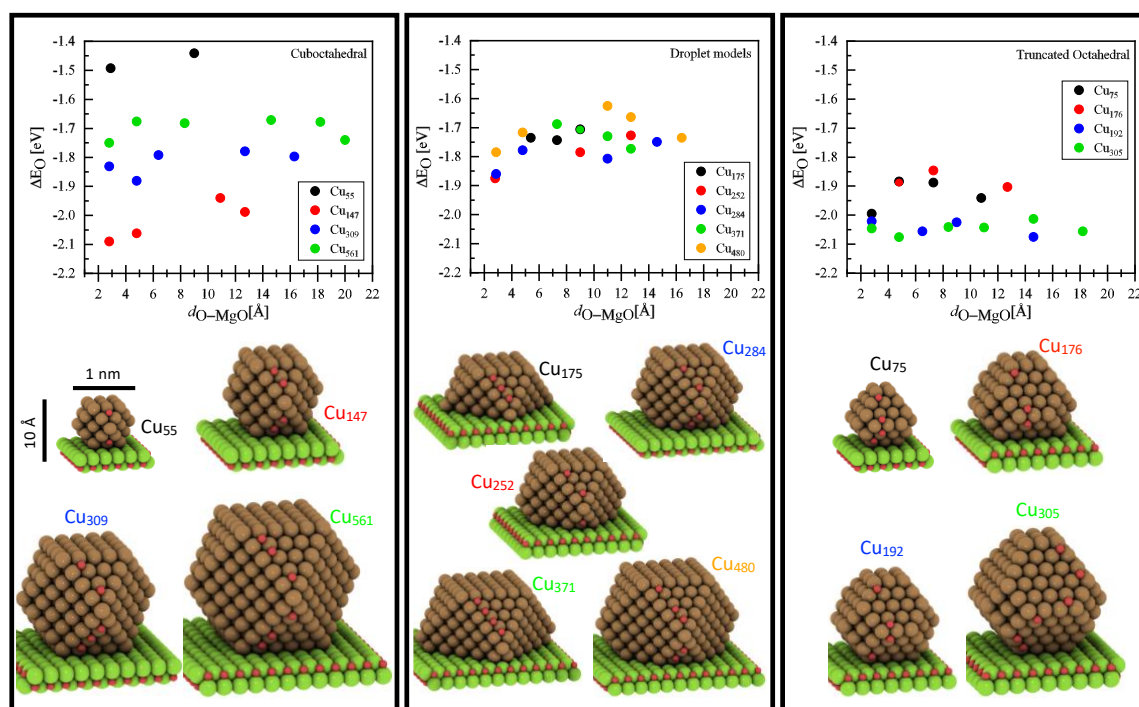
Figure 5.6. Oxygen adsorption energies calculated on fixed structures of the MgO supported copper NPs. The lattice constant of MgO, as described in the computational details section, is compressed to match with the lattice constant of copper in the bulk (Cu-Cu distance of ~ 2.59Å). From left to right: oxygen adsorption energy on cuboctahedral, droplet-like models and truncated octahedral copper nanoparticles against the distance of oxygen (adsorbate) from the oxide interface.

Here, the oxygen adsorption energy seems to slightly increase for some clusters by up to -0.17 eV. Importantly, the MgO support has only a small effect on the oxygen binding energy for all clusters and particles considered in this study, independent of its size and shape. The influence of the MgO support (see **Figure 5.7**), for some of the nanoparticles, is given as the difference between the oxygen chemisorption energy of the unsupported (free-standing) copper clusters and their MgO supported counterparts ($\Delta\Delta E_O$) as a function of the vertical distance of the chemisorbed oxygen from the MgO(100) plane. As can be seen, large variations only exist when comparing NPs of different sizes rather than for one size as a function of the metal-support interaction.
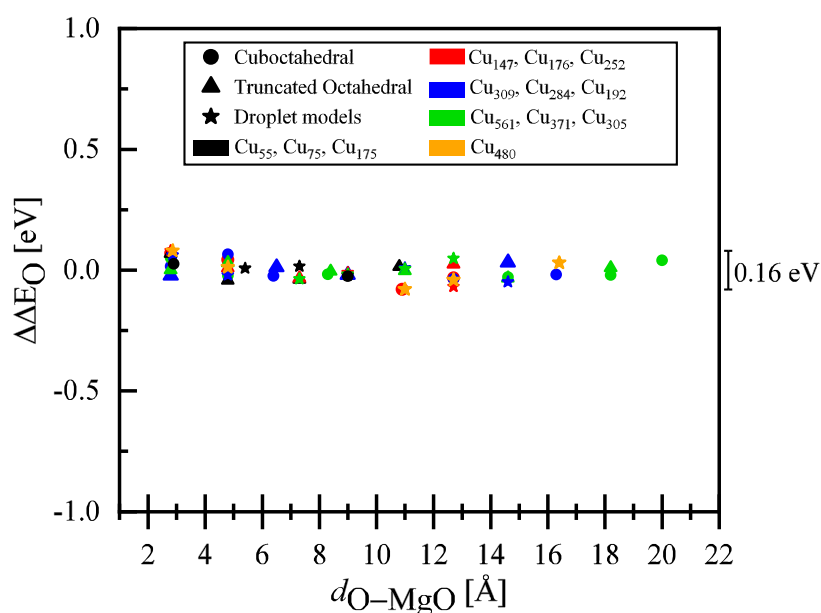
Figure 5.7. The oxygen chemisorption energy difference between the calculated values with DFT and the referenced values obtained from the zero slope fitted-line of the points of each series (average value), shown in **Figure 5.6**, with respect to the distance of the adsorbate (oxygen atom) from the support in angstrom. All the energies shown are in eV.

The impact of oxygen adsorption site distance from the support was evaluated, only considering positions on the copper clusters that are equivalent in terms of adsorption site geometry (see structures and adsorption sites in **Figure 5.6**). As can be seen from **Figure 5.7**, the influence of the MgO support on the oxygen binding energy is rather small (< 0.10 eV for most cases). There is a slight, albeit not very pronounced, effect at a close distance to the MgO(100) facet, where oxygen is binding to a position on the copper clusters less than about 4 Å from the MgO(100) plane.

5.5 Particle Size and Shape Effect

Due to the high computational cost of DFT calculations for large systems, simplified computational models of the particle support interface have been introduced recently. These are based on nanowires (NWs) of the transition metal interacting with the support.[238] By using nanowires, one can achieve a model with a smaller number of atoms per unit cell, that mimic the electronic structure of larger particles as a metallic character is obtained due to the periodic calculation. One therefore avoids the quantum size effects of sub-nanometer clusters that are typically used in computational studies. Here, a Cu nanowire model to simplify the calculations of the larger nanoparticles was employed. The MgO-supported copper nanowire used in this study is shown in **Figure 5.8**. Similar to the models of nanoparticles (shown in **Figure 5.6**) the structure of Cu NW as well as MgO were also fixed to the bulk lattice of copper in order to perform single-point calculations on the systems generated. The surface of the support is modelled by 2 layers of MgO(100) with a p(7x6) unit cell. The distance between two nanowires is approximately 5 Å, which has been verified as sufficient to suppress possible interactions between the periodic images (see **Figure 5.2**).
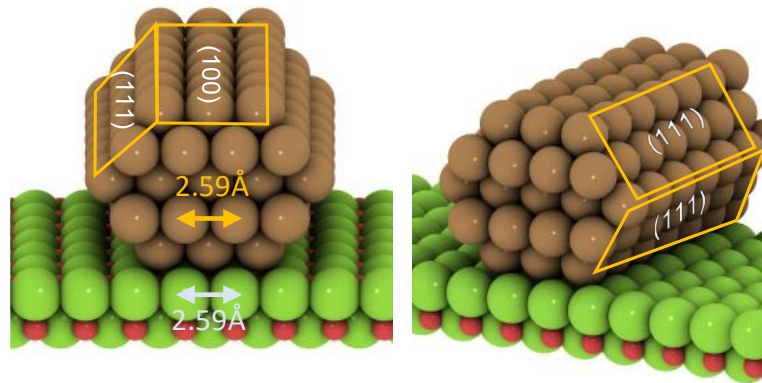
Figure 5.8. Left: Front view and right: perspective view of the Cu(7x5x5)/MgO nanowire model. The Cu(111) and Cu(100) planes are shown in the figures. Colors: Cu (brown), Mg (green), O (red).

Having shown that the support effect is visible only at the exact Cu-MgO interface, the influence of the adsorption site for all other adsorption positions on all considered models more generally using the concept of generalized coordination numbers (GCN), introduced by Sautet and co-workers[246] has been evaluated. GCNs are calculated by counting the nearest neighbors of the atoms on which adsorption takes place (n_j), weighing them by their own coordination numbers (cn(j)), and dividing by the maximum number of neighbors for given adsorption position (cn_{max}; see equation **5.4**).

$$\overline{CN}(i) = \sum_{j=1}^{n_i} cn(j)n_j/cn_{max} \tag{5.4}$$

This analysis reveals how the variation of the adsorption site on the cluster and particle models is affecting the oxygen adsorption strength. **Figure 5.9** shows the adsorption energies of oxygen (ΔE_O) for various positions on both, the MgO supported Cu_{192} and Cu(7x5x5) nanowire structures as a function of the GCN of the respective adsorption positions. As evident from **Figure 5.9**, ΔE_O is mostly a function of GCN, and the relation has a low mean absolute error (MAE).

a)

b)

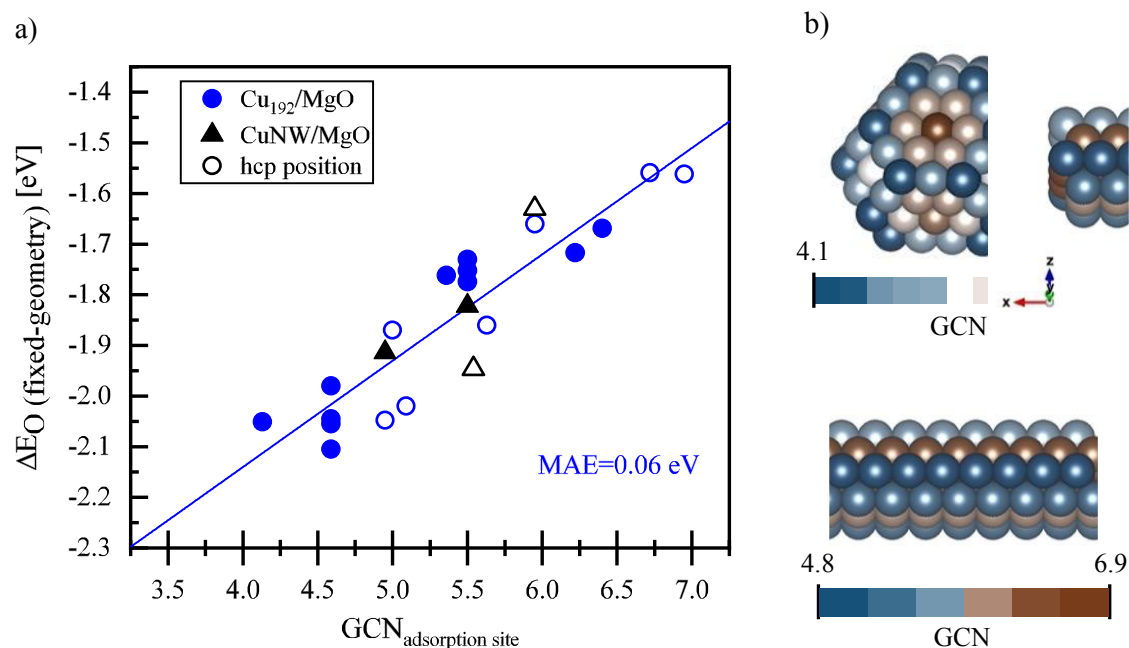**Figure 5.9. (a)** The oxygen adsorption energies calculated on different positions of MgO supported Cu_{192} (blue circles) and Cu nanowire (black triangles) fixed-geometries against the calculated values of GCN of the adsorbing positions. The blue fitted line shows the extrapolation of the oxygen adsorption values calculated for Cu_{192}/MgO. The hollow points in the figure represent the adsorption on HCP positions on the structures. **(b)** Above: The structure of truncated octahedral Cu_{192} nanoparticle. Below: The side view of the structure of Cu(7x5x5) nanowire. The atoms are colored with respect to their GCN values for which the range of the values are shown by the color scale bars below the structures. A general trend that of increasing adsorption strength which correlates with decreasing GCN is observable.

Next, the MgO supported NW model with calculations of Cu_{192}/MgO was compared (**Figure 5.10**). **Figure 5.10a** shows the positions of the adsorbed oxygen on the Cu_{192}/MgO and Cu(7x5x5) NW models with identical adsorption positions being shown in the same colors. For fully relaxed models, the oxide support was rotated by 45° so that the interface atoms of the copper nanowire face both magnesium and oxygen atoms of the support. The reason for this approach is that an unrotated nanowire, when fully relaxed visibly distorts and bends to form patches, where Cu fits to the underlying MgO lattice, which has not been considered a realistic model of a Cu NP in this work. For the models of fixed-geometry calculations, the MgO has not been rotated by 45°.
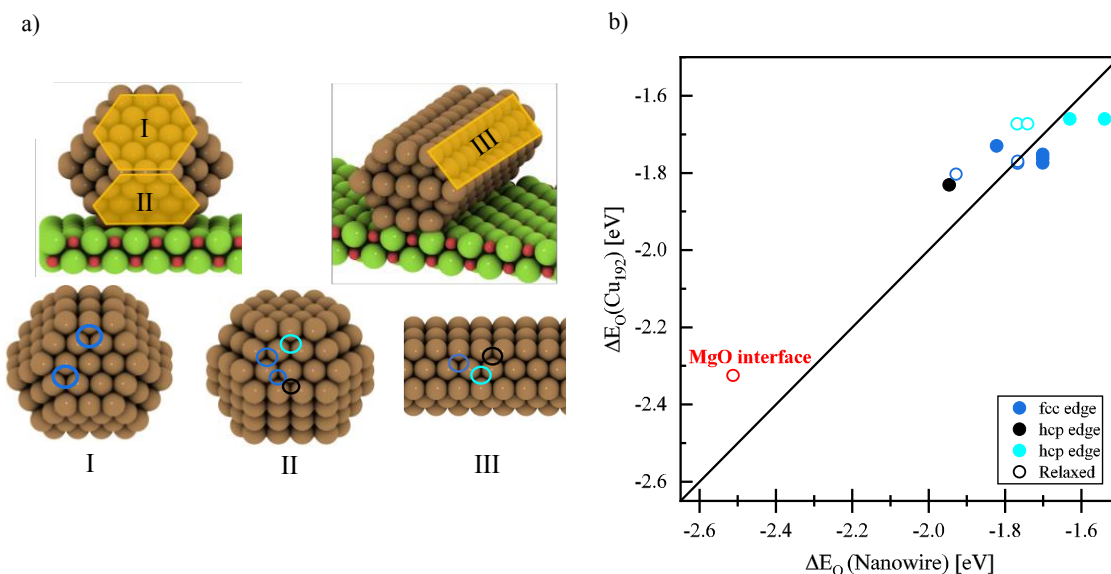
a)

b)

Figure 5.10. (a) Left: The structure of the 45° rotated Cu_{192} NP on MgO. Right: The 45° rotated Cu(7x5x5) NW on MgO. The numbered (I, II and III) structures are {111} facets on upper and lower planes of Cu_{192} and upper plane of CuNW, respectively. The blue, black and cyan highlighted circles depicted on the adsorption sites of the structures represent the intersecting FCC position between {111} and {100}, HCP position between {111} and {111} and HCP position between {111} and {100} facets, respectively. **(b)** Comparison of calculated oxygen adsorption energies on different adsorption sites between Cu_{192}/MgO and NW/MgO. The solid and hollow circles represent the energies of fixed-geometry structures and fully-relaxed ones, respectively.

As can be seen from **Figure 5.10**, there are only small differences between the supported Cu_{192} and NW models when identical adsorption sites are compared. As established earlier, the only marked influence of the support on oxygen adsorption energies is given for adsorption at the Cu/MgO interface (see **Figure 5.4**). This adsorption is about ~0.6 eV stronger, both for the interface of Cu_{192}/MgO and CuNW/MgO. It can be hence concluded that the NW model does reproduce the outcome of calculations with larger particles well.

5.6 Conclusion of the Chapter

The extent of metal-support interactions using DFT calculations have systematically been investigated. Choosing MgO as a non-reducible support and copper nanoparticles of various sizes, it was shown that the electronic effect of MgO on the reactivity of Cu, as measured by the oxygen adsorption energy, is rather small (about 0.1 eV), independent of particle size or shape. The only adsorption site where a strong influence of the support was present was the direct interface between MgO and the copper particles. When oxygen was binding to both MgO and Cu, an increased adsorption energy was obtained. A nanowire model, inspired by similar recent investigations in

literature, was further introduced and showed that it is indeed representative of supported copper nanoparticles.

A schematic comparison of the influence of the metal-support interaction, with those stemming from particle size effects and particle faceting is shown in **Figure 5.11**.
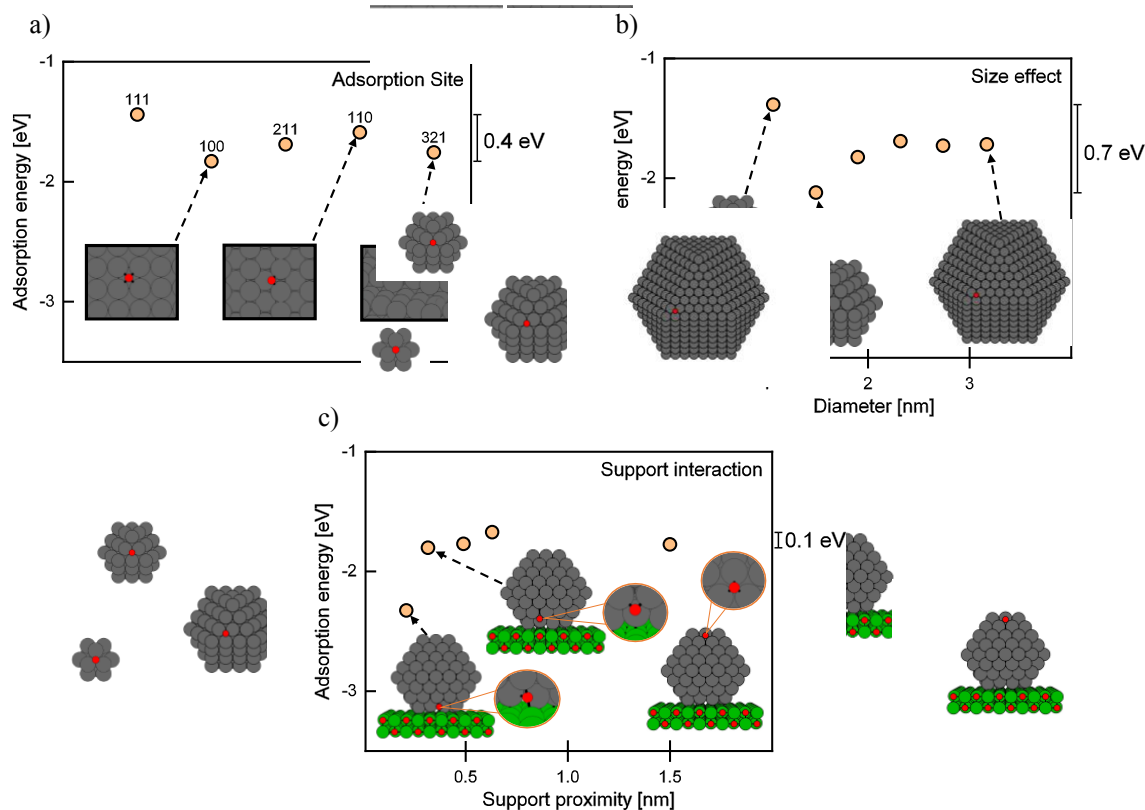

Figure 5.11. (a) Oxygen adsorption energy calculated on different copper surfaces ({111}, {100}, {211}, {110} and {321}) indicating the influence of different adsorption sites. (b) Oxygen chemisorption energy calculated on the free-standing fixed-geometries of cuboctahedral copper structures (from 13 to 1415 atoms) revealing the influence of the particle size on oxygen adsorption. (c) Oxygen adsorption energies calculated on a MgO supported Cu_{192} particle against the distance of the adsorbate from the oxide interface (in nm). The shaded areas as well as the scale bars (with values) on the right side of the plots represent the difference between the highest and lowest calculated oxygen adsorption energies. All energies are given in eV.

Differences in binding energies from various adsorption sites on different facets (from Cu(111), CN=9 to Cu(321), CN=6) are on the order 0.4 eV. The particle size effect is slightly larger (about 0.7 eV for particles > 1 nm) but vanishes at diameters above approximately 2.5 nm (oxygen binding energy difference of around 0.1 eV between the particles above 2 nm). The influence of the MgO support results in moderate deviations of about 0.1 eV. Note that remarkable differences for two cases have been observed, which are (1) extremely small clusters (Cu_{13} (~0.5 nm) binding oxygen stronger by ~1 eV) and (2) the exact interface of the MgO support with the copper particle (~0.5 eV) where oxygen binds to both MgO and Cu.

Using the Cu/MgO system, the impact of metal-support interactions for a non-reducible oxide on the reactivity of copper in addition to effects from particle size and surface faceting have been investigated. While the Cu/MgO system is interacting strongly (~ -0.5 eV per copper atom for Cu_{192}), the support is non reducible. The effect of reducible oxidic supports such as CeO_2 or ZnO might be substantially larger as electron donation could play a larger role.

6 Scaling Relations in Adsorption Energies

6.1 Introduction

The existence of various unique properties of transition metal nanoparticles (NPs), such as the presence of under-coordinated facets, quantum size effects (QSEs), and the higher ratios of surface-to-volume results in their great catalytic activity. The nanoparticles are used in various catalytic chemical reactions owing to their excellent catalytic properties.[57, 141-142] Many different factors, such as size[61-62, 158], shape[72, 247-249] and support[93, 250] can influence these properties.

The catalytic performance of the metals can be evaluated through the adsorption energies of various species (adsorbates) adsorbed on the available adsorption positions on their surfaces. Moreover, it is also important to study the activity of the catalysts to identify active catalysts or the active sites on different facets of the catalysts. Based on the Sabatier principle, the adsorption strength of an active catalyst should be neither too weak nor too strong. In the former case, the adsorbate desorbs easily from the catalyst surface, and in the latter case, the catalyst surface is poisoned by the adsorbate.[251] However, DFT-based computational methods, which can provide an accurate description of the catalytic systems of study, for the study cases of complex systems, such as nanoparticle catalysts, are quite demanding. Thus, combination of theoretical approaches, using cost-efficient and in the same time accurate models of the real systems, with the utilization of trends in catalytic reactions, which can predict the adsorption energies of the intermediates in a reaction or the behavior of different metals catalysts, are highly desirable and important. An example of such beneficial combinations, the computational models based on the fixed geometries of the NPs incorporated with the scaling relations method, can provide a promising solution to address the computational demands mentioned above. The fixed-geometry models of the transition metals NPs are reported to provide accurate results compared to the fully-optimized systems while consuming less computing resources.[61-62, 148, 252]

Owing to the recent developments and advances in computing systems and, in parallel, computational methods in theoretical chemistry and physics, the catalytic systems can be modeled, and the catalytic behavior of the catalysts can be accurately described. Therefore, it can direct the experiments to avoid possible errors and failures of the experimental studies.[45, 253-254] BrØnsted-Evans-Polanyi (BEP) relationship is one of the outcomes of the mentioned developments, in which one can find correlations between the accurately-predicted adsorption energies of different species (participants in the reactions) with the activation energies of the reactions.[255-256] The BEP relationships again shed light on the importance of investigating adsorption in catalysis. In addition, the binding energy of the intermediates adsorbed on specific site of the catalyst can be determined and scaled from/by the binding energy of the atom through which they are bound to the catalyst.[48, 257]

6.2 Computational details

All DFT calculations were done using Vienna ab Initio Simulation Package (VASP)[171-174] and the Atomic Simulation Environment (ASE)[175]. BEEF-vdW functional[126], which has provided reasonable description for the adsorption energies on transition metal surfaces, and projector-augmented wave (PAW) potentials for metal atoms and soft PAW for adsorbate atoms (C, O and H) were utilized.[135, 173] A Γ-centered k-point sampling and Gaussian smearing with the width of 0.1 eV for all the calculations were used. For the optimization of the bulk lattices, a kinetic cutoff energy of 800 eV for the plane wave basis set and a $16 \times 16 \times 16$ Mokhorst-Pack[258] grid was used. The optimized lattice parameters of 3.664 Å and 3.534 Å for Cu and Ni were obtained, respectively. The gas phase atoms and molecules were calculated in their ground state spin state (doublet) with a vacuum of 15 Å in all directions.

To model the fixed-geometry clusters and NPs with adsorbates and to determine the distance between the adsorbates and particles, the same setup, as discussed in **Chapter 3**, was employed. The adsorption positions of each of the adsorbates on the metal slabs and particles were followed as reported in ref[23].

6.3 Verification of the Fixed-Geometry Models

By using DFT methods, geometrical and electronic effects of the cuboctahedral copper and nickel particles, ranging from clusters of 13 atoms to particles with 1415 atoms (0.5 nm to 3.6 nm in diameter, see **Figure 6.1**), were investigated. Moreover, the scaling relations between the intermediates in the CO_2 hydrogenation to methanol reaction were studied. To reach the goals in this study, fixed geometries of the structures (atoms frozen to the lattice constants of the Cu and Ni bulks), similar to the method discussed in **Chapter 3**, were used. Thus, the adsorption energies calculated by doing cost-efficient single-point energy calculations were compared with the results of full relaxations of the structures.
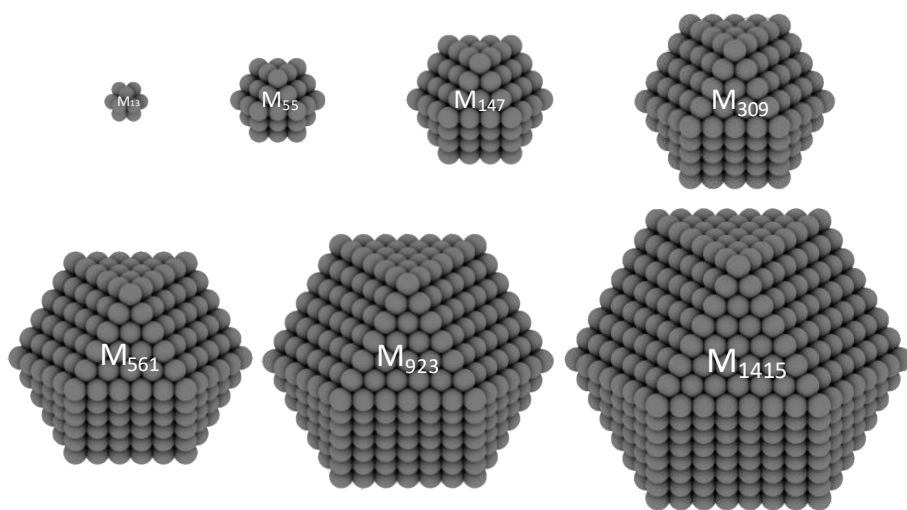

Figure 6.1. Schematic of the cuboctahedral geometries of the TM nanoparticles with number of atoms: 13, 55, 147, 309, 561, 923, 1415.

Adsorption energies of different intermediates in CO_2 and CO hydrogenation were calculated on the models using only static single-point energy calculations. Comparisons between the results of the adsorption energies obtained from the optimized structures and the fixed-geometry models (depicted in **Figure 6.2**) prove the accuracy of the proposed models ($\Delta\Delta E_{adsorbate}$ < ~0.2 eV). The deviations between the adsorption energies obtained from the optimization and the single-point calculations decrease as the sizes of the particles grow. The highest differences in adsorption energies are observable for the nanoclusters with 13 atoms which can be due to the quantum size effect (QSE). This phenomenon can be expected to influence the properties of copper particles up to 1.5-2 nm, in which the QSE disappears, and the particles behave as bulk.[200] In addition, trends in the adsorption energies of different intermediates adsorbed on Cu and Ni NPs with respect to their particle sizes are captured. Formate (HCOO) and hydrogen atom (H) bind stronger and weaker, respectively, to the copper NPs, compared to the other studied adsorbates. The un-reactivity of Cu_{55} towards the investigated adsorbates, which was observed before for oxygen adsorption (see **Chapters 3 and 4**), due to its closed-shell electronic configuration[200] is observable.

The corner positions of the fcc facet of the NPs were chosen to model the adsorptions. The adsorption sites (three-fold hollow fcc sites for O, H, CO, OH CH_3O, top position for HCOO, and three-fold hollow fcc and top positions for H_2COOH) were modelled according to the reported stable structures of adsorption of intermediates in CO_2 hydrogenation on copper fcc(111) facets.[23] The models were built based on the relaxation of each intermediate on the fixed geometry of metals' slabs. For M_{13} nanoclusters the three-fold hollow hcp site, which is the only available hollow position on its fcc facet, was used.
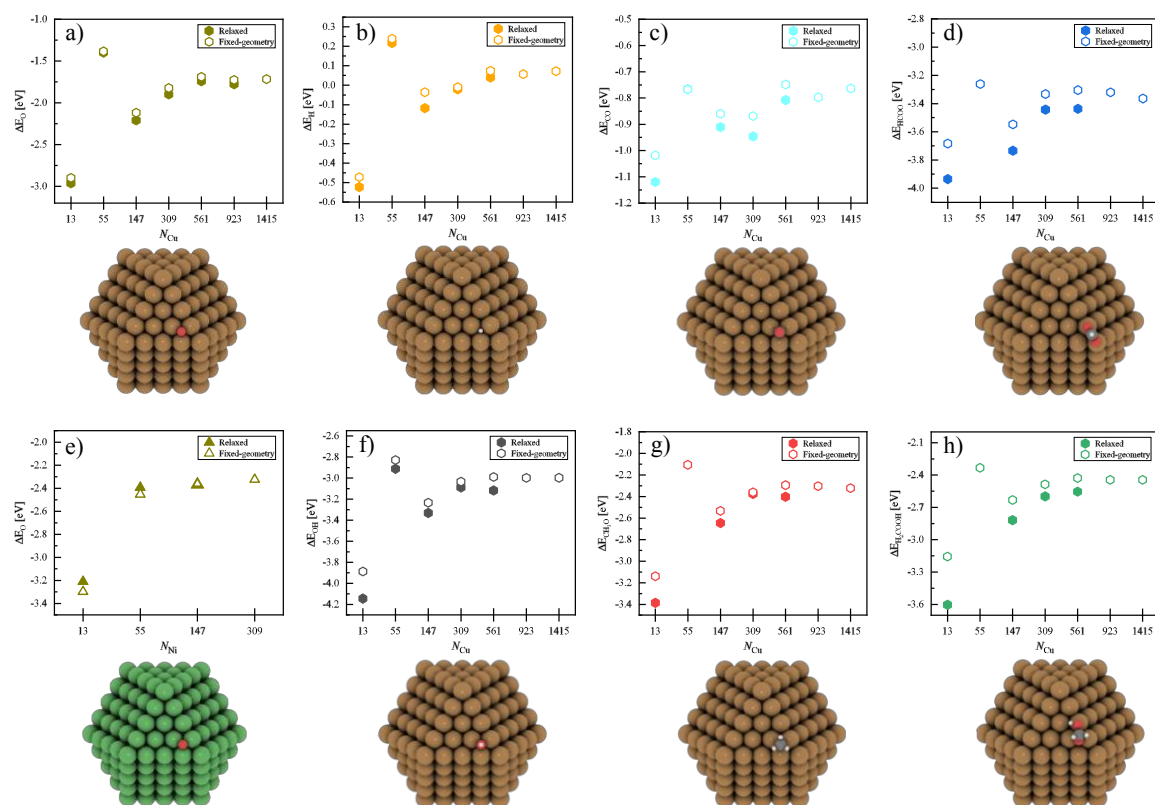
Figure 6.2. Calculated adsorption energies of different intermediates in CO_2 and CO hydrogenation reactions against the number of atoms in the nanoparticles. The solid and hollow hexagons and triangles represent the calculated adsorption energies from relaxed- and fixed-geometries, respectively. The adsorption energies of the adsorbates on nickel particles are depicted by triangles (e). The adsorption energies of (a) oxygen atom (dark yellow), (b) hydrogen atom (orange), (c) CO (cyan), (d) formate (HCOO) (blue), (e) oxygen atom adsorbed on nickel particles (dark yellow), (f) hydroxide (OH) (grey), methoxide (CH_3O) (red) and (h) H_2COOH (green). An example of the adsorption structure of each one of the adsorbates on M_{309} are shown below the related figures. The adsorption energies of each adsorbate are relative to their gas phase values.

The absence of the adsorption energies of relaxed CO, HCOO, CH_3O and H_2COOH adsorbed on the Cu_{55} (the solid points in **Figure 6.2 (c)**, **(d)**, **(g)** and **(h)**) is due to the transformation of the nanocluster's structure from cuboctahedral to icosahedral as the result of the geometry optimization of the system. This transformation, in which the six square fcc(100)-facets of the shell of the particles are converted to twelve triangular facets and results in 20 identical triangular-facet icosahedral particles, is reported to occur at lower activation barriers for coinage metals as well as Ni particles up to 309 atoms[259]. It is worth to noting that at the smaller sizes of the particles, the decahedral and icosahedral structures are reported to be more stable in some cases.[260-263] This can be in direct connection with the un-reactivity of the Cu55 due to its closed-shell electronic configuration combined with the electronic and geometrical stabilizing effect of the adsorbates. Interestingly, no rearrangement of the atoms was observed in M_{13} nanoclusters during the relaxation of the adsorption systems.

Having the model verified, the adsorption energies of the intermediates against the adsorption energy of the atom through which they bind to the NPs (oxygen and carbon) were calculated and illustrated in **Figure 6.3**. As can be seen from **Figure 6.3**, with imposed slopes of 0.5, all the calculated adsorption energies are scaled with the adsorption energy of the atom by which they bind

to the catalyst. In addition, the particle size effect on the adsorption energies of intermediates adsorbed on copper NPs is also observable. The intermediates bind weaker to Cu_{55} and stronger to Cu_{13} in each calculated series.
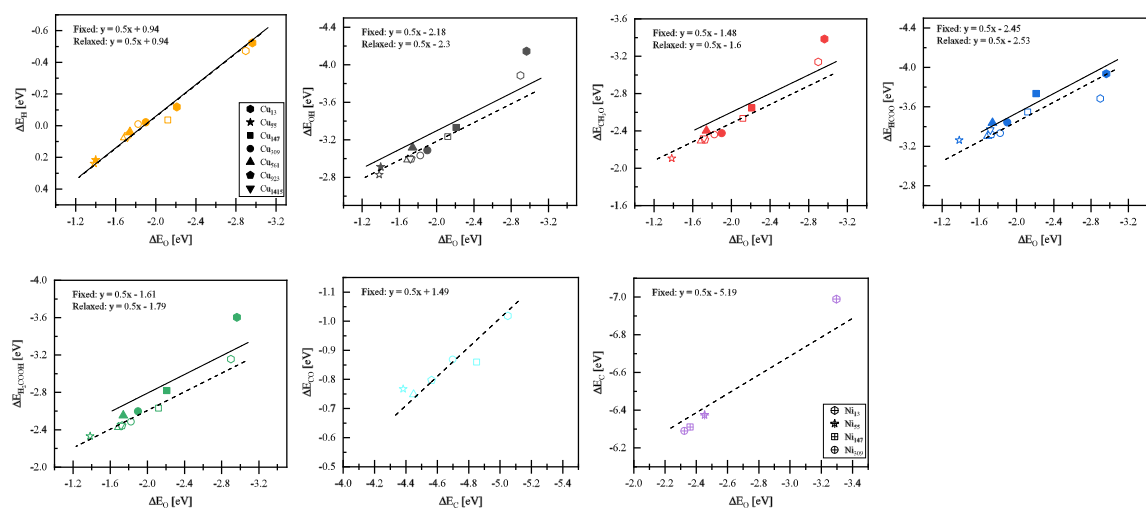
Figure 6.3. Calculated adsorption energies of different intermediates in CO_2 and CO hydrogenation reactions against adsorption energy of the atom through which they bind to the NPs. The solid shapes illustrate the adsorption energies obtained from the relaxation of the systems, and the hollow ones show the same energies obtained from the single-point energy calculations on fixed geometries.

6.4 Conclusion of the Chapter

Using DFT, it was shown that the cost-efficient static calculations on the fixed-geometry models of the copper and nickel particles could provide accurate results, compared to the results of relaxed systems, of the adsorption energies of different intermediates in CO and CO_2 hydrogenation reactions. The highest difference of ~0.2 eV between the adsorption energies calculated from the relaxation of the systems and applying single-point energy calculations on fixed-geometry systems proves the method's accuracy. The particle size effect of the studied particles on the adsorption energies of different intermediates was observed. The particle size effect for the particles up to 2 nm for copper and 1 nm for nickel were observed. The electronic effects caused by the adsorption of some of the intermediates on Cu_{55}, which resulted in the transformation of the structure from cuboctahedral to icosahedral, were noticed. The scaling relations between the adsorption energies of different intermediates in CO and CO_2 hydrogenation reactions combined with the particle size effect of the copper and nickel NPs were depicted.

7 Particle Size Effect in CO_2 Hydrogenation

7.1 Introduction

As mentioned, in detail, in **Chapter 1**, methanol is among the chemicals derived from the conversion of CO2, a potential substitute for fossil fuels. It is commonly used as a chemical feedstock in industry.[264] It is industrially produced from the hydrogenation of CO_2 (syngas) using $Cu/ZnO/Al_2O_3$ catalysts at the temperature of 240-260 °C and a pressure of 40-100 bar (see equation **1.1**).[28, 265-266]

CO_2, the main carbon source for the hydrogenation process, is provided by the water-gas shift (WGS) reaction (see equation **7.1**).
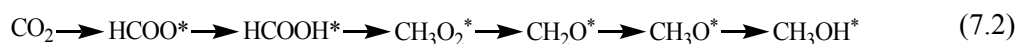
$$CO + H_2O \longrightarrow CO_2 + H_2 \qquad (7.1)$$

The stability of the catalyst benefits from the WGS reaction since the water produced during the methanol synthesis is consumed by the WGS reaction. However, if the feedstock consists of only CO_2 as the carbon source, CO_2 can be consumed by the reverse water-gas shift (RWGS) reaction (see equation **1.2**)

It is worthwhile to mention again that to increase the selectivity towards methanol production, and the mentioned competitive (RWGS) reaction must be avoided. In addition, the water produced (a by-product of RWGS reaction) could result in rapid degradation of the catalyst. Due to the mentioned factors, conventional methanol production is less challenging than pure CO_2 hydrogenation.[267]

For pure CO_2 hydrogenation, although new catalysts[268-271] were proposed to overcome the challenges, copper-based catalysts have still been mostly studied thanks to their high abundance, reactivity and low price[73, 267, 272]. To enhance the performance of the commercial $Cu/ZnO/Al_2O_3$ catalyst, which has been used for more than 50 years for methanol synthesis, some additives, such as ZrO_2, TiO_2, Ga_2O_3 and CeO_2, have been introduced.[273-276] However, these additives can behave simultaneously as both promoters and supports, resulting in the catalytic systems' complexity. To avoid this complexity and strong metal-support interaction (SMSI), the use of inert components, such as carbon support, is of great importance.[277-279]

Methanol and CO are both produced during the CO_2 hydrogenation reaction, and formate (HCOO*) and carboxylic species (COOH*) are known as the main intermediates in methanol synthesis using copper catalysts.[23, 34, 280] It has been reported that formate is the main intermediate in methanol synthesis.[38, 281-284] The proposed reaction sequence via formate intermediate to produce methanol from the hydrogenation of CO_2 is shown below:

$$CO_2 \longrightarrow HCOO^* \longrightarrow HCOOH^* \longrightarrow CH_3O_2{}^* \longrightarrow CH_2O^* \longrightarrow CH_3O^* \longrightarrow CH_3OH^* \qquad (7.2)$$

The influence of the size of the copper nanoparticles (NPs) and the catalytic characteristic of different facets are still under debate.[285-288] It has been reported that the reaction on different copper surfaces ({111},{100},{110} and {211}) is structure-sensitive, and the activity of the defect-rich stepped surface is higher than on flat surfaces.[23, 31, 37-38, 282, 289-293] MeOH and CO formation show two distinctly different activation energies, which suggests that the RWGS and methanol synthesis are occurring at different sites on the copper nanoparticles. To understand the particle size effect and which surface sites are more likely to be active for MeOH synthesis and CO formation, the theoretical fraction of different surface sites and the corresponding adsorption free energies for reaction intermediates by DFT calculation have been calculated..

Both CO$_2$ hydrogenation to methanol and the RWGS have been shown to be structure sensitive on copper surfaces.[23, 31, 38, 282] For methanol synthesis, it has been shown that sites with a low coordination number are more active, e.g., when comparing single crystal measurements on Cu(100) with those on Cu(110).[31, 36-38, 282] Surface defects, e.g., modeled by Cu(211) surfaces, have indeed been suggested as active sites for copper-based catalysts.[31] Likewise, the RWGS has also been shown to exhibit smaller barriers on more undercoordinated surfaces, although kinetic modeling indicates that this does not necessarily translate to higher reaction rates.[36, 38, 246, 280, 282] An interesting difference between methanol and CO formation is that the former is assumed to proceed via the formate intermediate. In contrast, CO formation occurs either via the carboxyl intermediate or through the direct splitting of CO$_2$.

7.2 Computational details

DFT calculations were carried out using the Vienna Ab Initio Simulation Package (VASP)[171-174] and the Atomic Simulation Environment (ASE)[175] employing the Bayesian error estimation functional with van der Waals corrections (BEEF-vdW)[126, 294] and the projector-augmented wave (PAW) potentials[135]. The BEEF-vdW functional was chosen due to the fact that it has a reasonable performance regarding adsorption energies on transition-metal surfaces.[127] Importantly, this functional has also been shown to successfully describe processes on copper surfaces relevant for the CO$_2$ hydrogenation to methanol.[139] The lattice constant of bulk copper was optimized to 3.664 Å using an energy cutoff of 800 eV and a 16x16x16 Monkhorst-Pack[258] k-point grid. The kinetic energy cut-off for all slab calculations was 450 eV. The surfaces were modelled by 4 layer supercells separated by 18 Å in the z-direction. The different sizes and corresponding k-point sampling used to calculate the various coverages are given in **Table A.4** in the appendix. In all calculations the bottom two layers were kept fixed at the bulk position while the top two layers and the adsorbate were allowed to relax until atomic forces had reached below 0.01 eV/Å. Adsorption energies were calculated relative to the corresponding gas-phase species (CO$_2$ and ½ H$_2$ in the case of formate and carboxyl). The correction of the well-known gas-phase errors for CO$_2$ (+0.41 eV) and H$_2$ (+0.09 eV) has been taken from the literature.[290] Using this correction an adsorption enthalpy of formate on Cu(100) of 84 – 91 kJ/mol (0.87 – 0.94 eV) for coverages 0.12 ML to 0.5 ML was obtained. This compares with 80 – 100 kJ/mol (0.83 – 1.03 eV) reported for measurements on Cu(100) single crystal surfaces.[295] Zero-point energy (ZPE) and entropic contributions were taken from calculations reported in the literature using Cu(211) in conjunction with the BEEF-vdW

functional[290] and are listed in **Table A.6** together with the total energies of all systems reported in **Table A.5**.

Based on the computed electronic energies, reaction energies and free energies were calculated at 503 K and 1 bar reference pressure using the results of published calculations.[290] Based on the data on *HCOO/Cu(211) in the supporting information of ref[290], the following energy differences for the formation of *CHOO/Cu(211) from CO_2(g) and H_2(g): Correction to DFT-energies to improve gas-phase energetics (-0.455 eV), ZPVE contribution (0.169 eV) and finally the Gibbs free energy contribution, including ZPVE (1.238 eV) were obtained. Based on these contributions, corrected energies and Gibbs free energies for the formation of formate were obtained for all facets by adding -0.286 eV (E) and -0.783 eV (G) to the electronic reaction energies.

The calculations on graphene bulk were carried out using the same setup as for copper bulk, which resulted in the optimized lattice constant of 2.465 Å and C-C distance of 1.42 Å, which were in a good agreement with the literature.[296-297] For the calculations of copper on graphene systems, BEEF-vdW functional and the projector-augmented wave (PAW) potentials for metal atoms and soft PAW for carbon atoms, a kinetic cutoff energy of 350 eV for plane wave basis set, a Γ-centered k-point sampling were used. Positions of all atoms were allowed to move during the relaxation until the forces of relaxed atoms converged bellow 0.01 eV/Å. A sufficient 14 Å of vacuum was applied to prevent interactions between the periodic images of structures. The system including fixed-geometries of Cu NP on defected-graphene, was modelled by removing a row of C atoms from the pristine graphene and functionalized it (where the bonds were cleaved) by adding O, OH and H to the carbon atoms on the defect. An optimum distance of 3 Å between the Cu NP and graphene with defect was obtained from a periodic calculation on a system containing 3 layers of Cu(111) on top of one layer of graphene (1x1) unit cell. In all the calculations, Cu NPs were placed on top of graphene sheet via their {111} facet.

7.3 Graphene Support

The reason for choosing graphene support in this study by our experimental collaborators (the university of Utrecht) was its expected weak interaction with metal particles larger than 2 nm.[298] Thus, it allows studying a series of size-controlled Cu nanoparticles supported on such inert material to study the intrinsic influence of Cu particle size.

Therefore, some theoretical investigations were done to confirm the absence of any effective influence of carbon support on the properties of copper NPs, which could have an impact on the catalytic properties of the catalyst and its performance during CO$_2$ hydrogenation. To capture the influence of the support on Cu NPs, oxygen adsorption energy on corner fcc positions of the {111} facet of NPs with different distances from the support, was calculated. This study used a graphene sheet as the carbon support material and cuboctahedral copper NPs with 147 and 309 atoms to model the systems. The structures of Cu$_{309}$/C with oxygen adsorbed on different particle positions are depicted in **Figure 7.1**.

$d_{O–C}$ = 5.3 Å $d_{O–C}$ = 9.5 Å $d_{O–C}$ = 13.1 Å

$d_{O–C}$ = 17.4 Å $d_{O–C}$ = 20.9 Å
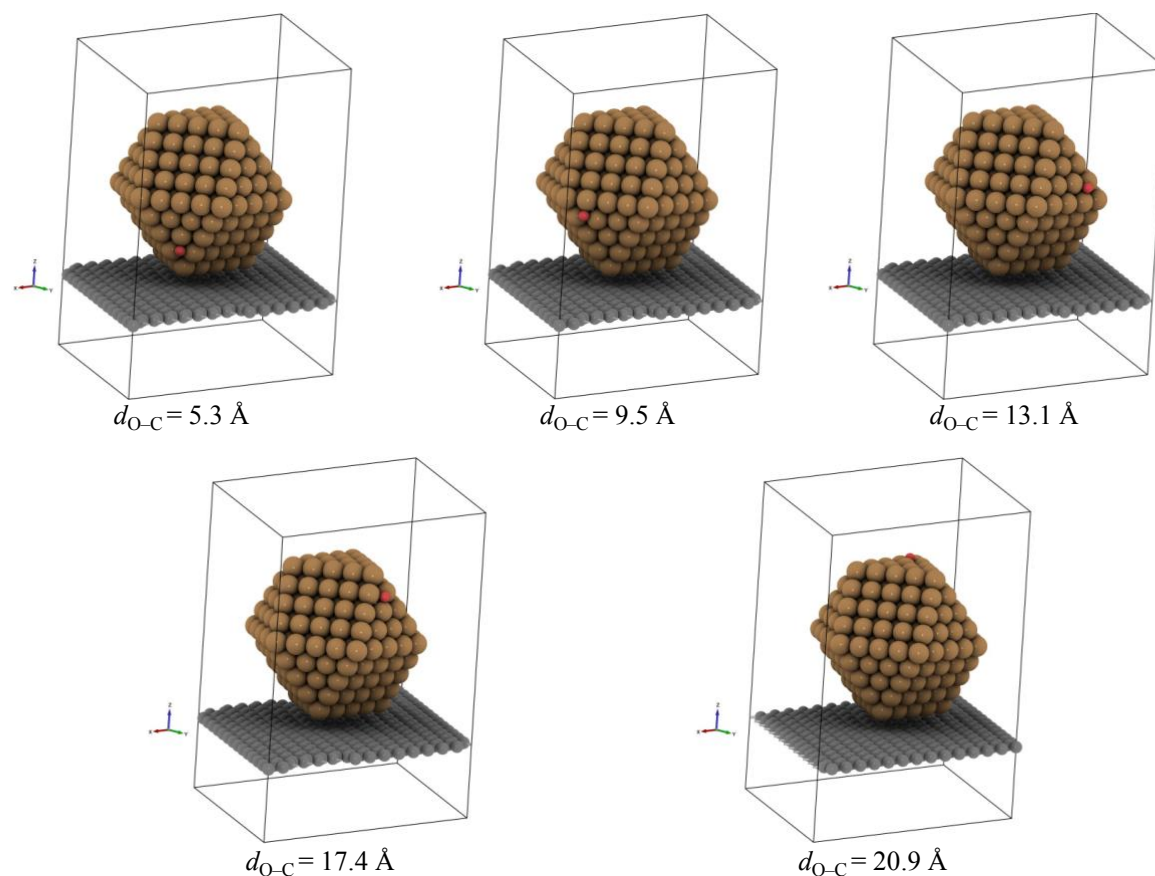
Figure 7.1. Optimized structures of Cu$_{309}$, with oxygen adsorbed on fcc corner positions of the particle, on graphene support. The distance between the oxygen atom and the carbon atom of the support (directly below it) is shown below each of the images of the structures.

In the models shown, graphene sheets were modelled using 288 carbon atoms for Cu$_{309}$ particles to maintain the distance of ~ 14 Å between the particles and their periodic images.

The oxygen adsorption energies (ΔE_O) on the copper NPs (Cu$_{147}$ and Cu$_{309}$) in the presence of the support, as a function of the distance of adsorbate (oxygen atoms) from the support, are depicted in **Figure 7.2**. From the plot comparing the oxygen adsorption energies calculated on the supported

Cu_{147} and Cu_{309} NPs with the values of the free-standing (dashed lines in the plot) NPs, it is evident that almost no significant change in the oxygen adsorption energy in the presence of the support is observable.
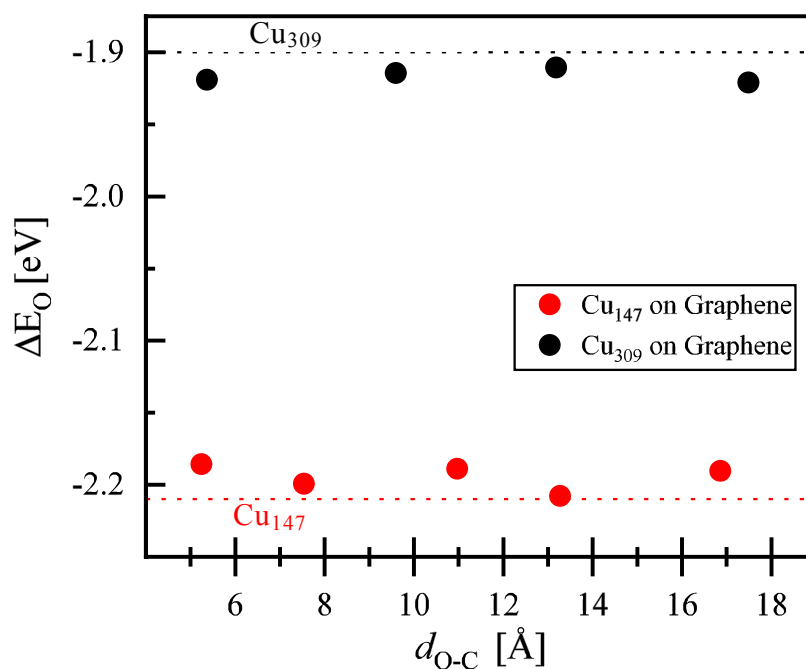
Figure 7.2. Calculated oxygen adsorption energies (ΔE_O) on Cu_{147} and Cu_{309} NPs as a function of the distance of adsorbate to the support (d_{O-C}). The dashed black and red lines show the reference values of the oxygen adsorption energies of the free-standing (gas phase) Cu_{147} and Cu_{309}, respectively. The oxygen adsorption energies are referenced to $1/2$ O_2 in the gas phase.

Furthermore, as **Figure 7.2** indicates, no significant difference between the oxygen adsorption energies calculated on the supported Cu_{147} and Cu_{309} NPs by varying the distance of the adsorbate to the support is obtained.

Moreover, further investigations on the Cu/C system, by introducing (functionalized) defects into the pristine structure of graphene, were performed. The models of defective graphene supports are illustrated in **Figure 7.3**.
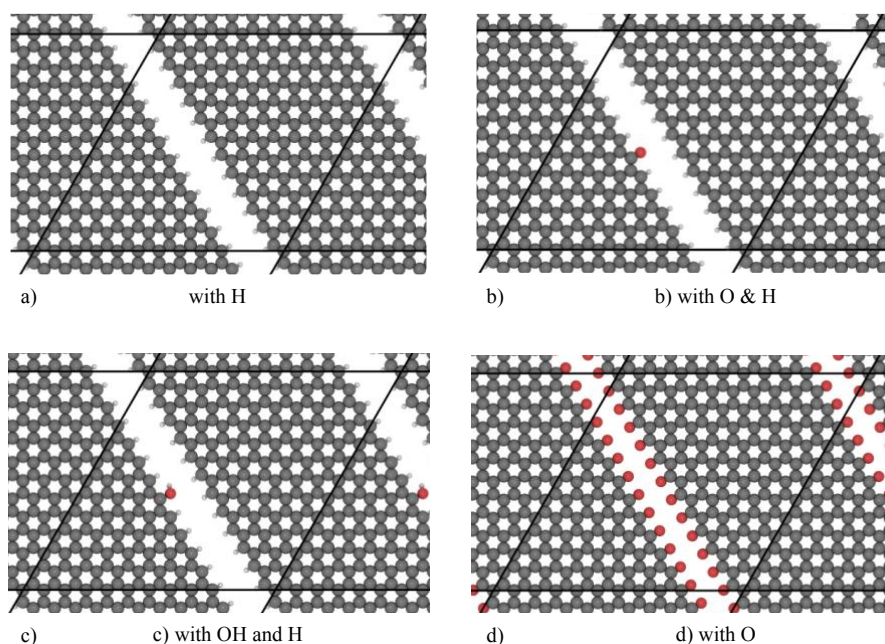
Figure 7.3. The functionalized defected graphene with a) hydrogen atoms, b) oxygen atom and hydrogen atoms, c) hydroxide molecule and hydrogen atoms, and d) with oxygen atoms. The generated gap on the graphene structure has ~5 Å width (C-C distance).

The influence of (functionalized) defective graphene on Cu NPs was done using oxygen adsorption energy on different positions (similar to calculations shown above) on Cu_{147}. In these calculations, the fixed-geometry models were used. All the atoms in the system kept constrained to their bulk values. The distance of the adsorbate to the Cu NP was obtained from the relaxation of the adsorbate on the metal slab (same as discussed in **Chapter 3**). The particle was placed on top of the functional group atom (H, O, OH), where the functional atom was located on the fcc adsorption site of {111} facet of the particle. The distance between the particle and the support was obtained from slab calculations of the relaxed functional atom on a fixed Cu slab.

Even though the introduction of the defect into the pristine graphene could provide an impact on the electronic structure of the Cu NP and, consequently, on the oxygen adsorption energy, this enhancement was not observed from the calculated adsorption energies. The biggest change in the oxygen adsorption energy of below 0.1 eV was obtained from the defective graphene-supported Cu_{147} particle.

After the ineffectiveness of the carbon support on the enhancement of the properties of studied copper NPs (with sizes between 1.5 nm to 2 nm) was confirmed, further studies on the particle size effect of copper catalyst by applying extended surface models were carried out. The particle size mentioned above is the possible range of disappearance of quantum size effect for copper nanoparticles.[200]

7.4 Particle Size Effect on Selectivity towards Methanol

The experimental investigations of our collaborators at the university of Utrecht showed a decrease in the methanol selectivity by increasing the conversion for all catalysts of different sizes. However, to illustrate the impact of particle size on selectivity, the changes in selectivity as a function of particle size at a constant conversion of ~5% are depicted in **Figure 7.4(a)**. The remarkable enhancement of the selectivity towards methanol over CO is observable for small NPs. The methanol selectivity drops from 34% to around 15% as the copper particle size changes from 4.7 nm to 19.4 nm.

To better understand the observed particle size effect, a separate comparison between the formation rates of MeOH and CO was considered. Turn-over frequencies (TOF) of methanol and CO are illustrated in **Figure 7.4(b)**. As can be seen, the TOF of carbon monoxide at 260 °C shows an increase from 1.9×10^{-3} s^{-1} to 9.4×10^{-3} s^{-1} as the Cu particle size increased from 5 nm to 20 nm. However, the average rate of methanol formation of 8.4×10^{-3} s^{-1} for the bigger particles suggests the size-independency of methanol TOF except for the smallest Cu particle size. Thus, methanol is much more favorable on smaller copper clusters, which show the highest methanol selectivity.

a)   b)
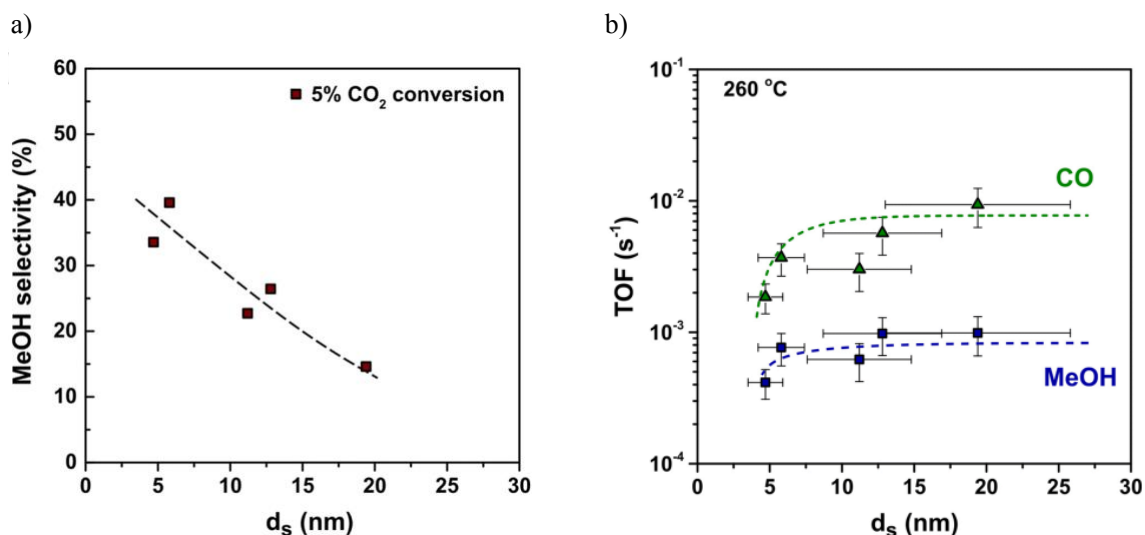
Figure 7.4. (a) MeOH selectivity as a function of copper particle size at a constant conversion of ~5% for CO$_2$. The added trendline is to guide the eye. Reaction conditions: 4.2 mg of Cu per reactor, 40 bar(g), 600 mL min^{-1} g$_{Cu}^{-1}$, H$_2$/CO$_2$/He = 67.5/22.5/10 vol%. (b) Turn-over frequency (TOF) of MeOH and CO as a function of the Cu particle size. Trendlines were added to guide the eye. Reaction conditions: 4.2 mg of Cu per reactor, 40 bar(g), 260 °C, 600 mL min^{-1} g$_{Cu}^{-1}$, H$_2$/CO$_2$/He = 67.5/22.5/10 vol%. The measurements of the catalyst's performance as well as the analysis of the data were performed by Laura Barberis and TEM measurements were performed by Nienke L. Visser, both at Utrecht university. Reproduced with permission from the Royal Society of Chemistry.

The smallest particles considered in the investigations of our experimental collaborators (the university of Utrecht) were in the range 3.9 ± 0.9 nm, which is just above the range where electronic particle size effects have been shown to disappear for copper nanoparticles, as e.g., evident from calculated adsorption energies that are essentially the same for all particles > 2.5 nm.[200] Another factor that is dependent on the particle size is the ratio of various surface terminations and it is thus useful to consider how the concentration of the various surface sites varies with particle size. This is shown in **Figure 7.5** where the fraction of surface atoms exhibiting a specific generalized coordination number (GCN)[246] is given as a function of particle size assuming ideal cuboctahedral

copper particles. It should be noted that this analysis assumes ideal particle shapes and that the aim is to deduct qualitative trends rather than quantitative numbers.
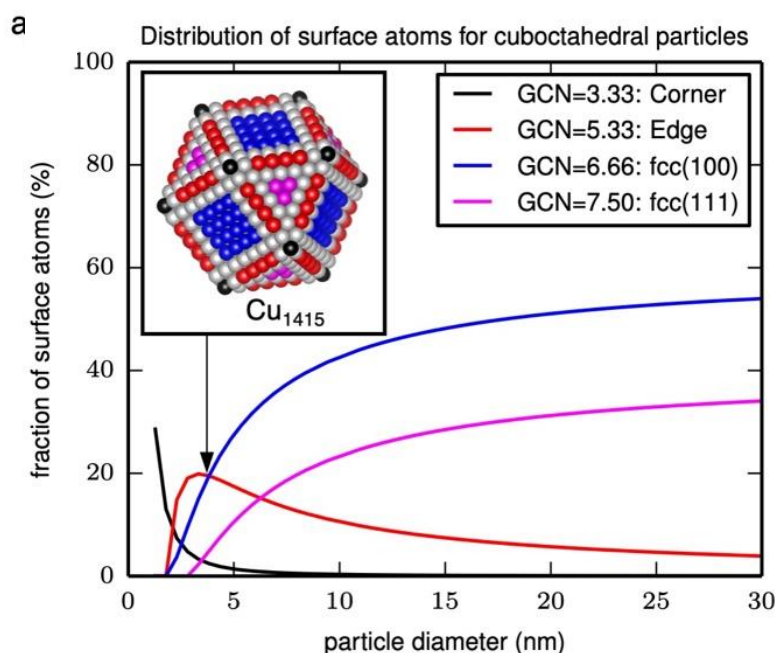
Figure 7.5. Fraction of surface atoms with a specific GCN as a function of particle diameter for cuboctahedral particles. GCN for the various surface atoms of a Cu_{1415} particle are shown in the inset. Reproduced with permission from the Royal Society of Chemistry.

Figure 7.5 shows that the number of edge sites with a GCN of 5.33 decreases from around 20% to less than 5% when going from 3 to 30 nm. On the other hand the fraction of the more close packed (111) and (100) facets increases from 3 and 10% to more than 30 and 50%, respectively. From the analysis of measured apparent activation energies for RWGS and methanol synthesis, it can be indicated that the two reactions are occurring at different sites on the copper nanoparticles. The decrease in RWGS rate with decreasing size seems related to a decrease of terrace sites (e.g., (100) surfaces).

Given that formate is the only intermediate that is found to have significant surface coverages, thus, in this theoretical study the adsorption free energy of formate on a range of different copper surfaces for coverages of up to 1 mono layer (ML) using density functional theory (DFT) was calculated (see **Figure 7.6**).
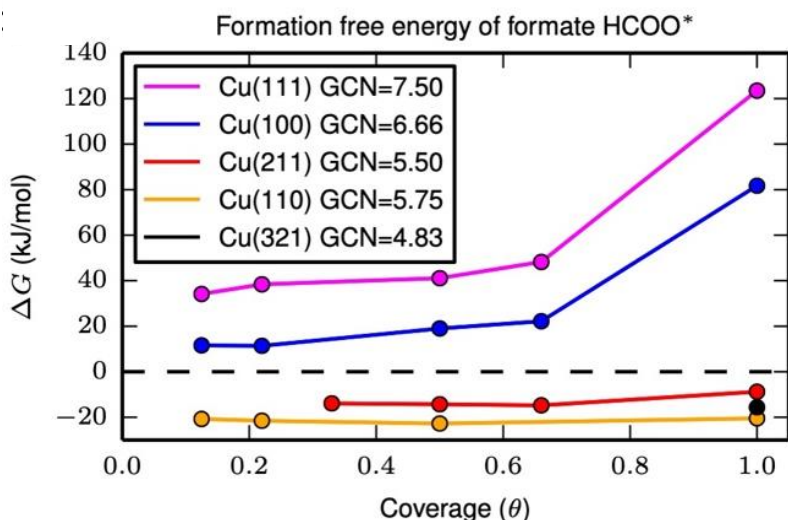
Figure 7.6. Adsorption free energy of formate as a function of coverage for Cu(111) (pink), Cu(100) (blue), Cu(211) (red), Cu(110) (orange) and Cu(321) (black) surfaces at 500 K and 1 bar of H_2 and CO_2. The coverage is normalized to 1 ML for one formate per two copper atoms of the corresponding facet (see **Table A.4** for structures).

The GCN for the models of edges ((211) and (110) surfaces) and corner atoms ((321) surface) differ slightly from that of the cuboctahedral particle, but they are close enough to be used as a rough guidance. The calculations reveal that the adsorption free energies decrease in the order Cu(321) $\approx$ Cu(110) > Cu(211) >> Cu(100) >> Cu(111). Interestingly, the effect of coverage (here 1 ML is defined as one formate per two copper surface atoms, see **Table A.4**) is small for the (211) and (110) surfaces but has a significant influence on the binding energy on Cu(111) and Cu(100). Importantly, at 500 K the adsorption free energy of formate on the (211) and (110) surfaces is negative, but positive on (111) and (100). This indicates that both (211) and (110) are covered by close to 1 ML of formate, while the coverage is significantly smaller on (100) and (111).
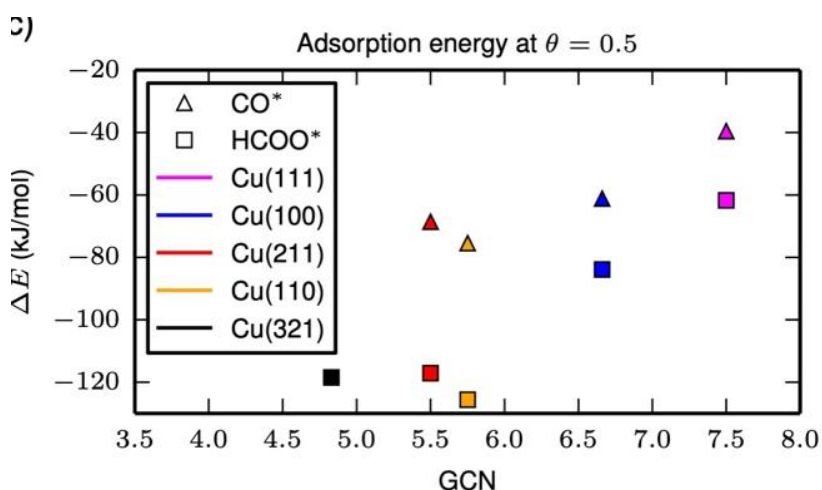
Figure 7.7. Adsorption energy of formate (squares) and CO (triangles) as a function of GCN.

Figure 7.7 shows the adsorption free energies of formate at a 1/2 ML coverage for the various surfaces as a function of the GCN. As can be seen, the adsorption free energies scale linearly with

the GCN. This allows to estimate adsorption free energies for the corner and edge sites of cuboctahedral particles (see **Figure 7.5**), shown here as open circles. For both facets, the adsorption free energy of formate is exothermic and thus a similar behavior as observed for (211), (110) and (321) facets is expected.

Assuming that formate can only be converted to methanol, this would indicate a strong preference of methanol formation on Cu(211) and Cu(110), which was used here to model the edge sites of the copper nanoparticles. On the other hand, the smaller coverage of formate on Cu(111) and Cu(100) might indicate that one or both of these sites are the predominate source for CO formation. Coverages of the carboxyl (COOH*) intermediate as well as CO* reveal similar trends and are given in the **Table A.4** and **Table A.5**. These findings roughly correlate with the analysis of the fraction of surface sites shown in **Figure 7.5**. This would explain why for the smallest Cu particles CO formation strongly decreases and hence overall the smallest particles give the highest MeOH selectively.

7.5 Conclusion of the Chapter

In this study, experimentally (the university of Utrecht) and theoretically, the effect of copper particle size in CO₂ hydrogenation reaction was investigated. Experimentally, copper catalysts with particle sizes between 5 and 20 nm over carbon support were studied. It was found that CO₂ hydrogenation is clearly a structure-sensitive reaction. Cu nanoparticles smaller than about 13 nm showed low activity but high MeOH selectivity. Furthermore, smaller particles showed higher MeOH selectivity. DFT calculations revealed that the formation free energy of formate, the main intermediate for methanol formation, is negative on the corner and edge sites. At the same time, it is positive on terrace sites, which are more abundant on larger particles. Therefore, small Cu nanoparticles having a surface dominated by the corner and edge sites, have a high ratio of methanol to CO formation, which can be explained by a higher formate coverage.

8 Final Conclusions and Outlooks

The fundamental understanding of catalysts' behavior to enhance their performance in catalytic reactions requires accurate computational models that simulate similar conditions of real systems. However, while computational studies of catalysts are mostly based on the extended surface models, some crucial effects, such as particle size and shape, and presence of support, are neglected. In this thesis, using cost-efficient fixed-geometry models of transition metals nanoparticles (NPs) combined with density functional theory (DFT) methods, the abovementioned important factors influencing the CO_2 hydrogenation reaction to produce methanol were investigated.

In the framework of this thesis, it is worth noting that employing the fixed-geometry models of the catalysts not only benefits from the accuracy of the DFT level but also provides a tremendous advantage in reducing the consumption of computing resources. It is vividly illustrated in **Figure 8.1(a)(b)**, where the computation time of the calculations (normalized by the number of computing system cores) is depicted as a function of the number of atoms in the systems for both relaxation and single-point calculations.
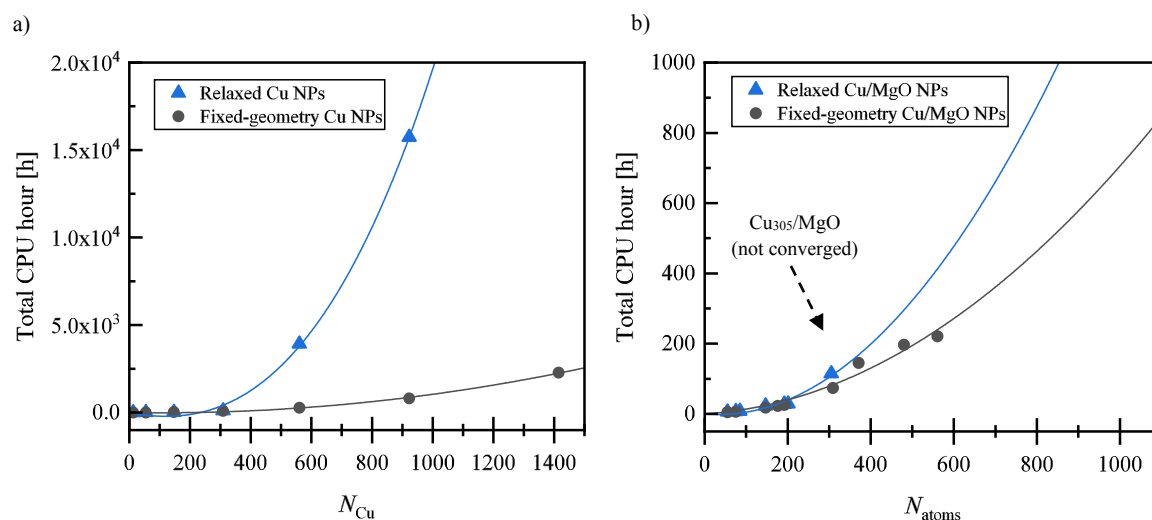
Figure 8.1. (a) The CPU hours used for the single-point energy calculations (dark grey circles) and optimizations (blue triangles) of the free-standing copper nanoparticles (NPs) as a function of the number of copper atoms in the particles. (b) The CPU hours used for optimization (blue triangles) and single-point energy calculations (dark grey circles) of MgO-supported copper NPs versus the number of atoms in the calculated systems. All the values are normalized by the number of computing system cores. The blue and dark grey lines represent the polynomial regression fitting of the plotted data for optimized and fixed-geometry structures, respectively. The data presented in the plot "a" and "b" are gathered from the calculated values of Chapters 3 and 5 of this thesis, respectively.

The significant differences in the cost of the calculations between the relaxation and single-point calculations prove the excellent efficiency of the applied fixed-geometry models of the un/supported copper particles. The data shown are related to the results in Chapters 3 and 5 of this thesis.

Indicating the efficiency of the applied models above, the findings throughout this thesis are summarized as follows:

In the first part of this thesis, intermediates the particle size effect on the adsorption energy of oxygen atom on coinage metals copper, silver, and gold was studied. It was found that surface relaxation has a relatively small impact on oxygen adsorption compared to particle size changes. Thus it allows the use of single-point calculations, which are less expensive than optimization of the structures. Therefore, the trends in adsorption energies of larger particles were captured. All three metals represented identical trends in adsorption energies, where M_{13} clusters illustrated the strongest adsorption, M_{55} weakest adsorption energy, and the trend approached smoothly to the bulk limit reached for M_{309}/M_{561} (2 nm to 2.5 nm). In addition, the quantum size effect on the smaller clusters was studied. Consequently, quite drastic changes in the oxygen adsorption energy (as much as 0.1 eV) on smaller clusters by adding or removing an atom to/from them were observed.

The second part covered the results of relating the applied method (in the previous part) to other transition metals from groups 9 and 10 in the periodic table of elements. Again the oxygen adsorption energy was used as a descriptor to capture the trends in the results obtained from particles of different sizes. Reaching the bulk limits was observed at different sizes for each metal NPs.. Interestingly, M_{13} indicated the strongest oxygen adsorption energy for all the metals studied. In addition, the influence of spin polarization on the properties of the transition metal NPs, as well as the changes in the magnetic moments by changing the size of NPs were investigated. It was shown that spin polarization slightly influences oxygen adsorption energy calculated on transition metals NPs studied.

The third part focused on the metal-support interactions from a systematic investigation using DFT calculations. This was done by investigating the influence of MgO as non-reducible oxide support and copper NPs of various sizes and shapes. It was shown that independent of the size and shape of the particles, the electronic effect of magnesia on the reactivity of Cu, measured by oxygen adsorption energy, is relatively small (about 0.1 eV). Only the adsorption site at the direct interface between Cu NPs and MgO, where the oxygen binds both to the support and the particle, illustrated a strong influence of the support. Introducing a nanowire model of MgO-supported metal (Cu) proved that such a model can represent supported (larger) copper nanoparticles. In addition, a general prediction from the comparison between the size, shape, and support effect on oxygen adsorption energy on a catalyst was presented. It was concluded that the particle size effect has the highest influence (0.7 eV for particles smaller than 1 nm). In contrast, the shape effect, studied by the difference in adsorption sites, has a slightly smaller effect (0.4 eV), and the MgO has the slightest influence among the others (0.1 eV).

In the fourth part, by benefiting from the utilized efficient models of metal NPs, adsorption energies of different intermediates in CO and CO_2 hydrogenation reactions, such as O, C, H, CO, HCOO, OH, CH_3O and H_2COOH, were investigated. The highest deviation of ~0.2 eV between the

calculated results of the adsorption energies of different intermediates on copper and nickel particles provided by less expensive single-point calculations and relaxations of the structures were obtained. Based on this proof of the accuracy of the results, the calculated adsorption energies showed linear scaling relationships with the adsorption energy of the atom through which they bind to the metal particles. In addition, particle size effects on the calculated adsorption energies of intermediate were observed.

The last part of this thesis sheds light on the influence of copper catalyst particle size on the CO_2 hydrogenation reaction is structure sensitive. Using DFT calculations on extended surface models revealed that the formation free energy of the main intermediate in CO_2 hydrogenation, formate (HCOO), is endergonic on the corner and edge sites, which constitute the higher fraction of surface atoms in small particles. In contrast, formate's calculated formation free energy on the terrace sites, which fractionally are more dominant on larger particles, was found to be exergonic. Thus, it was indicated that the small copper nanoparticles, which possess more corner and edge sites on their surfaces, have a higher ratio of methanol formation than CO.

In summary, this thesis efforted to shed light on essential topics in heterogeneous catalysis, specifically computational methods in catalysis. The results provided in this work are expected to pave the way toward modelling more complicated catalytic reactions and catalysts, as well as a better understanding of essential factors impacting methanol synthesis reaction. The presented findings concerned the particle size effect, the quantum size effect, and the different sizes at which different transition metals catalysts are expected to illustrate the bulk's properties can play essential roles in enhancing the performance of different catalytic reactions. Additionally, the influence of copper catalyst particle size on the activity and the selectivity of the catalyst, two important and hence mostly debated topics in methanol synthesis, was experimentally and theoretically demonstrated. Moreover, the studies on the influence of inert components (e.g., graphene) and non-reducible oxides (e.g., MgO) as support materials revealed a slight influence of the support on the properties of the NPs, except for adsorption positions at the interface between the catalyst and the oxidic support. The presented work provided opportunities for future investigations and simulations of more complicated catalysts supported on reducible oxides (e.g., CeO_2 or ZnO) in which the electron donation could play a more prominent role. In addition, the nature of support's impact on the electronic structure of the catalyst, concerning the interactions between the catalyst and the support, could be understood by the investigations of potential dispersion forces between them. Furthermore, it was shown that using even more efficient nanowire (NW) models of the catalysts accompanied by the generalized coordination number (GCN) descriptor can discriminate the adsorption sites and, consequently, describe the catalyst's particle shape effect. Lastly, it was shown that the particle size effect on the adsorption energies of different intermediates in CO_2 hydrogenation reaction combined with the scaling relations between the adsorption energies of the adsorbates could be helpful in predicting the behavior of copper catalysts with different sizes toward different intermediates with the benefit of lowering the cost of calculations using fixed-geometry models.

References

[1]   UN (**2015**) The Paris Agreement. United Nations.
        https://unfccc.int/sites/default/files/english_paris_agreement.pdf
[2]   P. Tans and R. Keeling, "Trends in atmospheric carbon dioxide, noaa/esrl," URL:
        http://www.esrl.noaa.gov/gmd/ccgg/trends, 2020.
[3]   D. Luthi, et al.. 2008; Etheridge, D.M., et al. 2010; Vostok ice core data/J.R. Petit et al.; NOAA
        Mauna Loa CO2 record.
[4]   J. R. Petit, J. Jouzel, D. Raynaud, N. I. Barkov, J. M. Barnola, I. Basile, M. Bender, J. Chappellaz,
        M. Davis, G. Delaygue, M. Delmotte, V. M. Kotlyakov, M. Legrand, V. Y. Lipenkov, C. Lorius,
        L. Pepin, C. Ritz, E. Saltzman, M. Stievenard, *Nature* **1999**, *399*, 429-436.
[5]   N. G. C. Change, G. W. V. S. of the Planet. Jet Propulsion Laboratory / National Aeronautics, and
        S. Administration, "Global climate change: Evidence.," URL: http://climate.nasa.gov/evidence,
        2017.
[6]   J. Fourier, in *Annales de Chemie et de Physique, Vol. 27*, **1824**, pp. 136-167.
[7]   AAAS, **1857**, Proceedings of the American Association for the Advancement of Science. Tenth
        Meeting, held at Albany, New York, August, 1856. Joseph Lovering, Cambridge, 258 p.
[8]   J. Tyndall, *Proceedings of the Royal Society of London* **1860**, 37-39.
[9]   J. Tyndall, *Philosophical Transactions of the Royal Society of London* **1861**, 1-36.
[10]   S. Arrhenius, *The London, Edinburgh, and Dublin Philosophical Magazine and Journal of Science*
        1896, *41*, 237-276.
[11]   Rodney and Otamatea Times, Waitemata and Kaipara Gazette, 14 August **1912**, Page 7.
[12]   Certain data included herein are derived from Clarivate Web of Science. © Copyright Clarivate
        202___. All rights reserved.
[13]   R. Boyle, *The works of the honourable Robert Boyle* **1661**, *1*, 1965-1966.
[14]   G. A. Olah, *Angew Chem Int Edit* **2005**, *44*, 2636-2639.
[15]   A. Khassin, T. Minyukova, *Catalysis in Industry* **2022**, *14*, 31-41.
[16]   M. Bukhtiyarova, T. Lunkenbein, K. Kahler, R. Schlogl, *Catalysis Letters* **2017**, *147*, 416-427.
[17]   I. U. Din, M. S. Shaharun, M. A. Alotaibi, A. I. Alharthi, A. Naeem, *J Co2 Util* **2019**, *34*, 20-33.
[18]   S. Kanuri, S. Roy, C. Chakraborty, S. P. Datta, S. A. Singh, S. Dinda, *Int J Energ Res* **2022**, *46*,
        5503-5522.
[19]   Rynok metanola: tekushchaya situatsiya i perspektivy (Market of Methanol: State-of-the-Art and
        Prospects) https://assets.ey.com/content/dam/ey-sites/ey-com/ ru_ru/topics/industrial-products/ey-
        methanol-market-overview-october-2020-rus.pdf?download. Cited May 25, **2021**.
[20]   W. Wang, S. P. Wang, X. B. Ma, J. L. Gong, *Chemical Society Reviews* **2011**, *40*, 3703-3727.
[21]   X. L. Du, Z. Jiang, D. S. Su, J. Q. Wang, *Chemsuschem* **2016**, *9*, 322-332.
[22]   H. Ahouari, A. Soualah, A. Le Valant, L. Pinard, P. Magnoux, Y. Pouilloux, *React Kinet Mech
        Cat* **2013**, *110*, 131-145.
[23]   L. C. Grabow, M. Mavrikakis, *Acs Catalysis* **2011**, *1*, 365-384.
[24]   V. N. Ipatieff, G. S. Monroe, *Journal of the American Chemical Society* **1945**, *67*, 2168-2171.
[25]   K. Klier, *Adv Catal* **1982**, *31*, 243-313.
[26]   K. Klier, V. Chatikavanij, R. G. Herman, G. W. Simmons, *Journal of Catalysis* **1982**, *74*, 343-360.
[27]   G. Liu, D. Willcox, M. Garland, H. H. Kung, *Journal of Catalysis* **1985**, *96*, 251-260.
[28]   G. C. Chinchen, P. J. Denny, D. G. Parker, M. S. Spencer, D. A. Whan, *Applied Catalysis* **1987**,
        30, 333-338.
[29]   Y. Yang, C. A. Mims, D. H. Mei, C. H. F. Peden, C. T. Campbell, *Journal of Catalysis* **2013**, *298*,
        10-17.
[30]   E. L. Kunkes, F. Studt, F. Abild-Pedersen, R. Schlogl, M. Behrens, *Journal of Catalysis* **2015**,
        328, 43-48.

[31]   M. Behrens, F. Studt, I. Kasatkin, S. Kuhl, M. Havecker, F. Abild-Pedersen, S. Zander, F. Girgsdies, P. Kurr, B. L. Kniep, M. Tovar, R. W. Fischer, J. K. Norskov, R. Schlogl, *Science* **2012**, *336*, 893-897.

[32]   R. Guil-Lopez, N. Mota, J. Llorente, E. Millan, B. Pawelec, J. L. G. Fierro, R. M. Navarro, *Materials* **2019**, *12*.

[33]   Y. F. Zhao, Y. Yang, C. Mims, C. H. F. Peden, J. Li, D. H. Mei, *Journal of Catalysis* **2011**, *281*, 199-211.

[34]   M. D. Porosoff, B. H. Yan, J. G. G. Chen, *Energy & Environmental Science* **2016**, *9*, 62-73.

[35]   Z. M. Hu, K. Takahashi, H. Nakatsuji, *Surface Science* **1999**, *442*, 90-106.

[36]   P. B. Rasmussen, P. M. Holmblad, T. Askgaard, C. V. Ovesen, P. Stoltze, J. K. Norskov, I. Chorkendorff, *Catalysis Letters* **1994**, *26*, 373-381.

[37]   P. B. Rasmussen, M. Kazuta, I. Chorkendorff, *Surface Science* **1994**, *318*, 267-380.

[38]   J. Yoshihara, C. T. Campbell, *Journal of Catalysis* **1996**, *161*, 776-782.

[39]   Q. J. Hong, Z. P. Liu, *Surface Science* **2010**, *604*, 1869-1876.

[40]   J. J. Wang, G. N. Li, Z. L. Li, C. Z. Tang, Z. C. Feng, H. Y. An, H. L. Liu, T. F. Liu, C. Li, *Sci Adv* **2017**, *3*.

[41]   S. E. Collins, M. A. Baltanas, A. L. Bonivardi, *Journal of Catalysis* **2004**, *226*, 410-421.

[42]   J. Y. Ye, C. J. Liu, D. H. Mei, Q. F. Ge, *Journal of Catalysis* **2014**, *317*, 44-53.

[43]   Y. X. Yang, J. Evans, J. A. Rodriguez, M. G. White, P. Liu, *Phys Chem Chem Phys* **2010**, *12*, 9909-9917.

[44]   A. Baiker, *J Mol Catal A Chem* **2000**, *163*, 205-220.

[45]   J. K. Norskov, T. Bligaard, J. Rossmeisl, C. H. Christensen, *Nature Chemistry* **2009**, *1*, 37-46.

[46]   C. Costentin, M. Robert, J. M. Saveant, *Accounts Chem Res* **2015**, *48*, 2996-3006.

[47]   I. Funes-Ardoiz, F. Schoenebeck, *Chem* **2020**, *6*, 1904-1913.

[48]   F. Abild-Pedersen, J. Greeley, F. Studt, J. Rossmeisl, T. R. Munter, P. G. Moses, E. Skulason, T. Bligaard, J. K. Norskov, *Physical Review Letters* **2007**, *99*.

[49]   F. Studt, I. Sharafutdinov, F. Abild-Pedersen, C. F. Elkjær, J. S. Hummelshøj, S. Dahl, I. Chorkendorff, J. K. Nørskov, *Nature chemistry* **2014**, *6*, 320.

[50]   F. Studt, I. Sharafutdinov, F. Abild-Pedersen, C. F. Elkjaer, J. S. Hummelshoj, S. Dahl, I. Chorkendorff, J. K. Norskov, *Nature Chemistry* **2014**, *6*, 320-324.

[51]   A. T. Bell, *Science* **2003**, *299*, 1688-1691.

[52]   Y. Ma, P. B. Balbuena, *Surface Science* **2008**, *602*, 107-113.

[53]   I. Swart, F. M. F. de Groot, B. M. Weckhuysen, P. Gruene, G. Meijer, A. Fielicke, *Journal of Physical Chemistry A* **2008**, *112*, 1139-1149.

[54]   H. Liu, J. Guan, X. Mu, G. Xu, X. Wang, X. Chen, *Encyclopedia of Physical Organic Chemistry* **2016**, 1-75.

[55]   E. Roduner, *Chem Soc Rev* **2006**, *35*, 583-592.

[56]   T. Tsukuda, H. Häkkinen, *Protected metal clusters: from fundamentals to applications*, Elsevier, **2015**.

[57]   G. Ertl, et al., *Handbook of heterogeneous catalysis*, 2nd, completely rev. and enl. ed., Wiley-VCH, Weinheim, **2008**.

[58]   S. Laurent, D. Forge, M. Port, A. Roch, C. Robic, L. V. Elst, R. N. Muller, *Chem Rev* **2008**, *108*, 2064-2110.

[59]   M. B. Gawande, P. S. Branco, K. Parghi, J. J. Shrikhande, R. K. Pandey, C. A. A. Ghumman, N. Bundaleski, O. M. N. D. Teodoro, R. V. Jayaram, *Catal Sci Technol* **2011**, *1*, 1653-1664.

[60]   A. S. K. Hashmi, G. J. Hutchings, *Angewandte Chemie International Edition* **2006**, *45*, 7896-7936.

[61]   J. Kleis, J. Greeley, N. Romero, V. Morozov, H. Falsig, A. H. Larsen, J. Lu, J. J. Mortensen, M. Dułak, K. S. Thygesen, *Catal lett* **2011**, *141*, 1067-1071.

[62]   L. Li, F. Abild-Pedersen, J. Greeley, J. K. Norskov, *J Phys Chem Lett* **2015**, *6*, 3797-3801.

[63]   R. Van Hardeveld, F. Hartog, *Surface Science* **1969**, *15*, 189-230.

[64]   R. A. Van Santen, *Accounts Chem Res* **2009**, *42*, 57-66.

[65]   A. S. Crampton, M. D. Rötzer, C. J. Ridge, F. F. Schweinberger, U. Heiz, B. Yoon, U. Landman, *Nat Commun* **2016**, *7*, 1-12.

[66]   P. van Helden, I. M. Ciobîcă, R. L. Coetzer, *Catalysis Today* **2016**, *261*, 48-59.

[67]   M. Boudart, *Adv Catal* **1969**, *20*, 153-166.

[68]   G. A. Somorjal, J. Carrazza, *Ind Eng Chem Fund* **1986**, *25*, 63-69.

[69]   C. R. Henry, *Surf Sci Rep* **1998**, *31*, 235-325.

[70]   G. L. Bezemer, J. H. Bitter, H. P. C. E. Kuipers, H. Oosterbeek, J. E. Holewijn, X. D. Xu, F. Kapteijn, A. J. van Dillen, K. P. de Jong, *Journal of the American Chemical Society* **2006**, *128*, 3956-3964.

[71]   H. M. T. Galvis, J. H. Bitter, T. Davidian, M. Ruitenbeek, A. I. Dugulan, K. P. de Jong, *Journal of the American Chemical Society* **2012**, *134*, 16207-16215.

[72]   B. Roldan Cuenya, F. Behafarid, *Surf Sci Rep* **2015**, *70*, 135-187.

[73]   R. van den Berg, G. Prieto, G. Korpershoek, L. I. van der Wal, A. J. van Bunningen, S. Laegsgaard-Jorgensen, P. E. de Jongh, K. P. de Jong, *Nat Commun* **2016**, *7*.

[74]   H. N. P. E. Hansen JB, *, in Handbook of Heterogeneous Catalysis, Ertl G, Knözinger H, Schüth F, Weitkamp J (Wiley-VCH, Weinheim, Germany, ed. 2, 2008).*

[75]   M. Haruta, T. Kobayashi, H. Sano, N. Yamada, *Chem Lett* **1987**, *16*, 405-408.

[76]   J. M. Thomas, W. J. Thomas, *Principles and practice of heterogeneous catalysis*, VCH, Weinheim ; New York, **1997**.

[77]   M. Valden, X. Lai, D. Goodman, *science* **1998**, *281*, 1647-1650.

[78]   G. Ertl, *Angewandte Chemie International Edition* **2008**, *47*, 3524-3535.

[79]   G. A. Somorjai, J. Y. Park, *Chemical Society Reviews* **2008**, *37*, 2155-2162.

[80]   Y. Li, G. A. Somorjai, *Nano Lett* **2010**, *10*, 2289-2295.

[81]   G. Bond, D. Thompson, *Catal Rev-Sci Eng* **1999**, *41*, 319-388.

[82]   L. Li, A. H. Larsen, N. A. Romero, V. A. Morozov, C. Glinsvad, F. Abild-Pedersen, J. Greeley, K. W. Jacobsen, J. K. Nørskov, *The journal of physical chemistry letters* **2012**, *4*, 222-226.

[83]   S. H. Overbury, P. A. Bertrand, G. A. Somorjai, *Chem Rev* **1975**, *75*, 547-560.

[84]   Z. P. Qu, W. X. Huang, S. T. Zhou, H. Zheng, X. M. Liu, M. J. Cheng, X. H. Bao, *Journal of Catalysis* **2005**, *234*, 33-36.

[85]   S. De, S. Duttab, B. Saha, *Catal Sci Technol* **2016**, *6*, 7364-7385.

[86]   N. Masoud, B. Donoeva, P. E. de Jongh, *Appl Catal a-Gen* **2018**, *561*, 150-157.

[87]   Y. H. Sun, L. M. Chen, Y. F. Bao, G. N. Wang, Y. J. Zhang, M. L. Fu, J. L. Wu, D. Q. Ye, *Catalysis Today* **2018**, *307*, 212-223.

[88]   D. Z. Gao, H. B. Yin, Y. H. Feng, A. L. Wang, *Can J Chem Eng* **2015**, *93*, 1107-1118.

[89]   M. Kurtz, H. Wilmer, T. Genger, O. Hinrichsen, M. Muhler, *Catalysis Letters* **2003**, *86*, 77-80.

[90]   H. Tao, Y. Li, X. Cai, H. Zhou, Y. Li, W. Lin, S. Huang, K. Ding, W. Chen, Y. Zhang, *The Journal of Physical Chemistry C* **2019**, *123*, 24118-24132.

[91]   M. Shekhar, J. Wang, W.-S. Lee, W. D. Williams, S. M. Kim, E. A. Stach, J. T. Miller, W. N. Delgass, F. H. Ribeiro, *Journal of the American Chemical Society* **2012**, *134*, 4700-4708.

[92]   Z. J. Zhao, Z. L. Li, Y. R. Cui, H. Y. Zhu, W. F. Schneider, W. N. Delgass, F. Ribeiro, J. Greeley, *Journal of Catalysis* **2017**, *345*, 157-169.

[93]   K. Larmier, W. C. Liao, S. Tada, E. Lam, R. Verel, A. Bansode, A. Urakawa, A. Comas-Vives, C. Coperet, *Angew Chem Int Edit* **2017**, *56*, 2318-2323.

[94]   R. LeSar, *Introduction to computational materials science: fundamentals to applications*, Cambridge University Press, **2013**.

[95]   N. W. Ashcroft, N. D. Mermin, *Appendix N* **2010**, *166*, 87.

[96]   R. G. Parr, *Oxford University Press* **1989**, *1*, 1989.

[97]   R. Dreizler, E. Gross, Berlin New York, **1990**.

[98]   R. M. Martin, *Electronic structure: basic theory and practical methods*, Cambridge university press, **2020**.

[99]   P. Hohenberg, W. Kohn, *Physical review* **1964**, *136*, B864.

[100]   J. P. Perdew, K. Schmidt, *Van Doren, V* **2001**, 1-20.

[101]   I. Y. Zhang, X. Xu, *Wires Comput Mol Sci* **2021**, *11*.

[102]   W. Carr Jr, *Physical Review* **1961**, *122*, 1437.

[103]   W. Carr Jr, A. Maradudin, *Physical Review* **1964**, *133*, A371.

[104]   U. Von Barth, L. Hedin, *Journal of Physics C: Solid State Physics* **1972**, *5*, 1629.

[105]   J. P. Perdew, P. Ziesche, H. Eschrig, Akademie Verlag, Berlin, **1991**.

[106]   J. P. Perdew, K. Burke, M. Ernzerhof, *Physical Review Letters* **1996**, *77*, 3865-3868.

[107]   A. D. Becke, *Phys Rev A* **1988**, *38*, 3098.

[108]   C. Lee, W. Yang, R. G. Parr, *Physical review B* **1988**, *37*, 785.

[109]   J. Tao, J. P. Perdew, V. N. Staroverov, G. E. Scuseria, *Physical Review Letters* **2003**, *91*, 146401.

[110]   G. I. Csonka, J. P. Perdew, A. Ruzsinszky, P. H. T. Philipsen, S. Lebegue, J. Paier, O. A. Vydrov, J. G. Angyan, *Physical Review B* **2009**, *79*.

[111]   V. N. Staroverov, G. E. Scuseria, J. M. Tao, J. P. Perdew, *J Chem Phys* **2003**, *119*, 12129-12137.

[112]   Y. Zhao, D. G. Truhlar, *Journal of Chemical Theory and Computation* **2005**, *1*, 415-432.

[113]   Y. Zhao, D. G. Truhlar, *Journal of Physical Chemistry A* **2005**, *109*, 5656-5667.

[114]   A. D. Becke, *J Chem Phys* **1993**, *98*, 1372-1377.

[115]   P. J. Stephens, F. J. Devlin, C. F. Chabalowski, M. J. Frisch, *The Journal of physical chemistry* **1994**, *98*, 11623-11627.

References

[116]   R. H. Hertwig, W. Koch, *Chem Phys Lett* **1997**, *268*, 345-351.
[117]   M. Ernzerhof, G. E. Scuseria, *The Journal of chemical physics* **1999**, *110*, 5029-5036.
[118]   F. Jensen, *Introduction to computational chemistry*, John wiley & sons, **2017**.
[119]   H. L. Williams, C. F. Chabalowski, *The Journal of Physical Chemistry A* **2001**, *105*, 646-659.
[120]   Y. Andersson, E. Hult, H. Rydberg, P. Apell, B. I. Lundqvist, D. C. Langreth, in *Electronic Density Functional Theory*, Springer, **1998**, pp. 243-260.
[121]   O. A. Vydrov, T. Van Voorhis, *Physical review letters* **2009**, *103*, 063004.
[122]   S. Grimme, *J Comput Chem* **2004**, *25*, 1463-1473.
[123]   S. Grimme, *J Comput Chem* **2006**, *27*, 1787-1799.
[124]   S. Grimme, J. Antony, S. Ehrlich, H. Krieg, *The Journal of chemical physics* **2010**, *132*, 154104.
[125]   B. Hammer, L. B. Hansen, J. K. Nørskov, *Physical review B* **1999**, *59*, 7413.
[126]   J. Wellendorff, K. T. Lundgaard, A. Møgelhøj, V. Petzold, D. D. Landis, J. K. Nørskov, T. Bligaard, K. W. Jacobsen, *Physical Review B* **2012**, *85*, 235149.
[127]   J. Wellendorff, T. L. Silbaugh, D. Garcia-Pintos, J. K. Nørskov, T. Bligaard, F. Studt, C. T. Campbell, *Surface Science* **2015**, *640*, 36-44.
[128]   M. Frisch, *Accurate and simple analytic representation of the electron-gas correlation energy. Phys. Rev. B* **1992**, *45*, 13244-13249.
[129]   J. Tao, J. P. Perdew, H. Tang, C. Shahi, *The Journal of Chemical Physics* **2018**, *148*, 074110.
[130]   K. Lee, É. D. Murray, L. Kong, B. I. Lundqvist, D. C. Langreth, *Physical Review B* **2010**, *82*, 081101.
[131]   J. C. Slater, *Physical Review* **1930**, *36*, 57.
[132]   S. Boys, *Proc. R. Soc. London. Ser. A* **1950**, *200*, 532-540.
[133]   F. Bloch, *Zeitschrift für physik* **1929**, *52*, 555-600.
[134]   P. E. Blöchl, *Physical review B* **1994**, *50*, 17953.
[135]   G. Kresse, D. Joubert, *Physical review b* **1999**, *59*, 1758.
[136]   D. A. McQuarrie, *Statistical mechanics*, Sterling Publishing Company, **2000**.
[137]   A. A. Peterson, F. Abild-Pedersen, F. Studt, J. Rossmeisl, J. K. Nørskov, *Energy & Environmental Science* **2010**, *3*, 1311-1315.
[138]   D. W. Blaylock, T. Ogura, W. H. Green, G. J. Beran, *The Journal of Physical Chemistry C* **2009**, *113*, 4898-4908.
[139]   F. Studt, F. Abild-Pedersen, J. B. Varley, J. K. Nørskov, *Catalysis letters* **2013**, *143*, 71-73.
[140]   K. H. Ertl G, Schüth F, Weitkamp J, Handbook of heterogeneous catalysis (Wiley, 2008).
[141]   N. Mizuno, M. Misono, *Chem Rev* **1998**, *98*, 199-218.
[142]   A. T. Bell, *Science* **2003**, *299*, 1688-1691.
[143]   C. Bartholomew, R. Farrauto, in *Fundamentals of Industrial Catalytic Processes, Vol. 2*, John Wiley & Sons, Inc, Hoboken, NJ, **2005**.
[144]   Q. Xu, K. C. Kharas, B. J. Croley, A. K. Datye, *Chemcatchem* **2011**, *3*, 1004-1014.
[145]   M. Valden, X. Lai, D. W. Goodman, *Science* **1998**, *281*, 1647-1650.
[146]   G. C. Bond, D. T. Thompson, *Catal Rev* **1999**, *41*, 319-388.
[147]   M. Haruta, T. Kobayashi, H. Sano, N. Yamada, *Chem Lett* **1987**, 405-408.
[148]   J. X. Liu, I. A. W. Filot, Y. Su, B. Zijlstra, E. J. M. Hensen, *J Phys Chem C Nanomaterials and Interfaces* **2018**, *122*, 8327-8340.
[149]   A. H. Larsen, J. Kleis, K. S. Thygesen, J. K. Norskov, K. W. Jacobsen, *Phys Rev B* **2011**, *84*, 245429.
[150]   S. S. Laletina, M. Mamatkulov, E. A. Shor, V. V. Kaichev, A. Genest, I. V. Yudanov, N. Rosch, *J Phys Chem C* **2017**, *121*, 17371-17377.
[151]   I. V. Yudanov, A. Genest, S. Schauermann, H. J. Freund, N. Rosch, *Nano Lett* **2012**, *12*, 2134-2139.
[152]   J. H. Fischer-Wolfarth, J. A. Farmer, J. M. Flores-Camacho, A. Genest, I. V. Yudanov, N. Rosch, C. T. Campbell, S. Schauermann, H. J. Freund, *Phys Rev B* **2010**, *81*.
[153]   M. Behrens, F. Studt, I. Kasatkin, S. Kuhl, M. Havecker, F. Abild-Pedersen, S. Zander, F. Girgsdies, P. Kurr, B. L. Kniep, M. Tovar, R. W. Fischer, J. K. Norskov, R. Schlogl, *Science* **2012**, *336*, 893-897.
[154]   P. L. Hansen, J. B. Wagner, S. Helveg, J. R. Rostrup-Nielsen, B. S. Clausen, H. Topsoe, *Science* **2002**, *295*, 2053-2055.
[155]   K. K. Hinrichsen KO, Muhler M, in Handbook of Heterogeneous Catalysis, Ertl G, Knözinger H, Schüth F, Weitkamp J (Wiley-VCH, Weinheim, Germany, ed. 2, 2008).
[156]   B. A. Mallat T, in Handbook of Heterogeneous Catalysis, Ertl G, Knözinger H, Schüth F, Weitkamp J (Wiley-VCH, Weinheim, Germany, ed. 2, 2008).

[157] A. H. Weissermel K, Industrial Organic Chemistry (VCH, New York, 1993**)**.

[158] R. van den Berg, G. Prieto, G. Korpershoek, L. I. van der Wal, A. J. van Bunningen, S. Laegsgaard-Jorgensen, P. E. de Jongh, K. P. de Jong, *Nat Commun* **2016**, *7*, 13057.

[159] B. Yang, C. Liu, A. Halder, E. C. Tyo, A. B. Martinson, S. n. Seifert, P. Zapol, L. A. Curtiss, S. Vajda, *The Journal of Physical Chemistry C* **2017**, *121*, 10406-10412.

[160] L. Ma, J. Akola, *Phys Chem Chem Phys* **2019**, *21*, 11351-11358.

[161] S. Peredkov, S. Peters, M. Al-Hada, A. Erko, M. Neeb, W. Eberhardt, *Catal Sci Technol* **2016**, *6*, 6942-6952.

[162] W. Dononelli, T. Kluner, *Faraday Discuss* **2018**, *208*, 105-121.

[163] J. F. Blandez, A. Primo, A. M. Asiri, M. Alvaro, H. Garcia, *Angew Chem Int Edit* **2014**, *53*, 12581-12586.

[164] Y. Han, K. C. Lai, A. Lii-Rosales, M. C. Tringides, J. W. Evans, P. A. Thiela, *Surface Science* **2019**, *685*, 48-58.

[165] R. Reske, H. Mistry, F. Behafarid, B. Roldan Cuenya, P. Strasser, *Journal of the American Chemical Society* **2014**, *136*, 6978-6986.

[166] B. Delley, D. E. Ellis, A. J. Freeman, E. J. Baerends, D. Post, *Physical Review B* **1983**, *27*, 2132-2144.

[167] X. Zhang, J. X. Liu, B. Zijlstra, I. A. W. Filot, Z. Y. Zhou, S. G. Sun, E. J. M. Hensen, *Nano Energy* **2018**, *43*, 200-209.

[168] P. Christopher, S. Linic, *Chemcatchem* **2010**, *2*, 78-83.

[169] V. I. Bukhtiyarov, A. F. Carley, L. A. Dollard, M. W. Roberts, *Surface Science* **1997**, *381*, L605-L608.

[170] T. Tsuneda, *J Comput Chem* **2019**, *40*, 206-211.

[171] G. Kresse, J. Hafner, *Physical Review B* **1993**, *47*, 558-561.

[172] G. Kresse, J. Hafner, *Physical Review B* **1994**, *49*, 14251-14269.

[173] G. Kresse, J. Furthmuller, *Physical Review B* **1996**, *54*, 11169-11186.

[174] G. Kresse, J. Furthmuller, *Comp Mater Sci* **1996**, *6*, 15-50.

[175] A. H. Larsen, J. J. Mortensen, J. Blomqvist, I. E. Castelli, R. Christensen, M. Dulak, J. Friis, M. N. Groves, B. Hammer, C. Hargus, E. D. Hermes, P. C. Jennings, P. B. Jensen, J. Kermode, J. R. Kitchin, E. L. Kolsbjerg, J. Kubal, K. Kaasbjerg, S. Lysgaard, J. B. Maronsson, T. Maxson, T. Olsen, L. Pastewka, A. Peterson, C. Rostgaard, J. Schiotz, O. Schutt, M. Strange, K. S. Thygesen, T. Vegge, L. Vilhelmsen, M. Walter, Z. H. Zeng, K. W. Jacobsen, *J Phys-Condens Mat* **2017**, *29*.

[176] E. Dietze, P. N. Plessow, F. Studt, *J Phys Chem C* **2019**, *123*, 25464-25469.

[177] J. Meija, B. Coplen Tyler, M. Berglund, A. Brand Willi, P. De Bièvre, M. Gröning, E. Holden Norman, J. Irrgeher, D. Loss Robert, T. Walczyk, T. Prohaska, in *Pure Appl. Chem., Vol. 88*, **2016**, p. 265.

[178] J. Meija, T. B. Coplen, M. Berglund, W. A. Brand, P. De Bievre, M. Groning, N. E. Holden, J. Irrgeher, R. D. Loss, T. Walczyk, T. Prohaska, *Pure Appl Chem* **2016**, *88*, 265-291.

[179] J. Wachter, *Angewandte Chemie* **1988**, *100*, 1624-1625.

[180] M. Mavrikakis, B. Hammer, J. K. Norskov, *Physical Review Letters* **1998**, *81*, 2819-2822.

[181] H. J. Wei, C. Gomez, J. J. Liu, N. Guo, T. P. Wu, R. Lobo-Lapidus, C. L. Marshall, J. T. Miller, R. J. Meyer, *J Catal* **2013**, *298*, 18-26.

[182] P. Nava, M. Sierka, R. Ahlrichs, *Phys Chem Chem Phys* **2003**, *5*, 3372-3381.

[183] T. M. Soini, X. F. Ma, O. U. Akturk, S. Suthirakun, A. Genest, N. Rosch, *Surface Science* **2016**, *643*, 156-163.

[184] O. D. Haberlen, S. C. Chung, M. Stener, N. Rosch, *J Chem Phys* **1997**, *106*, 5189-5201.

[185] A. Kohn, F. Weigend, R. Ahlrichs, *Phys Chem Chem Phys* **2001**, *3*, 711-719.

[186] Y. Nanba, T. Ishimoto, M. Koyama, *J Phys Chem C* **2017**, *121*, 27445-27452.

[187] R. Marchal, I. V. Yudanov, A. V. Matveev, N. Rosch, *Chem Phys Lett* **2013**, *578*, 92-96.

[188] F. Weigend, R. Ahlrichs, *Philos T R Soc A* **2010**, *368*, 1245-1263.

[189] J. Kleis, J. Greeley, N. A. Romero, V. A. Morozov, H. Falsig, A. H. Larsen, J. Lu, J. J. Mortensen, M. Dulak, K. S. Thygesen, J. K. Norskov, *Abstr Pap Am Chem S* **2011**, *242*.

[190] T. N. Pingel, M. Jorgensen, A. B. Yankovich, H. Gronbeck, E. Olsson, *Nat Commun* **2018**, *9*.

[191] F. Calle-Vallejo, A. S. Bandarenka, *Chemsuschem* **2018**, *11*, 1824-1828.

[192] M. Jorgensen, H. Gronbeck, *Top Catal* **2019**, *62*, 660-668.

[193] M. Escudero-Escribano, P. Malacrida, M. H. Hansen, U. G. Vej-Hansen, A. Velazquez-Palenzuela, V. Tripkovic, J. Schiotz, J. Rossmeisl, I. E. L. Stephens, I. Chorkendorff, *Science* **2016**, *352*, 73-76.

[194] U. Naher, U. Zimmermann, T. P. Martin, *J Chem Phys* **1993**, *99*, 2256-2260.

References

[195]   A. H. Larsen, J. Kleis, K. S. Thygesen, J. K. Norskov, K. W. Jacobsen, *Physical Review B* **2011**, *84*.

[196]   D. I. Sharapa, D. E. Doronkin, F. Studt, J. D. Grunwaldt, S. Behrens, *Adv Mater* **2019**, *31*, 1807381.

[197]   G. C. Bond, *Chemical Society Reviews* **1991**, *20*, 441-475.

[198]   S. H. Oh, C. C. Eickel, *Journal of Catalysis* **1991**, *128*, 526-536.

[199]   M. Che, C. O. Bennett, *Adv Catal* **1989**, *36*, 55-172.

[200]   A. H. Hakimioun, E. M. Dietze, B. D. Vandegehuchte, D. Curulla-Ferre, L. Joos, P. N. Plessow, F. Studt, *Catalysis Letters* **2021**, 1-5.

[201]   J. Kleis, J. Greeley, N. A. Romero, V. A. Morozov, H. Falsig, A. H. Larsen, J. Lu, J. J. Mortensen, M. Dulak, K. S. Thygesen, J. K. Norskov, K. W. Jacobsen, *Catalysis Letters* **2011**, *141*, 1067-1071.

[202]   J. Wellendorff, K. T. Lundgaard, A. Mogelhoj, V. Petzold, D. D. Landis, J. K. Nørskov, T. Bligaard, K. W. Jacobsen, *Phys. Rev. B* **2012**, *85*, 235149.

[203]   B. V. Reddy, S. N. Khanna, B. I. Dunlap, *Physical Review Letters* **1993**, *70*, 3323-3326.

[204]   V. Kumar, Y. Kawazoe, *Physical Review B* **2002**, *66*, 144413.

[205]   G. A. Somorjai, Y. Li, *Introduction to surface chemistry and catalysis, second edition*, 2nd ed., John Wiley & Sons, Hoboken, N.J., **2010**.

[206]   K. Hayek, R. Kramer, Z. Paal, *Appl Catal a-Gen* **1997**, *162*, 1-15.

[207]   C. T. Campbell, *Nature Chemistry* **2012**, *4*, 597-598.

[208]   Y. Lykhach, S. M. Kozlov, T. Skala, A. Tovt, V. Stetsovych, N. Tsud, F. Dvorak, V. Johanek, A. Neitzel, J. Myslivecek, S. Fabris, V. Matolin, K. M. Neyman, J. Libuda, *Nature Materials* **2016**, *15*, 284.

[209]   M. Comotti, W. C. Li, B. Spliethoff, F. Schuth, *Journal of the American Chemical Society* **2006**, *128*, 917-924.

[210]   M. D. Salazar-Villalpando, B. Reyes, *Int J Hydrogen Energ* **2009**, *34*, 9723-9729.

[211]   J. R. Croy, S. Mostafa, J. Liu, Y. H. Sohn, H. Heinrich, B. Roldan Cuenya, *Catalysis Letters* **2007**, *119*, 209-216.

[212]   M. Cargnello, V. V. T. Doan-Nguyen, T. R. Gordon, R. E. Diaz, E. A. Stach, R. J. Gorte, P. Fornasiero, C. B. Murray, *Science* **2013**, *341*, 771-773.

[213]   S. Kattel, P. Liu, J. G. Chen, *J Am Chem Soc* **2017**, *139*, 9739-9754.

[214]   W. W. Wang, Z. P. Qu, L. X. Song, Q. Fu, *J Energy Chem* **2020**, *40*, 22-30.

[215]   T. Witoon, J. Chalorngtham, P. Dumrongbunditkul, M. Chareonpanich, J. Limtrakul, *Chem Eng J* **2016**, *293*, 327-336.

[216]   T. W. van Deelen, C. H. Mejia, K. P. de Jong, *Nat Catal* **2019**, *2*, 955-970.

[217]   M. Behrens, F. Studt, I. Kasatkin, S. Kühl, M. Hävecker, F. Abild-Pedersen, S. Zander, F. Girgsdies, P. Kurr, B.-L. Kniep, *Science* **2012**, 1219831.

[218]   J. D. Grunwaldt, A. M. Molenbroek, N. Y. Topsoe, H. Topsoe, B. S. Clausen, *Journal of Catalysis* **2000**, *194*, 452-460.

[219]   P. L. Hansen, J. B. Wagner, S. Helveg, J. R. Rostrup-Nielsen, B. S. Clausen, H. Topsoe, *Science* **2002**, *295*, 2053-2055.

[220]   J. B. Wagner, P. L. Hansen, A. M. Molenbroek, H. Topsoe, B. S. Clausen, S. Helveg, *J Phys Chem B* **2003**, *107*, 7753-7758.

[221]   R. N. d'Alnoncourt, X. Xia, J. Strunk, E. Loffler, O. Hinrichsen, M. Muhler, *Phys Chem Chem Phys* **2006**, *8*, 1525-1538.

[222]   S. J. Tauster, S. C. Fung, R. L. Garten, *Journal of the American Chemical Society* **1978**, *100*, 170-175.

[223]   S. J. Tauster, *Accounts Chem Res* **1987**, *20*, 389-394.

[224]   S. Schauermann, N. Nilius, S. Shaikhutdinov, H. J. Freund, *Accounts Chem Res* **2013**, *46*, 1673-1681.

[225]   B. Hammer, J. K. Norskov, *Surface Science* **1995**, *343*, 211-220.

[226]   B. Hammer, J. K. Norskov, *Nature* **1995**, *376*, 238-240.

[227]   B. Hammer, J. K. Norskov, *Advances in Catalysis, Vol 45* **2000**, *45*, 71-129.

[228]   J. Ontaneda, R. A. Bennett, R. Grau-Crespo, *J Phys Chem C* **2015**, *119*, 23436-23444.

[229]   N. D. Nielsen, J. Thrane, A. D. Jensen, J. M. Christensen, *Catalysis Letters* **2020**, *150*, 1427-1433.

[230]   J. K. Norskov, F. Abild-Pedersen, F. Studt, T. Bligaard, *P Natl Acad Sci USA* **2011**, *108*, 937-943.

[231]   A. Morales-Garcia, F. Vines, J. R. B. Gomes, F. Illas, *Wires Comput Mol Sci* **2021**, *11*.

[232]   M. Monai, A. C. Banerjee, *Catalysis Today* **2021**, *382*, 1-2.

[233]   J. K. Nørskov, F. Studt, F. Abild-Pedersen, T. Bligaard, Wiley, Hoboken, New Jersey, **2015**, p. 1 online resource.

[234] L. Li, A. H. Larsen, N. A. Romero, V. A. Morozov, C. Glinsvad, F. Abild-Pedersen, J. Greeley, K. W. Jacobsen, J. K. Norskov, *J Phys Chem Lett* **2012**, *4*, 222-226.

[235] G. Kumar, L. Tibbitts, J. Newell, B. Panthi, A. Mukhopadhyay, R. M. Rioux, C. J. Pursell, M. Janik, B. D. Chandler, *Nature Chemistry* **2018**, *10*, 268-274.

[236] Y. Suchorski, S. M. Kozlov, I. Bespalov, M. Datler, D. Vogel, Z. Budinska, K. M. Neyman, G. Rupprechter, *Nature Materials* **2018**, *17*, 519.

[237] S. M. Kozlov, H. A. Aleksandrov, J. Goniakowski, K. M. Neyman, *J Chem Phys* **2013**, *139*.

[238] S. Polierer, J. Jelic, S. Pitter, F. Studt, *J Phys Chem C* **2019**, *123*, 26904-26911.

[239] P. Ghanekar, J. Kubal, Y. R. Cui, G. Mitchell, W. N. Delgass, F. Ribeiro, J. Greeley, *Top Catal* **2020**, *63*, 673-687.

[240] A. Wander, I. J. Bush, N. M. Harrison, *Physical Review B* **2003**, *68*.

[241] D. R. Alfonso, J. A. Snyder, J. E. Jaffe, A. C. Hess, M. Gutowski, *Physical Review B* **2000**, *62*, 8318-8322.

[242] H. Gronbeck, *J Phys Chem B* **2006**, *110*, 11977-11981.

[243] M. L. Williams, *Occupational and Environmental Medicine* **1996**, *53*, 504-504.

[244] D. Dubbeldam, S. Calero, T. J. H. Vlugt, *Mol Simulat* **2018**, *44*, 653-676.

[245] K. Momma, F. Izumi, *J Appl Crystallogr* **2011**, *44*, 1272-1276.

[246] F. Calle-Vallejo, J. I. Martinez, J. M. Garcia-Lastra, P. Sautet, D. Loffreda, *Angew Chem Int Ed Engl* **2014**, *53*, 8316-8319.

[247] R. Narayanan, M. A. El-Sayed, *Nano Lett* **2004**, *4*, 1343-1348.

[248] R. Narayanan, M. A. El-Sayed, *J Phys Chem B* **2005**, *109*, 12663-12676.

[249] Z. H. Yan, M. G. Taylor, A. Mascareno, G. Mpourmpakis, *Nano Lett* **2018**, *18*, 2696-2704.

[250] M. J. Ndolomingo, N. Bingwa, R. Meijboom, *J Mater Sci* **2020**, *55*, 6195-6241.

[251] P. Sabatier, *Berichte der deutschen chemischen Gesellschaft* **1911**, *44*, 1984-2001.

[252] A. H. Hakimioun, E. M. Dietze, B. D. Vandegehuchte, D. Curulla-Ferre, L. Joos, P. N. Plessow, F. Studt, *Catalysis Letters* **2021**, *151*, 3165-3169.

[253] J. Greeley, M. Mavrikakis, *Nature Materials* **2004**, *3*, 810-815.

[254] D. A. Hansgen, D. G. Vlachos, J. G. G. Chen, *Nature Chemistry* **2010**, *2*, 484-489.

[255] T. Bligaard, J. K. Norskov, S. Dahl, J. Matthiesen, C. H. Christensen, J. Sehested, *Journal of Catalysis* **2004**, *224*, 206-217.

[256] F. Vines, A. Vojvodic, F. Abild-Pedersen, F. Illas, *J Phys Chem C* **2013**, *117*, 4168-4171.

[257] E. M. Fernandez, P. G. Moses, A. Toftelund, H. A. Hansen, J. I. Martinez, F. Abild-Pedersen, J. Kleis, B. Hinnemann, J. Rossmeisl, T. Bligaard, J. K. Norskov, *Angew Chem Int Edit* **2008**, *47*, 4683-4686.

[258] H. J. Monkhorst, J. D. Pack, *Physical Review B* **1976**, *13*, 5188-5192.

[259] P. N. Plessow, *Phys Chem Chem Phys* **2020**, *22*, 12939-12945.

[260] K. Koga, T. Ikeshoji, K. Sugawara, *Physical Review Letters* **2004**, *92*.

[261] J. M. Rahm, P. Erhart, *Nano Lett* **2017**, *17*, 5775-5781.

[262] B. Fleury, R. Cortes-Huerto, O. Tache, F. Testard, N. Menguy, O. Spalla, *Nano Lett* **2015**, *15*, 6088-6094.

[263] H. Li, L. Li, A. Pedersen, Y. Gao, N. Khetrapal, H. Jonsson, X. C. Zeng, *Nano Lett* **2015**, *15*, 682-688.

[264] G. A. Olah, A. Goeppert, G. S. Prakash, *Am. J. Plant Physiol* **2007**, *164*, 525-526.

[265] K. C. Waugh, *Catalysis Today* **1992**, *15*, 51-75.

[266] J. B. Hansen, P. H. Nielsen, *Ertl, G* **2008**, 1856.

[267] M. Behrens, *Recyclable Catalysis* **2015**, *2*.

[268] H. Bahruji, M. Bowker, G. Hutchings, N. Dimitratos, P. Wells, E. Gibson, W. Jones, C. Brookes, D. Morgan, G. Lalev, *Journal of Catalysis* **2016**, *343*, 133-146.

[269] A. Ota, E. L. Kunkes, I. Kasatkin, E. Groppo, D. Ferri, B. Poceiro, R. M. N. Yerga, M. Behrens, *Journal of Catalysis* **2012**, *293*, 27-38.

[270] J. Y. Ye, C. J. Liu, D. H. Mei, Q. F. Ge, *Acs Catalysis* **2013**, *3*, 1296-1306.

[271] M. S. Frei, M. Capdevila-Cortada, R. Garcia-Muelas, C. Mondelli, N. Lopez, J. A. Stewart, D. C. Ferre, J. Perez-Ramirez, *Journal of Catalysis* **2018**, *361*, 313-321.

[272] A. Alvarez, A. Bansode, A. Urakawa, A. V. Bavykina, T. A. Wezendonk, M. Makkee, J. Gascon, F. Kapteijn, *Chem Rev* **2017**, *117*, 9804-9838.

[273] J. Graciani, K. Mudiyanselage, F. Xu, A. E. Baber, J. Evans, S. D. Senanayake, D. J. Stacchiola, P. Liu, J. Hrbek, J. F. Sanz, J. A. Rodriguez, *Science* **2014**, *345*, 546-550.

[274] C. Li, X. Yuan, K. Fujimoto, *Applied Catalysis A: General* **2014**, *469*, 306-311.

[275] F. Arena, G. Mezzatesta, G. Zafarana, G. Trunfio, F. Frusteri, L. Spadaro, *Catalysis Today* **2013**, *210*, 39-46.

[276]   B. Ouyang, W. L. Tan, B. Liu, *Catal Commun* **2017**, *95*, 36-39.
[277]   R. Dalebout, N. L. Visser, C. E. L. Pompe, K. P. de Jong, P. E. de Jongh, *Journal of Catalysis* **2020**, *392*, 150-158.
[278]   R. Beerthuis, J. W. de Rijk, J. M. S. Deeley, G. J. Sunley, K. P. de Jong, P. E. de Jongh, *Journal of Catalysis* **2020**, *388*, 30-37.
[279]   R. Dalebout, L. Barberis, G. Totarella, S. J. Turner, C. La Fontaine, F. M. F. de Groot, X. Carrier, A. M. J. V. Eerden, F. Meirer, P. E. de Jongh, *Acs Catalysis* **2022**, *12*, 6628-6639.
[280]   Y. W. Li, S. H. Chan, Q. Sun, *Nanoscale* **2015**, *7*, 8663-8683.
[281]   S. Kattel, P. J. Ramirez, J. G. Chen, J. A. Rodriguez, P. Liu, *Science* **2017**, *355*, 1296.
[282]   J. Yoshihara, S. C. Parker, A. Schafer, C. T. Campbell, *Catalysis Letters* **1995**, *31*, 313-324.
[283]   T. Fujitani, I. Nakamura, T. Uchijima, J. Nakamura, *Surface Science* **1997**, *383*, 285-298.
[284]   S. A. French, A. A. Sokol, S. T. Bromley, C. R. A. Catlow, S. C. Rogers, F. King, P. Sherwood, *Angew Chem Int Edit* **2001**, *40*, 4437.
[285]   F. Arena, K. Barbera, G. Italiano, G. Bonura, L. Spadaro, F. Frusteri, *Journal of Catalysis* **2007**, *249*, 185-194.
[286]   S. Natesakhawat, J. W. Lekse, J. P. Baltrus, P. R. Ohodnicki, B. H. Howard, X. Y. Deng, C. Matranga, *Acs Catalysis* **2012**, *2*, 1667-1676.
[287]   X. M. Guo, D. S. Mao, G. Z. Lu, S. Wang, G. S. Wu, *Journal of Catalysis* **2010**, *271*, 178-185.
[288]   A. Karelovic, P. Ruiz, *Catal Sci Technol* **2015**, *5*, 869-881.
[289]   Z. M. Hu, R. J. Boyd, *J Chem Phys* **2000**, *112*, 9562-9568.
[290]   F. Studt, M. Behrens, E. L. Kunkes, N. Thomas, S. Zander, A. Tarasov, J. Schumann, E. Frei, J. B. Varley, F. Abild-Pedersen, J. K. Norskov, R. Schlogl, *Chemcatchem* **2015**, *7*, 1105-1111.
[291]   D. Kopac, B. Likozar, M. Hus, *Appl Surf Sci* **2019**, *497*.
[292]   F. Calle-Vallejo, D. Loffreda, M. T. M. Koper, P. Sautet, *Nature Chemistry* **2015**, *7*, 403-410.
[293]   Z. P. Liu, P. Hu, *Journal of the American Chemical Society* **2003**, *125*, 1958-1967.
[294]   J. J. Mortensen, K. Kaasbjerg, S. L. Frederiksen, J. K. Norskov, J. P. Sethna, K. W. Jacobsen, *Physical Review Letters* **2005**, *95*.
[295]   P. A. Taylor, P. B. Rasmussen, C. V. Ovesen, P. Stoltze, I. Chorkendorff, *Surface Science* **1992**, *261*, 191-206.
[296]   D. Guerard, A. Herold, *Carbon* **1975**, *13*, 337-345.
[297]   N. N. Greenwood, A. Earnshaw, *Chemistry of the Elements*, Elsevier, **2012**.
[298]   H. W. Chen, J. M. White, J. G. Ekerdt, *Journal of Catalysis* **1986**, *99*, 293-303.
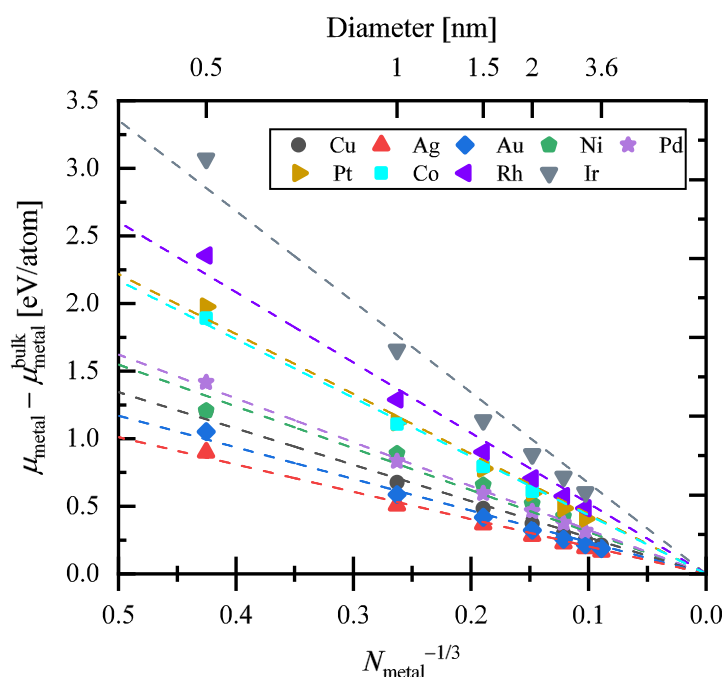
Appendixes

Figure A.1. The calculated chemical potentials of the metals (μ_{Metal}) relative to the chemical potential of the metals bulks (μ_{Metal}^{bulk}) as function of the number of metal atoms in the nanoparticles to the power of -1/3 ($N_{Metal}^{-1/3}$). The copper (Cu), silver (Ag), gold (Au), nickel (Ni), palladium (Pd), platinum (Pt), cobalt (Co), rhodium (Rh) and iridium (Ir) metals are shown in black, red, blue, green, purple, dark yellow, cyan, violet and grey colors shapes. The energies shown are in eV/atom.
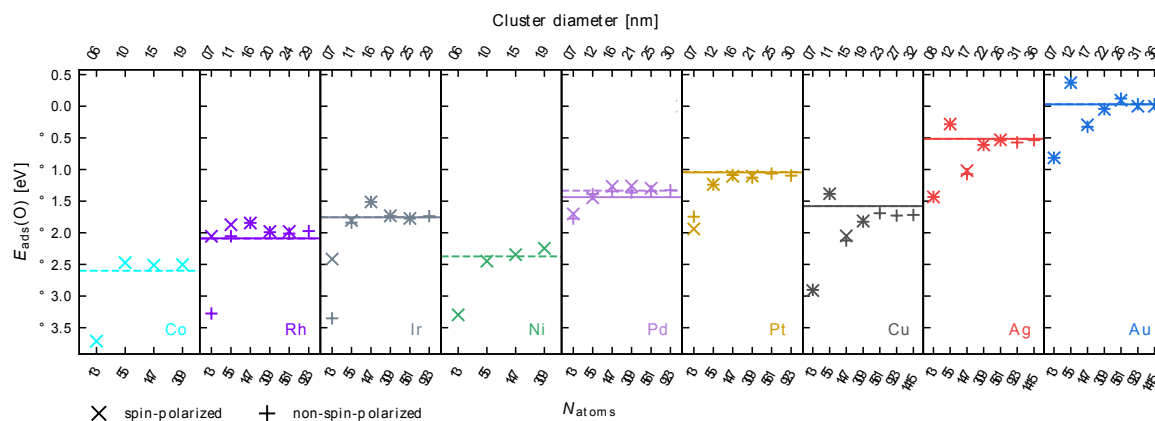
Figure A.2. The calculated oxygen adsorption energy, E_{ads} (O), on the spin-polarized and non-spin-polarized particles against the corresponding number of atoms, N_{atoms} (lower abscissa) and the corresponding size of the particles (upper abscissa). The copper (Cu), silver (Ag), gold (Au), nickel (Ni), palladium (Pd), platinum (Pt), cobalt (Co), rhodium (Rh) and iridium (Ir) metals are shown in black, red, blue, green, purple, dark yellow, cyan, violet and grey colors shapes. The cross and plus shapes represent the calculated oxygen adsorption energies from spin-polarized and non-spin-polarized callculations, respectively. The solid and dashed-lines show the calculated oxygen adsorption energy of the spin-polarized and non-spoin-polarized calculations on the metals surfaces.

Table A.3. Calculated total energies, E_{tot} in eV, of the spin-polarized and non-spin-polarized calculations of different transition metals nanoparticles, magnetic moments (μ_B) (normalized b

y the number of atoms) with and without oxygen adsorbed on the nanoparticles, difference of the total energies ΔE_{tot}, difference of the magnetic moments $\Delta\mu_B$.

System	E_{tot} spin-polarized	E_{tot} non-spin-polarized	Magnetic moment per atom [μ_B]		ΔE_{tot}	$\Delta\mu_B$
			with adsorbate	without adsorbate		
Cu bulk	-14.97	-14.97	0.00	0.00	0.00	0.00
Cu13	7.32	7.33	0.07	0.05	-0.01	0.02
Cu55	1.97	1.97	0.02	0.00	0	0.02
Cu147	-23.10	-23.12	0.00	0.00	0.02	0.00
Cu309	-82.94	-82.94	0.00	0.00	0	0.00
Cu561	-192.84	-192.85	–	0.00	0.01	–
Ag bulk	26.13	26.13	0.00	0.00	0.00	0.00
Ag13	18.85	18.84	0.03	0.00	0.01	0.03
Ag55	58.15	58.14	0.00	0.00	0.01	0.00
Ag147	135.01	134.98	0.00	0.00	0.03	0.00
Ag309	257.52	257.39	0.00	0.00	0.13	0.00
Ag561	436.16	436.05	0.00	0.00	0.11	0.00
Au bulk	-2.51	-2.51	0.00	0.00	0.00	0.00
Au13	10.28	10.28	0.00	0.00	0	0.00
Au55	17.91	17.90	0.00	0.00	0.01	0.00
Au147	23.28	23.25	0.00	0.00	0.03	0.00
Au309	19.44	19.36	0.00	0.00	0.08	0.00
Au561	-1.88	-2.07	0.00	0.00	0.19	0.00
Ni bulk	-10.87	–	0.66	0.66	–	0.00
Ni13	-84.73	–	0.77	0.61	–	0.16
Ni55	-269.88	–	0.76	0.73	–	0.03
Ni147	-616.46	–	0.7	0.69	–	0.01
Ni309	-1175.93	–	0.68	0.68	–	0.00
Ni561	-10.87	–	0.66	0.66	–	0.00
Pd bulk	-60.02	-59.75	0.33	0.42	-0.27	-0.09
Pd13	-7.06	-6.96	0.15	0.43	-0.1	-0.28
Pd55	-61.76	-61.60	0.27	0.26	-0.16	0.01
Pd147	-200.304	-199.48	0.3	0.31	-0.824	-0.01
Pd309	-462.37	-460.44	0.33	0.34	-1.93	-0.01
Pd561	-887.06	-883.99	0.35	0.36	-3.07	-0.01
Pt bulk	-100.59	-100.59	0.00	0.00	0	0.00
Pt13	-15.41	-14.96	0.16	0.46	-0.45	-0.30
Pt55	-110.65	-110.35	0.4	0.40	-0.3	0.00
Pt147	-345.48	-345.31	0.27	0.28	-0.17	-0.01

Pt$_{309}$	-781.71	-781.21	0.25	0.26	-0.5	-0.01
Pt$_{561}$	-1482.61	-1482.60	–	0.03	-0.01	–
Co bulk	-30.98	–	1.72	1.69	–	0.03
Co$_{13}$	-174.22	–	2.07	2.08	–	-0.01
Co$_{55}$	-511.81	–	1.853	1.89	–	-0.04
Co$_{147}$	-1132.509	–	1.81	1.82	–	-0.01
Co$_{309}$	-30.98	–	1.78	1.79	–	-0.01
Rh bulk	-137.59	-137.59	0.00	0.00	0	0.00
Rh$_{13}$	-28.74	-24.62	1.15	1.46	-4.12	-0.31
Rh$_{55}$	-164.74	-162.72	0.94	1.03	-2.02	-0.09
Rh$_{147}$	-492.19	-492.09	0.16	0.16	-0.1	0.00
Rh$_{309}$	-1095.75	-1095.36	0.24	0.25	-0.39	-0.01
Rh$_{561}$	-2062.36	-2061.13	0.14	0.14	-1.23	0.00
Ir bulk	-192.17	-192.16	0.00	0.00	-0.01	0.00
Ir$_{13}$	-39.26	-35.77	1.83	1.90	-3.49	-0.07
Ir$_{55}$	-229.56	-229.11	0.4	0.45	-0.45	-0.05
Ir$_{147}$	-689.06	-689.06	0.00	0.00	0	0.00
Ir$_{309}$	-1525.71	-1525.71	0.00	0.00	0	0.00
Ir$_{561}$	-2863.31	-2863.29	0.03	0.03	-0.02	0.00

Table A.4. Unit cell sizes, coverages of different adsorbates on slabs and k-point grids of each calculated systems are depicted.

Surfaces	HCOO			cis-COOH			CO		
	Unit cell	Coverage (ML)	k-point sampling	Unit cell	Coverage (ML)	k-point sampling	Unit cell	Coverage (ML)	k-point sampling
Cu(100)	(4×4)	0.12	3×3×1	(4×4) (3×3)	0.12 0.22	3×3×1 4×4×1	(3×3)	0.11	4×4×1
	(3×3)	0.22	4×4×1	(2×2)	0.5	6×6×1	(2×2)	0.25	6×6×1
	(2×2)	0.5	6×6×1	(3×3) 3×COOH	0.66	4×4×1	(2×2) 2×CO	0.5	6×6×1
	(2×3)	0.66	4×6×1	(2×3) 2×COOH	0.66	4×6×1	-	-	-
	(2×2) 2×HCOO	1	6×6×1	(2×2) 2×COOH	1	6×6×1	(1×1)	1	12×12×1
Cu(110)	(4×4)	0.12	3×3×1	(4×4)	0.12	3×3×1	(3×3)	0.11	4×4×1
	(3×3)	0.22	4×4×1	(3×3)	0.22	4×4×1	(2×2)	0.25	6×6×1
	(2×4) 2×HCOO	0.5	6×3×1	(2×4) 2×COOH	0.5	6×3×1	(2×2) 2×CO	0.5	6×6×1
	(2×2) 2×HCOO	1	6×6×1	(2×2) 2×COOH	1	6×6×1	(1×1)	1	12×12×1
Cu(111)	(4×4)	0.12	3×3×1	(4×4)	0.12	3×3×1	(3×3)	0.11	4×4×1
	(3×3)	0.22	4×4×1	(3×3)	0.22	4×4×1			
	(2×2)	0.5	6×6×1	(2×2)	0.5	6×6×1	(3×3) 2×CO	0.22	4×4×1
	(3×2) 2×HCOO	0.66	4×6×1	(3×2) 2×COOH	0.66	4×6×1	(2×2)	0.25	6×6×1
	(3×3) 3×HCOO	0.66	4×4×1	(3×3) 3×COOH	0.66	4×4×1	(2×2) 2×CO	0.5	6×6×1
	(1×2)	1	12×6×1	(1×2)	1	12×6×1	(1×1)	1	12×12×1
Cu(211)	(3×6)	0.33	4×2×1	(3×6)	0.33	4×2×1	(3×3)	0.33	4×4×1
	(3×4)	0.5	4×3×1	(3×4)	0.5	4×3×1	(3×2)	0.5	4×5×1
	(3×3)	0.66	4×4×1	(3×3)	0.66	4×4×1	(3×3) 2×CO	0.66	4×4×1
	(3×2)	1	4×5×1	(3×2)	1	4×5×1	(3×2) 2×CO	1	4×5×1

Table A.5. Total energies of each of the calculated systems. All energies in eV. (a) in x and y direction.

| | | | Adsorbate | | | | | |
| | | | Formate | | cis-COOH | | CO | |
Surfaces	Size[a]	*E*	Size	*E*	Size	*E*	Size	*E*
Cu(100)	4×4	-22.1111	4×4	-44.7658	4×4	-43.8454	3×3	-25.1395
	3×3	-18.003	3×3	-35.09306	3×3	-34.1766	2×2	-18.2001
					2×2	-27.2331		
	2×3	-12.4363	2×3	-53.37807	3×3 (3×COOH)	-77.6105	2×2 (2×CO)	-30.9429
	2×2	-5.5257	2×2	-28.10359	2×3 (2×COOH)	-51.5739		
	1×1	-1.3813	2×2 (2×HCOO)	-49.3798	2×2 (2×COOH)	-48.3009	1×1	-13.4862
Cu(110)	4×4	-12.2079	4×4	-35.1978	4×4	-34.1882	3×3	-19.6398
	3×3	-6.8656	3×3	-29.8633	3×3	-28.8539	2×2	-15.8243
	2×4	-6.1029	2×4 (2×HCOO)	-52.12319	2×4 (2×COOH)	-50.14508	2×2 (2×CO)	-28.7625
	2×2	-3.0506	2×2 (2×HCOO)	-49.0243	2×2 (2×COOH)	-47.0684	1×1	-13.3442
	1×1	-0.7625						
Cu(111)	4×4	-26.2532	4×4	-48.6733	4×4	-47.6981	3×3	-27.3015
	3×3	-14.7605	3×3	-37.1371	3×3	-36.1292	3×3 (2×CO)	-39.8089
	3×2	-9.8388	2×2	-28.9057	2×2	-28.0289	2×2	-19.1069
	2×2	-6.5573	3×2 (2×HCOO)	-54.34907	3×2 (2×COOH)	-52.7968	2×2 (2×CO)	-31.5247
	1×2	-3.2789	3×3 (3×HCOO)	-81.5849	3×3 (3×COOH)	-79.2094	1×1	-13.1757
	1×1	-1.6392	1×2	-49.5454	1×2	-24.0853		
Cu(211)	3×6	-28.1207	3×6	-51.0394	3×6	-50.0979	3×3	-26.8508
	3×4	-18.7475	3×4	-41.6697	3×4	-40.7196	3×2	-22.1513

3×3	-14.0618	3×3	-36.98902	3×3	-36.0104	3×3 (2×CO)	-39.6126
3×2	-9.3660	3×2	-32.2313	3×2	-31.2294	3×2 (2×CO)	-34.3138

Table A.6. Zero-point energy corrections (ZPE), entropy contributions and total energies of gas-phase species and intermediates. (a) All values in eV. (b) $H_2(g)$ and $CO_2(g)$ are corrected by +0.09 eV and +0.41 eV, respectively, as described in reference[290]. (c) All values from reference[290], that is data based on Cu(211) and the BEEF-vdW functional.

Intermediates	E	ZPE[c]	S[c]	$C_p dT$[c]
HCOO*	see Table A.5	0.624	0.000751	0.105
CO*	see Table A.5	0.192	0.000452	0.085
Gas-phase species				
$H_{2(g)}$[b]	-7.072	0.270	0.001380	0.091
$CO_{2(g)}$[b]	-18.003	0.320	0.002263	0.098
$CO_{(g)}$	-12.074	0.130	0.02092	0.091

Acronyms

ASE	Atomic Simulation Environment
B3LYP	Becke, 3-parameter, Lee-Yang-Parr hybrid functional
BEEF-vdW	Bayesian Error Estimation Functional with van der Waals
BEP	Bronsted-Evans-Polanyi
BLYP	Becke, Lee-Yang-Parr hybrid functional
CMS	Computational Materials Science
D1,D2,D3	Grimme's dispersion corrections models
DFT	Density Functional Theory
DOF	Degree of Freedom
GCN	Generalized Coordination Number
GGA	Generalized Gradient Approximation
GHG	Greenhouse Gas
HF	Hartree-Fock
HK	Hohenberg-Kohn
HOMO	Highest Occupied Molecular Orbital
IKFT	Institute of Catalysis Research and Technology
KIT	Karlsruhe Institute of Technology
KS	Kohn Sham
LCAO	Local-Combination-of-Atomic-Orbitals
LDA	Local Density Approximation
MAE	Mean Absolute Error
MOF	Metal Organic Framework
MTBE	Metyl-tert-butylether

NPs	Nanoparticles
PAW	Projected Augmented Wave
PBE	Perdew-Bruke-Enzerhof functional
ppm	Part per Million
PW91	Perdew and Wang functional
QMC	Quantum Monte-Carlo
QSE	Quantum Size Effect
RWGS	Reverse Water Gas Shift reaction
SAPT	Symmetry-Adapted Perturbation Theory
SMSI	Strong Metal-Support Interactions
TOF	Turnover Frequency
TPSS	Tao, Perdew, Staroverov, and Scuseria functional
VASP	Vienna Ab initio Simulation Package
vdW	van-der-Waals
WGS	Water Gas Shift reaction
XC	Exchange-Correlation
ZPE	Zero Point Energy

Acknowledgements

List of Publications

1. **Hakimioun, A.H.**, Dietze, E.M., Vandegehuchte, B., Curulla-Ferré, D., Joos, L., Plessow, P. N., Studt, F. Theoretical Investigation of the Size Effect on the Oxygen Adsorption Energy of Coinage Metal Nanoparticles. *Catalysis Letters* 151, 3165–3169 (**2021**).

2. Barberis, L., **Hakimioun, A.H.**, Plessow, P.N., Visser, N.L., Stewart, J.A., Vandegehuchte, B., Studt, F., de Jongh, P. Competition between reverse water gas shift reaction and methanol synthesis from CO_2: influence of copper particle size. *Nanoscale* 14, 37 (**2022**): 13551-13560.

3. **Hakimioun, A.H.**, Kaźmierczak, K., Vandegehuchte, B., Curulla-Ferré, D., Plessow, P. N., Studt, F. Particle Size effect in Transition Metals Nanoparticles. *in preparation*.

4. **Hakimioun, A.H.**, Kaźmierczak, K., Vandegehuchte, B., Curulla-Ferré, D., Plessow, P. N., Studt, F. Metal-Support Interactions in Heterogeneous Catalysis. *ACS omega* 8, 11 (**2023**): 10591-10599.

5. **Hakimioun, A.H.**, Kaźmierczak, K., Vandegehuchte, B., Curulla-Ferré, D., Plessow, P. N., Studt, F. Scaling relations in Adsorption Energies. *in preparation*.

6. Daum, S., Toms, J., Reshetnikov, V., Özkan, H.G., Hampel, F., Maschauer, S., **Hakimioun, A.**, Beierlein, F., Sellner, L., Schmitt, M. and Prante, O. Identification of boronic acid derivatives as an active form of N-alkylaminoferrocene-based anticancer prodrugs and their radiolabeling with [18]F. *Bioconjugate Chemistry* 30(4), pp.1077-1086 (**2019**).

7. Ghiasi, R., **Hakimioun, A. H.** Theoretical insights of magnetizability and solvent effect on the electronic properties of CoB_8-molecule. *Quarterly Journal of Iranian Chemical Communication 5*, no. 1, pp. 1-120, Serial No. 14 (**2017**): 67-78.

8. Auras, F., Ascherl, L., **Hakimioun, A.H.**, Margraf, J.T., Hanusch, F.C., Reuter, S., Bessinger, D., Döblinger, M., Hettstedt, C., Karaghiosoff, K. and Herbert, S. Synchronized offset stacking: a concept for growing large-domain and highly crystalline 2D covalent organic frameworks. *Journal of the American Chemical Society* 138(51), pp.16703-16710 (**2016**).

9. Ghiasi, R., Nemati, M., **Hakimioun, A.H.** Solvent effect on the structural, electronic, spectra properties and first hyperpolarizability of W $(CO)_5$L, L=(4-pyridylmethylene) malononitrile. *Journal of the Chilean Chemical Society* 61(2), pp.2921-2928 (**2016**).

10. **Hakimioun, A.H.**, Makkipour, P., Ghiasi, H., Pasdar, H. Computational study of gas-phase molecular structure and substitution effects in para-substituted nickelabenzenes (p-XC_5H_4) Ni $(CO)_2F$. *Russian Journal of Physical Chemistry A* 89(9), pp.1614-1618 (**2015**).

11. Ghiasi, R., Fashami, M.Z., **Hakimioun, A.H.** A density functional approach toward structural features and properties of C 20… N 2 X 2 (X= H, F, Cl, Br, Me) molecules. *Journal of Theoretical and Computational Chemistry*, 13(04), p.1450023 (**2014**).

12. Ghiasi, R., Ara, T.J., **Hakimyoun, A.H.** Spectroscopic studies and molecular orbital analysis on platinanaphthalenes and ring-fused BN platinanaphthalenes. *Russian Journal of Physical Chemistry A*, 88(4), pp.616-624 (**2014**).

13. Ghiasi, R., **Hakimyoon, A.H.** Density Functional Theory Analysis of Borazyne Complexes of Ni $(B_3N_3H_nF_{2-n})(CO)_2$ (n= 0-2). *Journal of the Mexican Chemical Society* 56(2), pp.100-104 (**2012**).

Curriculum Vitae

Personal Information

Name: Amir Hossein Hakimioun

Birth date: 31.07.1990

Birth place: Tehran, Iran

Education

10.2018 - present	**Ph.D. in Chemistry** Institute of Catalysis Research and Technology (IKFT). Karlsruhe Institute of Technology (KIT), Germany. Supervisor: Prof. Dr. Felix Studt *Theoretical studies on the influence of size and support interactions of copper catalysts for CO_2 hydrogenation to methanol*
04.2015 - 09.2018	**M.Sc. in Chemistry** Friedrich-Alexander Universität Erlangen-Nürnberg Supervisor: Prof. Dr. Timothy Clark *Enzyme-Independent Chemical Reactions for Chemistry in Living Cells*
10.2008 - 02.2013	**B.Sc. in Applied Chemistry** Tehran Branch of Azad University of Iran Supervisor: Prof. Dr. Reza Ghiasi

Professional Experience

10.2018 - present	**Ph.D. Candidate** Institute of Catalysis Research and Technology (IKFT). Karlsruhe Institute of Technology (KIT), Germany.
10.2015 - 10.2018	**Research Assistance** Computer-Chemistry-Center (CCC) Friedrich-Alexander Universität Erlangen-Nürnberg
01.2010 - 0.1.2013	**Research Assistance** Tehran Branch of Azad University of Iran

Eidesstattliche Erklärung

Hiermit versichere ich eidesstattlich, dass ich die hier vorgelegte Dissertation selbstständig angefertigt habe und keine anderen Quellen und Hilfsmittel genutzt habe als die hier angegebenen. Die wörtlich und inhaltlich übernommenen Stellen wurden als solche kenntlich gemacht. Die Regeln zur Sicherung guter wissenschaftlicher Praxis des Karlsruher Instituts für Technologie (KIT) in der gültigen Fassung wurden beachtet und Primärdaten gemäß Abs. A(6) gesichert. Die elektronische Version der Arbeit stimmt mit der schriftlichen überein. Die Arbeit wurde in gleicher oder ähnlicher Form noch keiner anderen Prüfungsbehörde zur Erlangung eines akademischen Grades vorgelegt.

Karlsruhe, den 13.09.2022